TECHNISCHE UNIVERSITÄT MÜNCHEN

Professur für Leitungsgebundene Übertragungstechnik

Digital Pre-Compensation of Optical Transmitters

Ginni Khanna

Vollständiger Abdruck der von der Fakultät für Elektrotechnik und Informationstechnik der Technischen Universität München zur Erlangung des akademischen Grades eines

Doktor–Ingenieurs

genehmigten Dissertation.

Vorsitzender: Prof. Dr.-Ing. Christian Jirauschek

Prüfer der Dissertation:
1. Prof. Dr.-Ing. Norbert Hanik
2. Prof. Dr.-Ing. Bernhard Schmauß

If you can dream it, you can do it !
- Walt Disney

Acknowledgement

I didn't know it was Walt Disney who said that, for me it was always my grandparents and parents. There was never a question on whether something could be achieved. It was always about your will. So, naturally when I asked my parents that I would like to go outside of India and live my life they always supported me and here I am finishing the thesis I have been working on quite some time now.

In retrospective, it almost feels like a plan which unfolded itself. Going to Prof. Norbert Hanik's lecture, joining the Optical Communication Systems course, completing the corresponding lab, followed by the Master Thesis under his supervision and finally wrapping up PhD work under him. He has been nothing less than a blessing for me in the past 8 years of my life in Munich and I guess this acknowledgement or a simple thank you does not even come close to convey how grateful I am for everything he has done. He is an exceptional human being and a very caring supervisor. Besides the educational aspects, over the years I have managed to learn quite a bit from him, especially how to remain calm, like always calm :) and keep on working on the next thing. I guess I couldn't have asked for a better supervisor. Thank you for everything Prof. Hanik!

With this I would also like to extend my gratitude to Prof. Bernhard Schmauß for being part of the defence committee. Thank you for taking out the time.

Even though I was employed by TU Munich and had a dedicated office there, I spent like 80% of my time in the lab in Coriant R&D GmbH which used to become my second home during deadlines. My relationship with Coriant goes back to Summer 2013, when I joined as a Master Thesis student and just stayed there for the next 5 years. This work would be definitely impossible without the continuous support of Bernhard Spinnler, Stefano Calabro and Erik De Man. There people are like walking encyclopedias for wireless and optical communications. Bernhard has been an exceptional mentor. I clearly remember the day when he gave me the new DACs and ADCs and said *"make them run now, they are yours"*. For him, there was never settling for just *"good"* and that definitely drove me crazy sometimes. If it can be done better, it has to be. I guess more than half of results achieved during the thesis is because he was not settling for anything less than the best :) Thanks

Bernhard for teaching me to not settle down and keep on looking for better solutions.

For any mathematical doubt, Stefano was the person to run to. I was always in awe when he started to teach or explain anything. It didn't matter what it was, he just knew the answers and never ever got tired of answering them. Through him, I understood maths is nothing but a language to translate the physical effects to something humans can understand. Thank you Stefano for all your wonderful explanations and the precious time I used to rob you off.

If there is one name Erik definitely deserves, it is the "One Man Army". He is the soul of the lab. Nothing can move without him or more appropriately, no one will know how it moves if he isn't there. All the setups built in the lab during this thesis were only possible because he was there. I remember how all of us were trying to plan experiments around his vacations, so we do not miss him when we needed him. Erik, you are exceptional person with an ability to always be there and give. Thank you for all the support throughout and for the endless times I have asked you to help me fix anything in the lab !

Thank you to all the colleagues at Coriant for their fruitful discussions and feedback on my work and presentations during my thesis.

Thanks to all the great colleagues at LNT, LÜT and COD. I barely spent time here but in the last couple of months while writing, I have truly enjoyed my time here and made some great friends too. I guess I will be the only one for a long time to give the *Einstandfeier* in the last year of the PhD. Some colleagues have graduated but I can never forget their help and support. Thanks Adriana, Yingkan, Beril, Talha and Carlos for the great time at the conferences and Coriant! You made the whole deal great fun.

Vielen Dank an meine Lieblingstante, Heike Vorpahl. Danke, dass du immer für mich da warst und mir geholfen hast hier im Deutschland auf meinen eigenen Beinen zu stehen.

Ma, Papa, Nabh, Neelakshi and LG. It is because of you I am where I am right now. I know we don't do thank-you's in the family, I am blessed to have you as a family :)

Andrei, my husband whom I have had the privilege to get married to during my thesis. Thanks a lot for this great time and being consistently there and picking me up whenever I was down. You have been a pillar throughout this time and I am grateful to have you as my partner.

München, July 2019   Ginni Khanna

Contents

Zusammenfassung

Um etwas zu verbessern, müssen wir es erst verstehen. Mathematische Modelle werden oft verwendet, um die physikalische Welt zu erfassen und helfen die Auswirkungen besser zu verstehen. Diese Dissertation ist ein Beispiel, wie man mathematische Modelle einsetzen kann, um ein Problem im Bereich der Optischen Übertragungstechnik zu lösen, nämlich : Beseitigung linearer und nicht-linearer Verzerrungen in den Komponenten des Senders.

Die Disseration beginnt mit der Einführung der Einschränkung von den Komponenten und untersucht dann eine berühmte Methode der digitalen Vorkompensastion. Ein mathematisch speicherpolynomisches Modell wird verwendet um die Komponenten zu modelliern. Danach wird die Inverse Funktion des Systems erzeugt durch eine bekannte Methode, der indirekten Lernarchitektur. Mit den Gründlagen von mathematischen Modellen, der indirekten Lernarchitektur und der Digitalsignalverarbeitung, wird eine Digitalvorvezerrungsprozess erstellt, der in der heutigen und nächsten Generation des optischen Transponders ohne Probleme integrieren werden kann.

Ein wesentlicher Beitrag der Dissertation ist der Entwicklung des Digitalvorvezerrungsblocks, der letzendlich Geld und Zeit spart, beim Automatisieren der Charakterizierung der Komponenten und deren Entzerrung.

Abstract

To make something better, we often need to first understand it. Mathematical models capture the essence of the physical world and help us to better comprehend the effects. This thesis is one such example of using mathematical models to understand and solve one such problem faced in the optical transmitter of high data rate optical systems, specifically the

linear and non-linear effects in the transmitter components.

This thesis starts with first laying down the several limitations of these components and then reviewing a very famous technique of digital pre-compensation. A mathematical memory polynomial model is utilized to capture the working of the transmitter components and then approach the problem of producing the inverse of the transmitter components with a known scheme called the indirect learning architecture. Together with the principles of mathematical modeling, indirect learning architecture and clever digital signal processing (DSP) techniques, a robust DPC architecture is established which can be conveniently assimilated in the present and next-generation optical transponder design.

A substantial contribution of the thesis is in the development of a DPC block which can ultimately save time and money by automating the characterization and mitigation of the transmitter effects.

1

Introduction

Background

Optical communications form the backbone of the present day communication network. Invisible to the eye, buried deep in the ground and under the sea, optical fibers are carrying terabits of data every moment of the day. Whether it is a phone call, a high-definition movie, a banking transaction, the next flight ticket that needs to be booked, each and every bit of information is supported by millions of fibers laid around the planet.

It was in the 1970s when optical fibers started to make their way into the telecommunications industry. In 1977, General Electronics and Telephone successfully transmitted 6 Mbit/s over a field deployed fiber in Long Beach, California [1]. Fast forward to year 2018, at the time of writing this thesis, researchers have demonstrated a transmission experiment with a data rate of 159 Tb/s over 1045 km [2], leading to a record bit-rate distance product of 166 Pb.km/s. To put things into perspective, 6 Mbit/s is the data rate received by a wireless mobile phone now.

The evolution of optical communications in the last 50 years has seen commercial systems based on intensity modulation direct-detection (IM-DD), delivering bit rates of 10 Gb/s to coherent systems capable of transmitting bit rates up to 600 Gbit/s on a single wavelength.

The arrival of the Internet in the 1990s and the subsequent bloom in the plethora of internet services such as file sharing, movie streaming, gaming, social networking, cloud computing etc., led to a huge demand and need for higher bandwidth and data rate com-

munication systems. For optical communications, it meant to re-visit an old scheme of coherent systems, which, in contrast to the legacy IM-DD system, has the potential to support higher data rates and deliver better performance. Combined with DSP, coherent systems provided a better alternative to the legacy system. It was then, in early 2000s, that research was rekindled in coherent systems and by the end of 2010, commercial coherent systems supporting bit rates of up to 100 Gbit/s were already being deployed.

As the data rates evolved from 10 Gb/s to 600 Gbit/s on a single wavelength, the optical transponder saw significant upgrades in its hardware components. The legacy systems, based on IM-DD were made up of a light amplification by stimulated emission of radiation (LASER) module and an external modulator at the transmitter. At the receiver side, there was a simple photodiode capable of converting incoming optical field to an electrical current.

Coherent systems, on the other hand, exploit the amplitude and phase information of the optical field. Another dimension of the optical field which can be used to transmit information is the polarization [1,3]. Two states of polarization, which are the X and Y are utilized in coherent systems to transport information. With the combination of the two polarizations, amplitude and phase of the optical field, DP-mQAM (m is the modulation order of QAM) signals can be constructed. For transmission of such signals, transmitter systems are made up of additional hardware components comprising of the digital to analog converter (DAC), driver amplifier (DA), and dual-polarization Mach-Zehnder Modulator (DP-MZM). The receiver, combined with suitable DSP becomes significantly more complicated than the IM-DD receiver, capable of harvesting even the phase information of the optical signal.

Ever since, extensive research and development is being directed towards making the performance of coherent systems even better, to be able to transmit even higher data rates, over even longer distances.

Motivation

In order to meet the ever-growing demands for higher data traffic [4], the optical community has come up with several solutions. Some of the solutions to enable high data rates using standard single mode fiber (SSMF) are :

- Transmit higher number of wavelengths

- Transmit higher baud rates (> 32 GBaud)

- Transmit higher modulation formats (> 4QAM)

Using more wavelengths means utilization of a higher number of components at the transmitter. This adds to additional costs for the overall transponder, and ultimately the cost per transmitted bit increases. The design goal of the system is, to achieve the highest data rate possible with the lowest possible number of wavelengths, for the available electro-optics and CMOS technologies [5]. This means increasing the baud rate and modulation order of each carrier (wavelength). However, increasing the baud rate or the modulation order of the system is not as straightforward.

The DAC, driver amplifier and DP-MZM are indispensable components and lie at the heart of a high data rate optical communication system. All these components are not ideal and exhibit various linear and non-linear effects which hamper the quality of the transmit signal even before the signal makes its way into the optical fiber. The linear effects, such as bandwidth limitation and I/Q skew become even more significant as the baud rate of the transmit signal increases. Non-linear effects from the DA and DP-MZM start to manifest when higher modulation formats are transmitted.

Not accounting for these effects and failure to compensate for them can lead to degradation of bit error rate (BER) and the system's overall bit-rate distance product. Additionally, not compensating for the linear and non-linear effects leads to an inefficient utilization of the transmitter components.

DPC consisting of digital pre-emphasis (DPE) and digital pre-distortion (DPD) is a very well known technique to mitigate various linear and non-linear effects at the transmitter. The principle behind the scheme is pretty simple. The DPC block is an additional filter at the transmitter which manipulates the incoming signal with the inverse of the overall channel response at the transmitter.

With the advent of coherent systems, intensive research has been conducted in certain linearization techniques to mitigate the effects of non-ideal components. Many of the proposed techniques are quite static and don't take into consideration the temporal effects of degradation of the components. Other techniques are measurement based and require an accurate characterization and measurement of the individual components which is a time consuming process. Moreover, the proposed techniques can only mitigate the effects of the DAC, DA and DP-MZM individually.

This dissertation is an attempt to understand the various linear and non-linear effects of the non-ideal components of an optical transmitter. After an analysis of such effects, a robust method is introduced which avoids the need for factory characterization of the

transmitter components, and also delivers a substantial performance improvement by tackling all transmitter impairments at once.

1.1 Outline

Following the introduction chapter, the thesis starts with **Chapter 2** where the **Principles of Digital Pre-Compensation** are presented to the reader. The reader is provided with a brief introduction to the problem statement. Following this, the working principle of the digital pre-compensation DPC block in modern-day optical transponders is discussed. This chapter also updates the reader with various solutions available in literature and practice to implement DPC. After discussing the previous works, the chapter draws comparisons of the DPC block developed in this thesis with the previous works and concludes by summarizing the major contributions of this work.

Next follows **Chapter 3** which gives an introduction to the coherent transponder's components. It starts with the basic overview of the LASER, the digital to analog converter DAC, the electrical driver amplifier DA and the dual-polarization Mach-Zehnder Modulator. Next a detailed discussion of the various linear and non-linear effects of the transmitter components is given. The effect of the limitations is evaluated with the support of various measurements. The receiver components are then briefly covered and the chapter concludes with a short description on the components of the DSP blocks which enable the transmission and reception of signals in transponders.

Chapter 4 forms the backbone of this thesis and is the most significant part which describes the theory essential for designing the DPC blocks. It lays down the foundations of the building principles of the memory polynomial model, the indirect learning architecture. This is the essential chapter on the *how-to* of the DPC. It gives a detailed derivation of the estimation of the DPC coefficients. The two modes of the DPC block namely training and working are also undertaken here. The distinct system models are illustrated in this chapter and are clarified with supplementary block diagrams and the required DSP blocks. To encapsulate, this chapter is the go-to recipe for implementing DPC in practice.

Once the theory is established in chapter 4, we make our way to **Chapter 5** where the experimental results of DPC are extensively discussed in diverse setups and system scenarios. We evaluate the performance of the algorithm to compensate the linear effects and then test the feasibility of it in a non-linear transmitter environment. This chapter also examines the accuracy of the DPC algorithm by assessing the estimated transmitter

I/Q skew values over several runs of the algorithm.

Chapter 6 documents the results of two field trials which were conducted during the course of the thesis. It further elaborates on the dynamic use of the algorithm to characterize the transmitter components in an on-field environment. The chapter showcases field trial transmission of single carrier 200 Gbit/s and 400 Gbit/s signals with state-of-the-art transmitter components.

Towards the end, **Chapter 7** which is the conclusion offers the user a concise description of the thesis at one place and captures the essential contributions of this thesis.

2

Principles of Digital Pre-Compensation

2.1 Coherent Transmitter Overview

An overview of the various components of a dual polarization coherent optical transmitter is shown in Fig. 2.1. The coherent transmitter consists of a high sampling rate 4-channel DAC, a high gain 4-channel electrical DA required for linearly amplifying the low output signal from the DAC, a DP-MZM which modulates the analog signal and a LASER source.

In addition to the hardware components, the transmitter comprises of transmitter DSP. The transmitter DSP is a crucial part of the coherent transponder. In the past 5-8 years, the DAC has become one of the cardinal components of the transponder. Combined with the DSP techniques, which include forward error correction (FEC), root raised cosine (RRC) filtering, pre-compensation [6, 7], various complex analog waveforms can be generated. Jointly with the electro-optic components, DP-mQAM (m is the modulation order $\in$ {4, 8, 16, 32, 64, 128, 256}) signals can then be constructed at the transmitter [5, 8].

The electronic and electro-optic transmitter components, which include the DAC, DA and DP-MZM have specific operating conditions, under which their performance is ideal. However, when made to run at their technology limits, the components exhibit various limiting effects such as 3-dB bandwidth limitation [7, 9–14] and transmitter I/Q skew [15–17]. The transmitter I/Q skew is a critical impairment for high-baud rate and high modulation format systems and arises due to the the uneven length of electrical connections at the
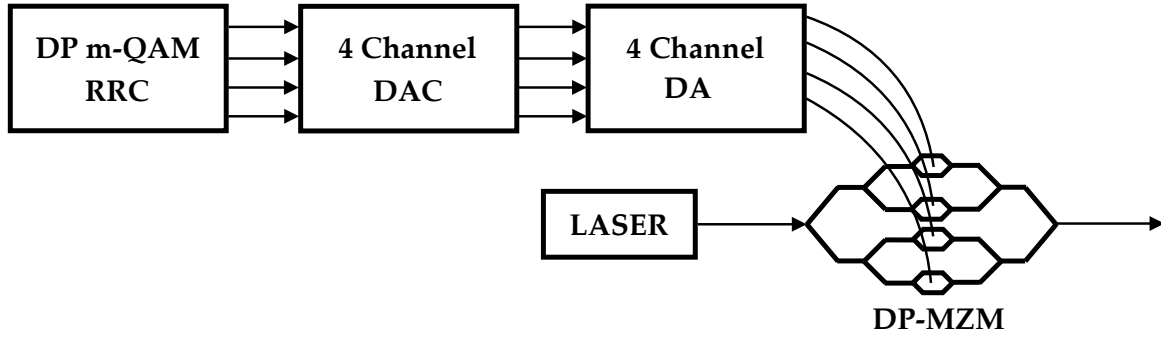
Figure 2.1: Dual polarization coherent optical transmitter

transmitter circuits. The generation of multi-level signals for higher order QAM requires the driving of the electrical DA and DP-MZM with higher input voltage signals. Moreover, it is highly desirable in design of some systems to achieve as high a transmit power as possible in order to boost the transmit optical signal to noise ratio (OSNR) and preserve the quality of the transmit signal. This is only achieved by increasing the gain of the driver amplifier, which ultimately leads to manifestation of various non-linearites and distortions in the transmit signal [18–23].

A suitable method is then needed to measure and mitigate the above mentioned limitations of the DAC, DA and DP-MZM.

2.2 Digital Pre-Compensation

Digital pre-compensation is a well-known DSP method borrowed from the wireless community [18, 18–20, 23]. In such a scheme, a digital algorithm, hereby termed DPC is implemented at the transmitter DSP, as shown in Fig. 2.2. Ideally, the DPC block implements the inverse transfer function of the transmitter components on the input signal. When the distorted input signal passes through the transmitter block, the combination of the pre-distorted input signal and the characteristics of the transmitter components becomes unity. Thus, the output signal becomes equal to the input signal.

The DPC block consists of a set of algorithms to mitigate the 3-dB bandwidth limitation, transmitter I/Q skew and other non-linear effects of the transmitter components. The DPC block in this thesis is made up of following :

- Linear digital pre-compensation (L-DPC)
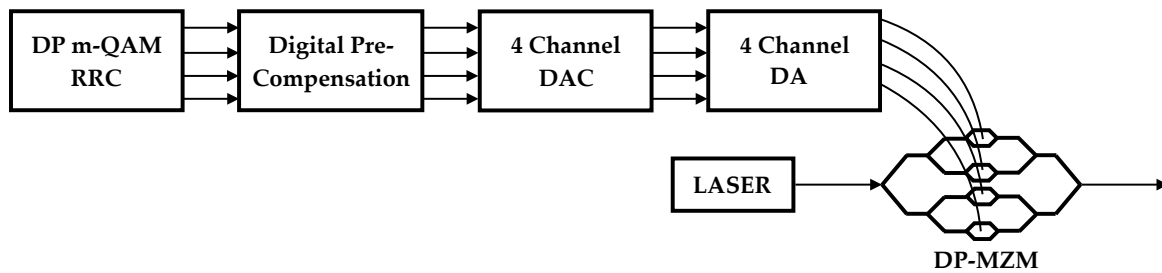
Figure 2.2: Digital pre-compensation at the transmitter DSP

- – Digital pre-emphasis (DPE) which overcomes only the 3-dB bandwidth limitation of the components
- – Transmitter I/Q skew compensation

- Digital pre-distortion (DPD) which overcomes additionally the non-linear effects of the components

In the remaining of the thesis, the above terminology is adopted when discussing the mitigation of linear and non-linear effects.

2.3 Related Works

One of the earliest works on electronic pre-equalization for coherent optical communication was conducted in [24–26] where a static pre-equalizer was implemented at the transmitter to generate RRC Nyquist pulses. In [24] pre-equalization of the the band-limiting effects of the arbitrary waveform generator (AWG) and the single-polarization Mach-Zehnder modulator (MZM) was carried out in the frequency domain. The transfer function of the AWG and MZM was measured under small signal driving condition, by exciting the components with 11 Gb/s 2^{15} De Bruijin PSK signals. Moreover, more than 100 measurements were conducted to get an accurate average of the frequency response of the transmitter.

In [26], the authors demonstrate transmission of 144 Gbit/s DP-64QAM signal. The transmitter, however, consisted of a single polarization MZM. In order to calculate the transfer function of the transmitter, 12 GBaud BPSK signals were sent in a back-to-back link with self-homodyne detection. The transfer function was obtained by comparing the fast fourier transform (FFT) of the transmitted and received signals. This process was done

only for one of the tributaries, i.e. the *I* channel of a QAM signal, and the same transfer function was used for the *Q* tributary. While such an assumption is quite normal, it can, however lead to improper compensation of the respective tributaries.

In [12], the frequency response of the DAC was measured by sending sinusoid waveforms at different frequencies. Additionally, the combined response of the transmitter at the output of the DP-MZM was measured and compared with the ideal Nyquist pulse sent at the input by comparing the two spectrums. The authors additionally noted that the bandwidth limitation was mainly due to the DAC. The pre-equalizer was implemented in the frequency domain to enable generation of 28 GBaud and 32 GBaud Nyquist RRC quadrature phase shift keying (QPSK) signals with 11.3 GHz bandwidth DAC. The signals were received with a 20 GHz analog bandwidth analog to digital converter (ADC).

The work in [21] reported on implementation of a non-linear pre-equalizer structure in front of the modulator for optical orthogonal frequency division multiplexing (OFDM) signals to linearize the output of the modulators used in high speed optical OFDM. The work was based on implementation of a DPD algorithm based on a polynomial model and an indirect learning structure.

This was followed by the work in [13], where spectral pre-emphasis for frequency components up to 20 GHz was implemented with a digital high pass filter to suppress the lower frequency components by 6 dB and demonstrate the generation of DP-64QAM 42.66 GBaud signals with high GSamples/second DAC. The signals were received with an ADC with 33 GHz bandwidth at 88 Gs/s. At the same time, the group [14], introduced the possibility of using the linear equalizers at the receiver combined with a decision directed least mean squares (DD-LMS) to estimate the frequency response of the transmitter in back-to-back setup with only single polarization and then implement a suitable time domain pre-equalizer structure at the transmitter.

In [9], the authors thoroughly investigated the impact of DAC bandwidth on system performance. In the same work, they proposed a novel DPE algorithm based on the measurement of the actual frequency response of the DAC. The desired frequency response filter is first initialized according to the symbol rate and then optimized based on the BER from the receiver through a feedback channel. The DPE filter was implemented in the frequency domain using 512 taps. Experimental results of the same were shown in [11] where Tera-bit transmission of 4 36 GBaud superchannel was demonstrated.

While work on this thesis was being developed, [10,17] were simultaneously published. In [10] the authors discussed a DPE scheme based on mean square error (MSE) approach which required the measurement of the electrical DAC frequency response. In [17], the

authors devised a DPD scheme using Volterra modelling of the transmitter components. They however, depend also on exclusive measurements of the DP-MZM characteristics. In the work, two different models were employed; one for the compensation of the DP-MZM and another for compensation of DAC and DA.

The authors in [16, 27, 28] also presented various low cost transmitter characterization approaches for DP-64QAM signals. The work [27] aimed at characterization of transmitter I/Q skew, bandwidth limitation and non-linear effects. The characterization was done sequentially for each tributary, i.e. for a dual-polarization setup, the measurement was carried out four times to get an estimate of the linear and non-linear effects.

In [16], the authors proposed receiver based monitoring and mitigation of transmitter impairments. In [28], the authors discussed a self-calibration scheme using low bandwidth components for measuring frequency response and time delay.

2.4 This Work

As mentioned in Sec.2.3, there were already various DPC methods present when work on the thesis begun. The main drawback of the reported methods is that they assume a precise knowledge of the frequency response of the DAC, DA and DP-MZM. Some of the methods measure just one of the tributaries and simply assume the same response for the other tributaries. In order to save time during calibration, the authors could assume an approximate typical frequency response for each of the tributaries and implement a DPC filter. Nonetheless, this would yield only sub-optimum performance due to the mis-match of the actual and the assumed transfer characteristics.

In addition to this, at the beginning of this thesis, to the best of author's knowledge, no work was published which had investigated the impact and compensation of transmitter I/Q skew and non-linear distortion in coherent optical communication transponders.

The proposed methods come with their own advantages and disadvantages. One advantage of the method published in [12] is the exact measurement of each of the tributaries by exciting the individual channels with sine waves of different frequencies and amplitude. But, nothing comes for free. Such an accurate measurement needs a longer time and additional hardware at the transmitter, which does not necessarily belong to the traditional transmitter design.

Experience has taught us that exact measurements of each of the components requires an additional step and is a time consuming process. Characterization of a single transpon-

der might be achieved without any great effort, but extending it to a higher number of transponders and for each of the four tributaries for a dual-polarization coherent system quickly escalates to a time and cost intensive task. Additionally, such characteristics often vary over baud rates, modulation formats and DP-MZM optical output power, which exacerbates the problem for multi-rate multi-format transceivers.

When reflecting on the proposed methods, and weighing the advantages and disadvantages of the suggested methods, it was realized that a fresh approach is needed to address the problem of DPC and design a method which is able to address the following two requirements :

- The new DPC method should avoid the need for any time-consuming measurement of the individual transmitter components.

- It should deliver a substantial system performance improvement by tackling all transmitter impairments at once.

2.4.1 Contributions

The main contribution of the thesis was the development of an adaptive accurate DPC scheme based on the indirect learning architecture (ILA) [18] and memory polynomial model of the transmitter [19, 20]. The main principle of the suggested DPC is shown in Fig. 2.3.

The adaptive DPC algorithm requires a feedback from the receiver. The algorithm makes use of two identical models H, one for training of the inverse system and the other for the pre-compensation. The training aims at minimizing the power of the error signal $e[n]$ by a least-squares algorithm. As $e[n]$ reaches zero, the training model synthesizes the inverse of the transmitter. If the optimal coefficients are copied to the pre-compensation block, the cascade of pre-compensation block and transmitter becomes the identity operator, and $y[n]$ becomes equal to $x[n]$.

Depending on the effects to be compensated i.e., linear or non-linear effects, a suitable model H is chosen and a corresponding DPC block is calculated. Once the inverse is synthesized, the filter coefficients are used for pre-distorting the input signal $x[n]$

The proposed algorithm is capable of estimation and joint mitigation of transmitter frequency response, I/Q skew and non-linear effects without any extensive calibration. The algorithm was verified with various experimental scenarios and results were reported in publications [15, 22, 29–36].
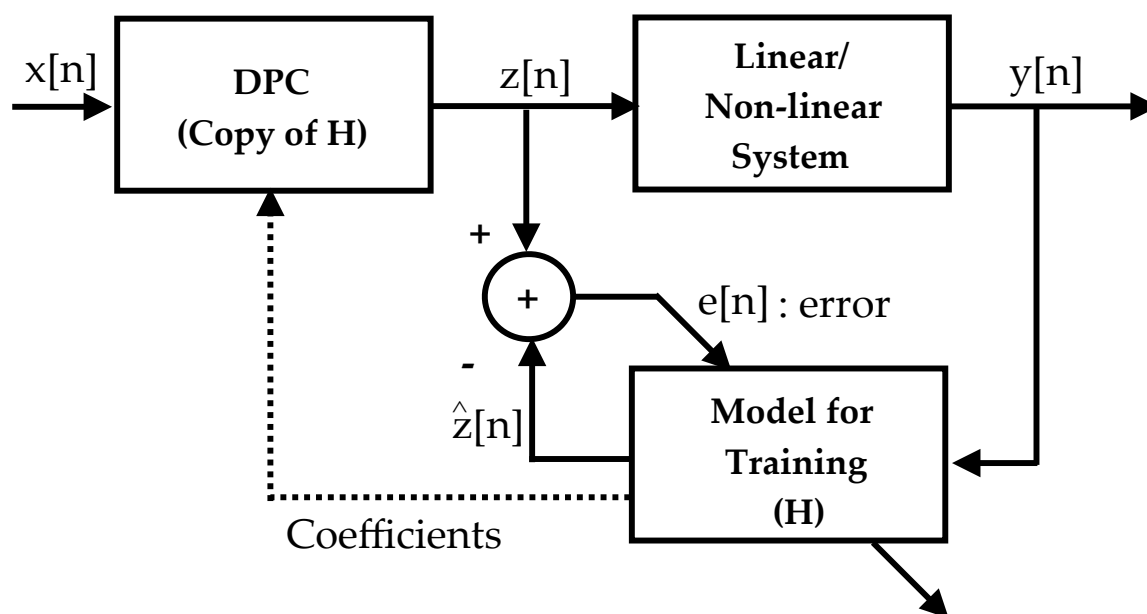
Figure 2.3: Principle of the DPC method.

For all the reported experiments, state-of-the-art transmitter components, designed for transmission of 32 GBaud signals were utilized.

This included an 88Gs/s 16 Ghz DAC with effective number of bits (ENOB) 5.5, an electrical DA with a bandwidth of 30 GHz and a DP-MZM with a 3-dB bandwidth of 23 GHz.

In [15], a linear model of the transmitter was considered and DPC was used to jointly mitigate the frequency response and transmitter I/Q skew in an electrical back-to-back scenario.

In [29], DPC was then extended to include DPD in an optical back-to-back setup. An additional polarization de-multiplexing block was introduced in this paper. Substantial gains were reported for modulation formats DP-4QAM to DP-64QAM over baud-rates up to 56 GBaud. It was also used in the long haul field trial transmission of terabit superchannels [37]

The DPD algorithm was applied to realize successful transmission of a DP-128QAM 569 Gbit/s (gross rate) single carrier signal with state-of-the-art components. In [33, 34], DPD coefficients were generated automatically without any prior measurements. This led to the demonstration of dense wavelength division multiplexing (DWDM) DP-64QAM and DP-128QAM 400G signals over a Telecom Italia legacy metro system, achieving a net spectral efficiency of 7.11 b/s/Hz. Additionally, various 200 Gbit/s configurations with DP-4QAM

at 57 GBaud, DP-8QAM at 42 GBaud and DP-16QAM at 33.01 GBaud were compared in the Telecom Italia field test environment.

Additionally, a memory polynomial based DPD to compensate for non-linear effects in high power transmitter components was evaluated in [22] and gains were reported for various transmit output powers for a DP-64QAM system.

Furthermore, a variant of the DPC where the DPC block receives feedback from a far end receiver was investigated in [34]. This was followed by an accurate estimation of the transmitter I/Q skew by implementing an additional phase noise compensation before the DPC block in [35]. An accuracy assessment of transmitter I/Q skew estimation was reported in [38].

3

Coherent Optical Communication Transponder Setup

In this chapter, a detailed description of a coherent optical communication system is given. After explaining the construction of the system, a thorough explanation of each of the components is provided.

Coherent optical communication system

The setup of a dual polarization coherent optical communication system is shown in Figure 3.1. The system is made up of several electronic, optical and electro-optic components. It consists of an optical transmitter part, a fiber channel and an optical receiver part [1]. Accompanying the hardware components at the transmitter and receiver are the DSPs.

The carrier in coherent optical communication systems is a LASER source at the transmitter. In order to exploit the two existing orthogonal polarization components of light, for transmitting data independently on both the polarizations, [1, 3] the LASER carrier is split into it's two orthogonal components, X and Y using a polarization beam splitter (PBS). The two split carriers , X and Y are then fed into a structure called the dual-polarization Mach-Zehnder Modulator (DP-MZM) which is made of two simple single MZM.

Digital modulating samples, $x_i[n]$, $i = (XI, XQ, YI, YQ)$ are generated by a suitable transmitter DSP. Here, X and Y denote the modulation of the two orthogonal polarization states of the carrier. The X and Y polarization can be modulated independently. The I and Q
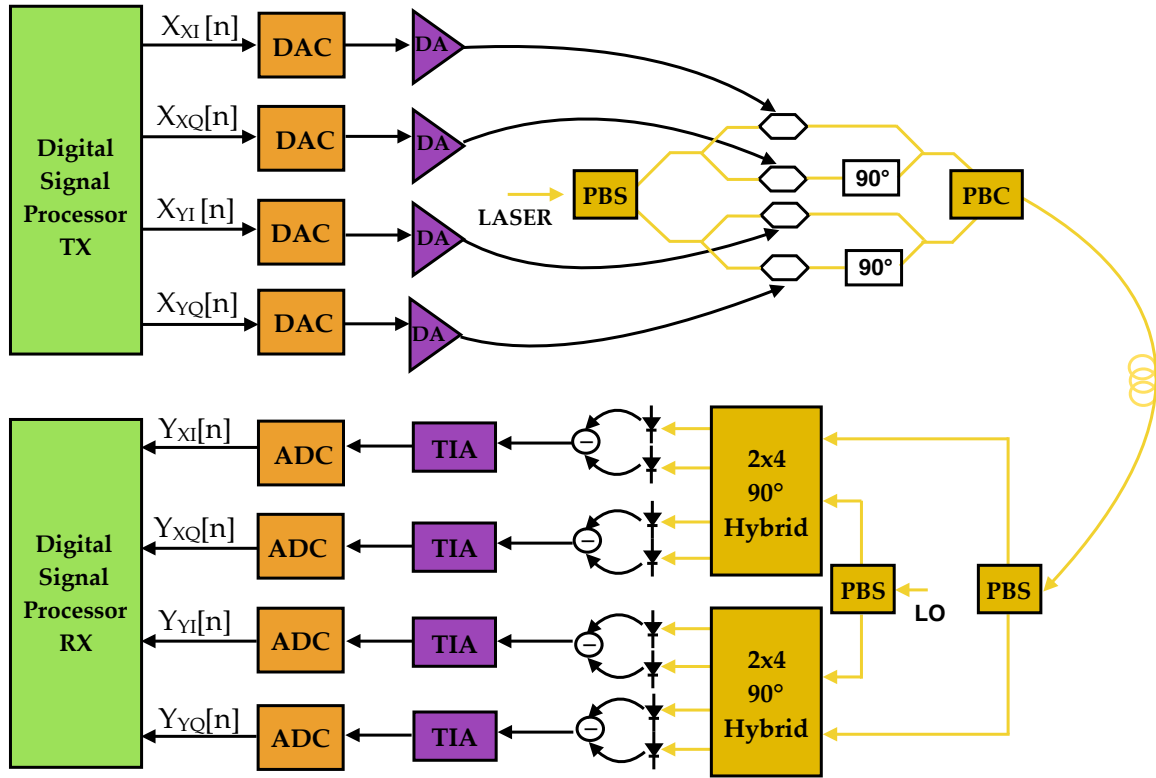
Figure 3.1: Coherent Optical Communication System

denote the inphase and quadrature components of the digital samples which modulate the *inphase* and *quadrature* components of the light carrier. The digital samples are first converted to analog signals by high sampling rates DACs, following which the signals get amplified by electrical DAs. The amplified signals then modulate the incoming light carrier with an I/Q modulator, which is a DP-MZM. After modulation, the two orthogonal signals are combined using polarization beam combiner (PBC) and sent in to a SSMF.

At the receiver, the optical signal is first split into two orthogonal polarizations using a polarization beam splitter (PBS). The signals are demodulated using a construction which consists of a LASER source and 2x4 90°hybrids. The demodulation can be achieved in three ways : intradyne, homodyne or heterodyne (explained in detail later). Photo-detectors convert the optical signal into electrical currents. The resulting electrical currents are amplified using transimpedance amplifier (TIA)s. A high sampling rate ADC converts the analog signal in to digital domain, after which finally the digital samples can be processed in the receiver DSP. Note that the black lines indicate the electrical connections and electrical signal. Optical path and signals are marked with yellow lines.

Transmitter Components

The role of the optical transmitter is to modulate the optical source with the information data and then send the corresponding modulated optical signal over the optical fiber. This section describes the components of the transmitter, the LASER, DAC, DA and DP-MZM in detail.

3.1 LASER

The LASER, acronym for "Light amplification of stimulated emission of radiation", is an essential component of a coherent optical transmitter. The major requirements for an optical source for a high data-rate optical communication transmitter are high optical output power and a narrow linewidth. While no optical source can be perfectly manufactured, the semiconductor LASER is a suitable candidate for high data rate systems. State of the art LASERs are capable of providing optical output power of up to 15-16 dBm with a linewidth of 100 kHz, and have a higher coupling efficiency into the SSMF in contrast to the low-cost light emitting diode (LED)s.

The principle of LASER operation is based on stimulated emission. Matter can interact with light in three possible ways which are known as absorption, spontaneous emission and stimulated emission. When a photon, with energy $h\vartheta$ and frequency ϑ is absorbed by an atom, the atom gets excited to a higher energy state. Such an excited atom can then return to its ground state through two ways; spontaneous emission or stimulated emission. During spontaneous emission, the emitted photons have random direction and phase characteristics compared to the original photon. In contrast, when a photon emission is stimulated by a photon, the emitted photon shares same the phase, frequency and polarization as of the original photon. Such a process then leads to generation of coherent light [1].

In order to maintain the stimulated emission process in a LASER, population inversion has to be achieved. This can be easily accomplished by forward biasing a direct band-gap p-n junction made up of GaAs or InP. Once the rate of stimulated emission exceeds the rate of absorption, the active region starts to exhibit an optical gain. In order to maintain this optical gain, the gain medium is placed in a Fabri-Perot cavity which consists of reflecting mirrors to maintain the optical feedback.

For high data rate coherent systems, single-longitudinal-mode LASERs are used. Such LASERs provide a stable carrier frequency, which is necessary for data transmission. In

optical systems, single-longitudinal-mode (SLM) lasers such as external cavity laser (ECL) and distributed feedback (DFB) lasers are also used. The ECLs provides higher output power with narrower laser linewidth ~100 khz which makes it appropriate for >100 Gbit/s transmission, but at the same time are more expensive. On the other hand, DFB lasers provide lower output power and broader linewidth ~10 MHz, which makes them cheaper but unsuitable for high data rate and high modulation order transmission.

For transmission, LASERs are operated in the carrier-wave mode [3] where the injection current, I is kept constant. This ideally enables a stable output of the LASER with constant amplitude, frequency and phase. Ideally, the output of a LASER is :

$$\underline{E}(t) = \left| \hat{\underline{E}} \right| \cdot e^{(j\omega_c t + \varphi_c)} \tag{3.1}$$

where $\left| \hat{\underline{E}} \right|$ is the amplitude of the carrier-wave LASER, ω_c is the angular frequency of the carrier wave and φ_c is a constant phase delay. In reality, however, a non-modulated optical carrier is modelled as :

$$\underline{E}(t) = \sqrt{\left| \hat{\underline{E}} \right|^2 + \left| \delta \hat{\underline{E}}(t) \right|^2} \cdot e^{(j\omega_c t + \varphi_c + \varphi_n(t))} \tag{3.2}$$

where the amplitude and phase have certain fluctuations due to the spontaneous emission processes [3]. The amplitude fluctuations give rise to intensity noise, $\left| \delta \hat{\underline{E}}(t) \right|^2$, which is negligible in most of the cases. On the other hand, the phase noise (PN) is non-negligible and has unfavorable effects on phase and coherent demodulation

The main cause of the PN are the random phase fluctuations in the LASER cavity. Due to these phase fluctuations, the power spectral density (PSD) of the LASER is not infinitely narrow and has a finite linewidth, Δf, also known as the laser linewidth (LLW). The PN can be modelled as a random walk process [3], given by Eq. 3.3.

$$\Delta \varphi_n(\tau) = \varphi_n(t + \tau) - \varphi_n(t) \tag{3.3}$$

where $\Delta \varphi_n(\tau)$ is a Gaussian random process, with :

$$\mathbb{E}[\varphi_n(t)] = 0 \tag{3.4}$$

$$\mathbb{E}[\varphi_n^2(t)] = 2\pi \cdot \Delta f \cdot \tau \tag{3.5}$$

where $\mathbb{E}[]$ is the expectation operator and τ is the time interval. The higher the LLW, the higher is the PN and the worse is the effect on the system performance [39]. Fig. 3.2

clearly shows the comparison between an ideal LASER and a LASER with finite LLW.
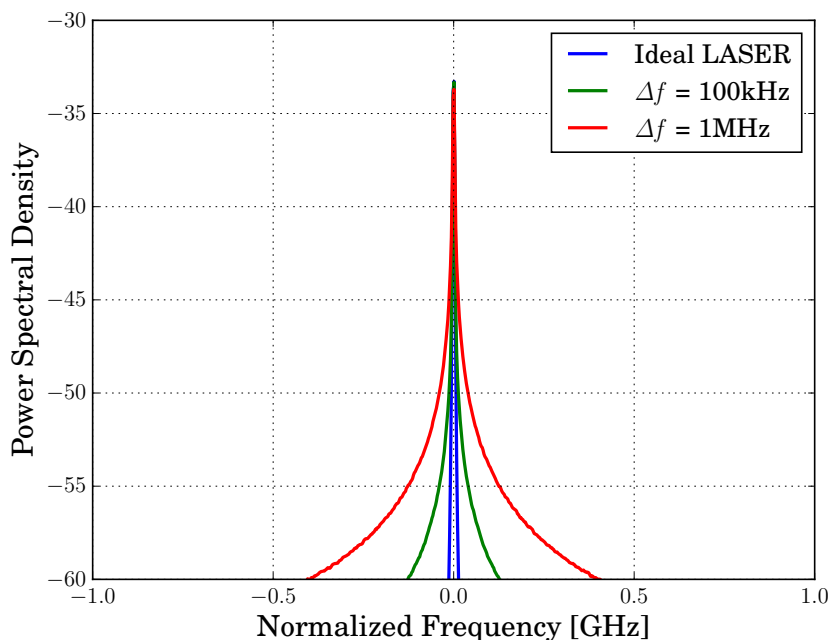
Figure 3.2: PSD of ideal LASER and LASER with different LLWs.

3.2 Digital to Analog Converter

DACs lie at the heart of an optical transponder. Digital data coming from the DSP is translated into the analog world using high data rate DACs. With the advancement in electronics, DACs enable various DSP operations at the transmitter, such as mapping of modulation data to amplitude and phase, pulse shaping, bandwidth and transmitter I/Q skew pre-compensation, pre-distortion of various transmitter non-linearities [5, 9].

Ideal DAC

Figure 3.3 illustrates the working of a DAC in time and frequency domain. Basically, the DAC has to acquire the digital data and convert it into the analog signal shown in Figure 3.3(b). This can be achieved by first converting the digital data into an impulse train, $x_p(t)$ shown in Figure 3.3(c). Sampling in time domain results into several replicas of the original frequency domain signal, as depicted in the frequency domain of Figure 3.3(c).

The analog re-construction of the digital signal is governed by the principles of Nyquist theorem [40] which states that a band-limited continuous-time signal $x(t)$ with highest frequency component f_m can be fully recovered from its discrete time sequence $x[nT_s]$, if:

$$f_s >= 2 \cdot f_m \tag{3.6}$$

$$f_s = 1/T_s \tag{3.7}$$

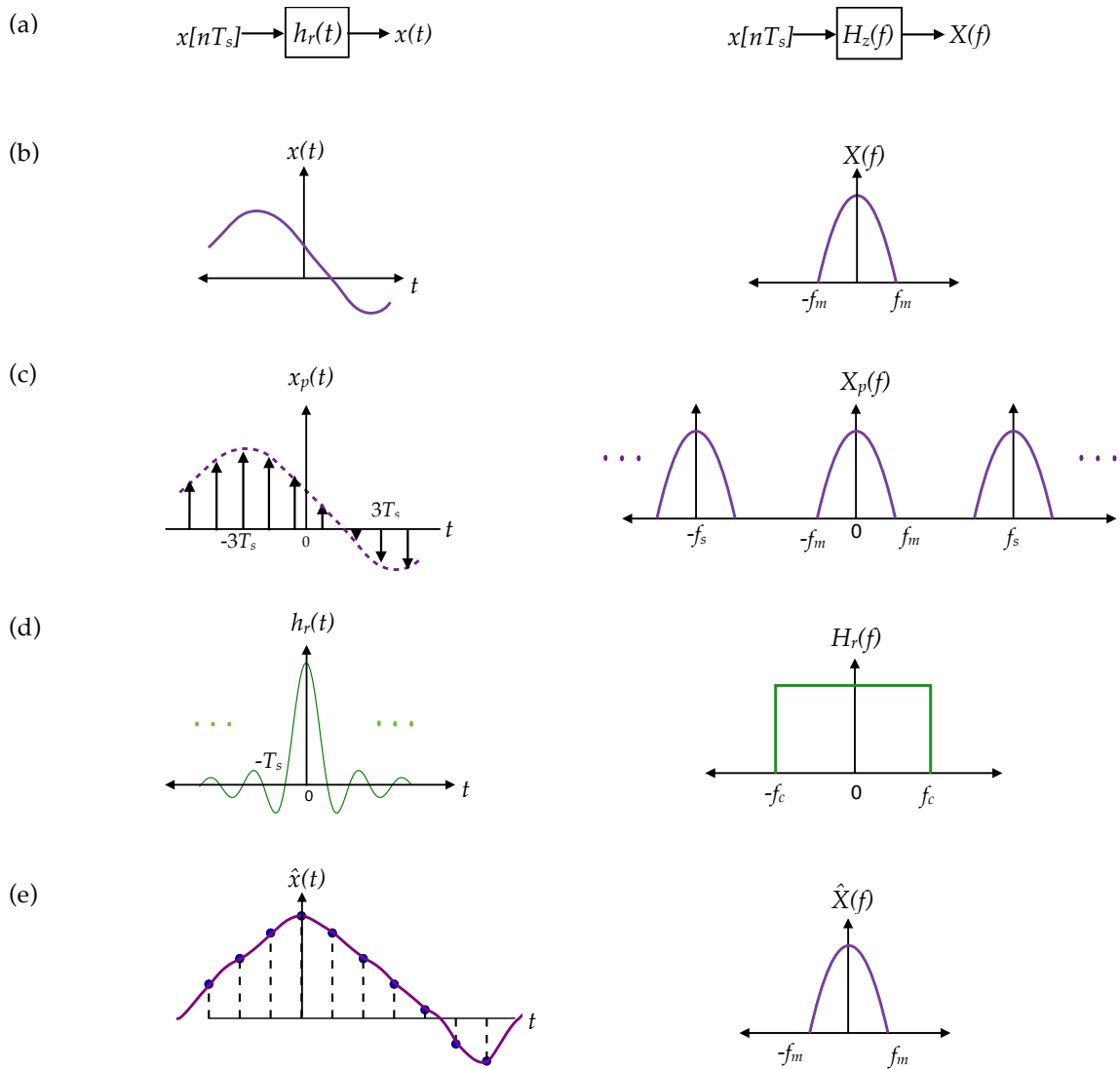where T_s is the sampling interval and f_s is the sampling frequency.

Figure 3.3: Time and frequency domain representation of an ideal DAC.

The analog signal is reconstructed from the impulse train $x_p(t)$ by passing it through a

reconstruction filter $h_r(t)$. This reconstruction filter is a *brick-wall filter* in the frequency domain with a cut-off frequency f_c, such that :

$$f_s = 2f_c; \quad T_s = \frac{1}{2f_c} \tag{3.8}$$

with a transfer function

$$H_r(f) = \begin{cases} \frac{1}{2f_c}, & |f| \leq f_c \\ 0, & |f| > f_c \end{cases} \tag{3.9}$$

and an impulse response, which is a *sinc* in time domain given by the equation :

$$h_r(t) = si\,(\pi t/T_s) = \frac{sin\,(2\pi f_c t)}{2\pi f_c t} \tag{3.10}$$

The impulse train $x_p(t)$ is written as :

$$\sum_{n=-\infty}^{\infty} x[n]\delta(t - nT_s) \tag{3.11}$$

and the reconstructed output $\hat{x}(t)$ is the convolution of $x_p(t)$ with the reconstruction filter, $h_r(t)$ in time domain, calculated as :

$$\hat{x}(t) = \sum_{n=-\infty}^{\infty} x[nT_s]h_r(t - nT_s) \tag{3.12}$$

$$= \sum_{n=-\infty}^{\infty} x[nT_s]\frac{sin\,(\pi(t - nT_s)/T_s)}{\pi(t - nT_s)/T_s} = x(t) \tag{3.13}$$

A closer look at Eq. 3.10 will tell the reader that the ideal reconstruction filter has an infinite length impulse response, and is non-causal. Such an ideal sinc filter does not exist in reality. A practical DAC is then realized by employing a *zero-order hold circuit* at the output. The DACs then function by holding the last value until a new sample is received.

Practical DAC

Fig.3.4 shows the output of a practical DAC in time and frequency domain. Since, *impulse trains* cannot be constructed practically in real systems, a *zero-order hold circuit* is implemented to generate a rectangular pulse with width T_s and unity height. The spectrum of
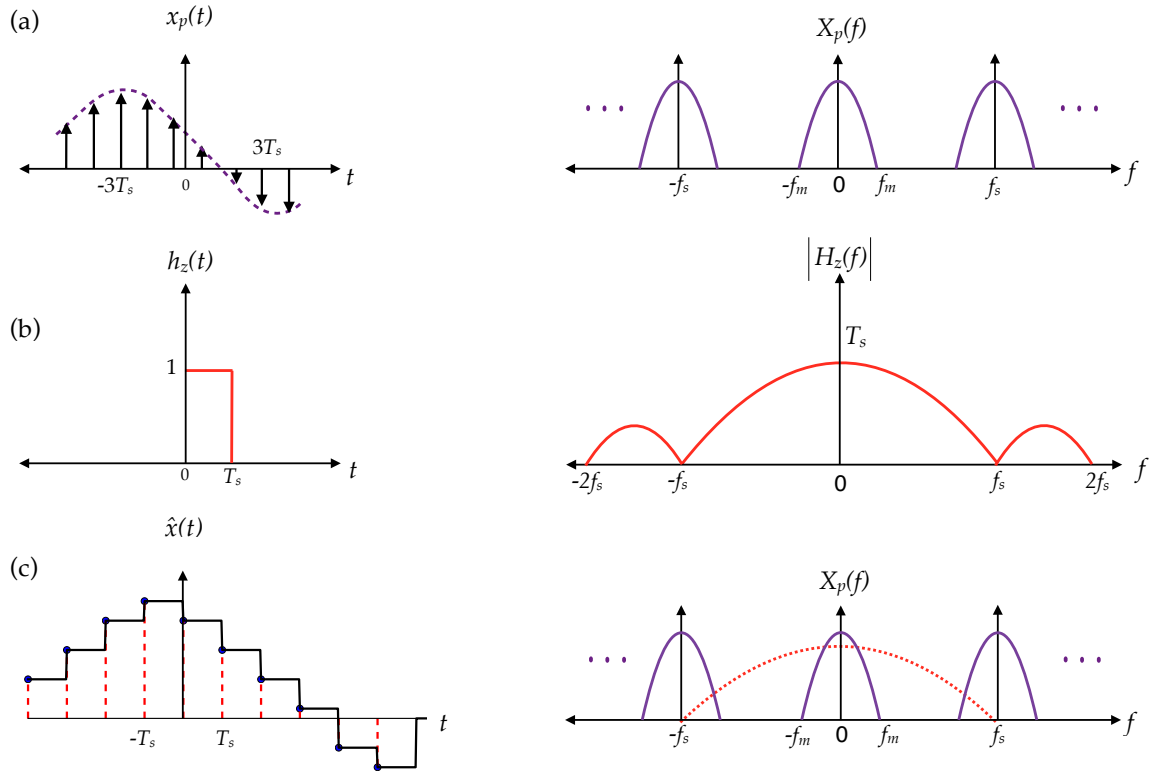
Figure 3.4: Time and frequency domain representation of a practical DAC.

the rectangular pulse is shown in Figure 3.4(b), which is a sinc pulse given as :

$$H_z(f) = T_s \cdot si(\pi f/f_s) \cdot e^{-j\pi f \, T_s} \tag{3.14}$$

The convolution of the impulse train with the *zero − order hold* circuit leads to the staircase form plotted in Figure 3.4(c). In the frequency domain, the convolution becomes a simple multiplication of $H_z(f)$ and $X(f)$ resulting into the reconstructed signal, $\hat{X}(f)$ which is a distorted copy of the original analog signal, $X(f)$. The output suffers from unwanted spectral signals which occur at multiples of sampling frequency, f_s. Additionally, there is also amplitude distortion in the resulting spectrum. In order to overcome these spectral bands, *smoothing filter*s are used at the output of practical DACs. Such filters remove the undesirable spectral components and additionally perform a post-equalization of the low amplitude at higher frequencies.

3.3 Driver amplifier

The next electronic component in the transmitter chain is the electrical driver amplifier (DA). Electrical DAs are needed to drive the LiNbO_3 modulators which are often characterized by their drive voltage V_π. V_π is the voltage required by a modulator to induce a phase change of 180°. In order to obtain efficient modulation and reduce modulation loss, modulators have to be driven in the range from 0 - $2V_\pi$ (more explanation in Section 3.4).

The output signals produced by the DACs however, are in the range of 100 mV$_{p-p}$ to 500 mV$_{p-p}$, with some DACs recently released reaching 1.3 V$_{p-p}$ [41]. Such low voltages are not enough to drive the MZMs which typically have a V_π of 3-4V$_{p-p}$ [42]. The DP-MZM used in this thesis has a V_π of 3.5 V [42].

In order to improve the signal to noise ratio (SNR) and the modulation efficiency of the MZM, the output signal of the DACs are amplified using electrical DAs. The electrical amplification guarantees a good signal quality and sufficient driving voltage to generate phase modulated signals such as DP-m QAM.

For the thesis, the analog output of the DACs had a range of 0.2-0.5 V_{p-p} and depending on the chosen analog driving gain, the DAs could produce output driving signals from 3-6 V_{p-p} for an input of up to 1 V_{p-p}.

3.4 Dual polarization Mach-Zehnder Modulator

Generation of higher data rate optical pulses is achieved by using a device called a Mach-Zehnder Modulator. The MZM is an opto-electronic device which enables external modulation of the optical signal emitted from a LASER. Owing to their reliable modulation capabilities to modulate phase and intensity of the optical field, LiNbO_3 MZMs are the preferred choice of modulators for transmission of higher data rate optical signals such as 100 Gbit/s and 400 Gbit/s [8].

3.4.1 Principle

The structure of a MZM is based on a Mach-Zehnder Interferometer and the working of the MZM is dependent on the Pockels effect. The Pockels effect is a phenomenon which describes the modification of refractive index of a waveguide as a function of the applied electrical voltage. As the refractive index of the waveguide changes, a change in the phase of optical signal travelling through this waveguide is induced. This change in phase of the

propagating light waves can then be used to modulate the incoming optical light based on interference and destruction of light waves.

Figure 3.5 shows the structure of a MZM. It consists of a LiNbO$_3$ waveguide and two electrode plates where external voltages $v_1(t)$ and $v_2(t)$ are applied [43]. As the applied electric voltage is changed, the LiNbO$_3$ waveguide induces a phase shift in the incoming optical signal. Incoming light from the LASER is defined as :

$$\underline{E}_{in}(t) = \hat{\underline{E}} \cdot e^{(j\omega_c t)} \tag{3.15}$$

As seen from the structure, the optical light power from LASER is split in to the two arms with a splitting ratio ϵ. Electric field at the output of the first Y-junction is given as :

$$\underline{E}_1(t, z = 0) = \epsilon_1 \cdot \hat{\underline{E}}(t) \cdot e^{(j\omega_c t)} \tag{3.16}$$

$$\underline{E}_2(t, z = 0) = \sqrt{1 - \epsilon_1^2} \cdot \hat{\underline{E}}(t) \cdot e^{(j\omega_c t)} \tag{3.17}$$
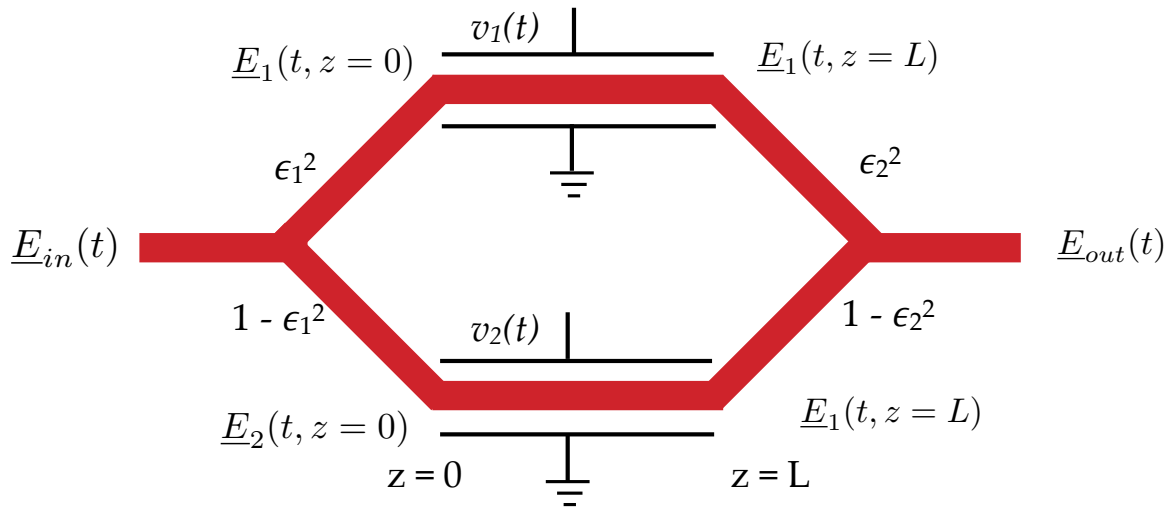

Figure 3.5: Structure of a LiNbO$_3$ MZM

The split electric fields then travel through the waveguide and depending on the applied voltage, a phase shift of $\Delta\phi_1(t)$ and $\Delta\phi_2(t)$ is induced on arm 1 and arm 2 respectively. The electric field at the input of the second Y-junction is then calculated as :

$$\underline{E}_1(t, z = L) = \underline{E}_1(t, z = 0) \cdot e^{(-j\Delta\phi_1(t))} \tag{3.18}$$

$$\underline{E}_2(t, z = L) = \underline{E}_2(t, z = 0) \cdot e^{(-j\Delta\phi_2(t))} \tag{3.19}$$

At the output of the second Y-junction, the combined electric field, $\underline{E}_{out}$ is written as the weighted sum of the electric field,

$$\underline{E}_{out}(t, z = L) = \epsilon_2 \cdot \underline{E}_1(t, z = L) + \sqrt{1 - \epsilon_2^2} \cdot \underline{E}_2(t, z = L) \tag{3.20}$$

which can be finally written as a function of input electric field as

$$\underline{E}_{out}(t, z = L) = \hat{\underline{E}}(t) \cdot e^{(j\omega_c t)} \Big[\epsilon_1 \cdot \epsilon_2 \cdot e^{(-j\Delta\phi_1(t))} + \sqrt{1 - \epsilon_1^2} \cdot \sqrt{1 - \epsilon_2^2} \cdot e^{(-j\Delta\phi_2(t))} \Big] \tag{3.21}$$

For equal power splitting ratio, Equation (3.21) reduces to

$$\underline{E}_{out}(t, z = L) = \frac{1}{2} \cdot \hat{\underline{E}}(t) \cdot e^{(j\omega_c t)} \Big[e^{(-j\Delta\phi_1(t))} + e^{(-j\Delta\phi_2(t))} \Big] \tag{3.22}$$

which can be further written as

$$\underline{E}_{out}(t, z = L) = \frac{1}{2} \cdot \hat{\underline{E}}(t) \cdot e^{(j\omega_c t)} \cdot e^{-j(\frac{\Delta\phi_1(t)+\Delta\phi_2(t)}{2})} \Big[e^{-j(\frac{\Delta\phi_1(t)-\Delta\phi_2(t)}{2})} + e^{j(\frac{\Delta\phi_1(t)-\Delta\phi_2(T)}{2})} \Big] \tag{3.23}$$

after re-arranging,

$$\underline{E}_{out}(t, z = L) = \hat{\underline{E}}(t) \cdot e^{(j\omega_c t)} \cdot \cos\left(\frac{\Delta\phi_1(t) - \Delta\phi_2(t)}{2}\right) \cdot e^{-j(\frac{\Delta\phi_1(t)+\Delta\phi_2(t)}{2})} \tag{3.24}$$

The phase changes brought about by changing the electric voltages, $v_1(t)$ and $v_2(t)$, are linearly related to the voltages and can be described by

$$\Delta\phi_1(t) = \frac{\pi}{V_\pi} \cdot v_1(t) \tag{3.25}$$

$$\Delta\phi_2(t) = \frac{\pi}{V_\pi} \cdot v_2(t) \tag{3.26}$$

where V_π is a constant known as the drive voltage of the MZM. It is defined as the voltage difference for which the phase difference $\Delta\phi_1(t) - \Delta\phi_2(t)$ becomes 180°.

Substituting Equation (3.25) and Equation (3.26) in Equation (3.24), the following expression for $\underline{E}_{out}$ at the MZM is obtained,

$$E_{out} = \hat{\underline{E}}(t) \cdot e^{(j\omega_c t)} \cdot \cos\left(\frac{\pi}{V_\pi} \cdot \frac{v_1(t) - v_2(t)}{2}\right) \cdot e^{-j\frac{\pi}{2V_\pi} \cdot (v_1(t) + v_2(t))} \tag{3.27}$$

where the $\cos\left(\frac{\pi}{V_\pi} \cdot \frac{v_1(t) - v_2(t)}{2}\right)$ determines the intensity modulation of the optical field and the $e^{-j\frac{\pi}{2V_\pi} \cdot (v_1(t) + v_2(t))}$ term decides the phase modulation.

In order to avoid the chirp arising from the phase modulation term, MZMs are operated in a push-pull mode. With $v_1(t) = -v_2(t) = v(t)/2$, pure intensity modulation is obtained [44]. However, a perfect chirp free modulation is still not achievable due to the inherent asymmetry in the MZM structure [45]. Assuming that the applied data voltages on the two arms are perfectly matched and the data on one of them is inverted, Equation (3.27) is then written as,

$$E_{out} = \hat{\underline{E}}(t) \cdot e^{(j\omega_c t)} \cdot \cos\left(\frac{\pi}{V_{pi}} \cdot \frac{v(t)}{2}\right) \tag{3.28}$$
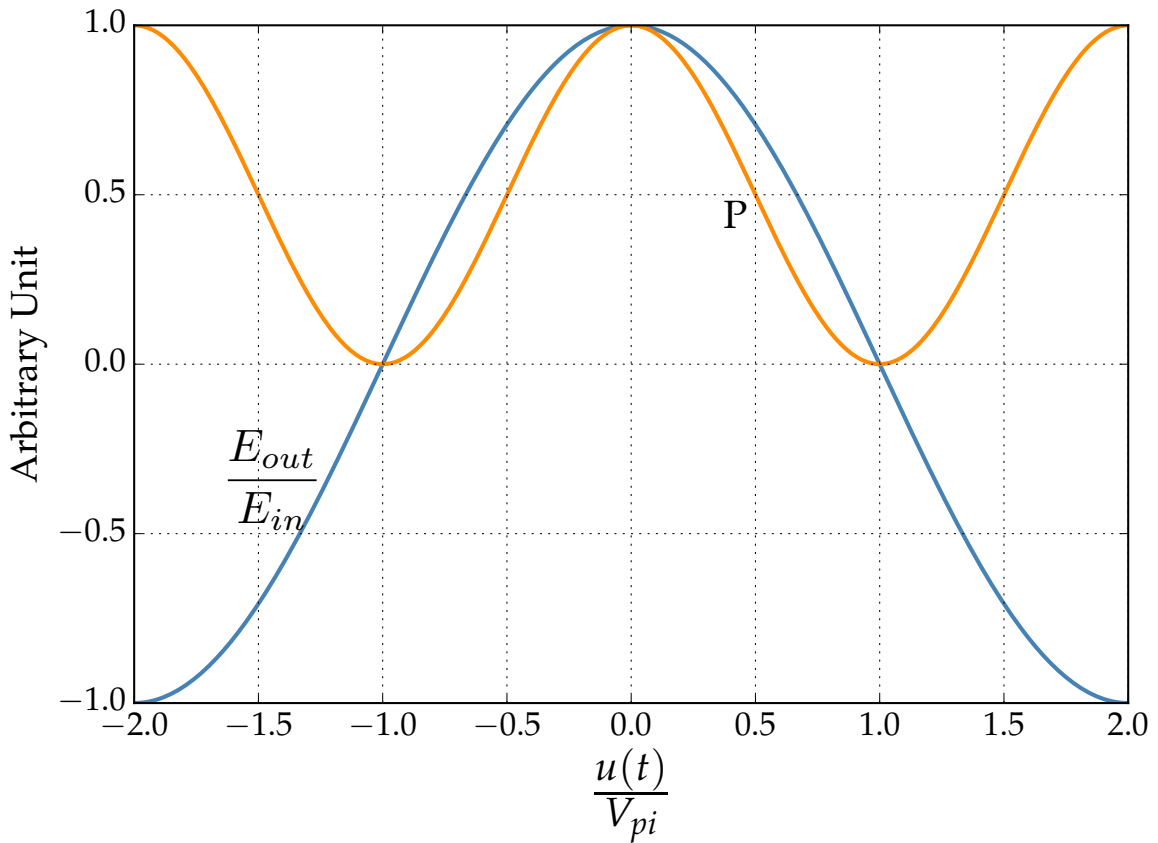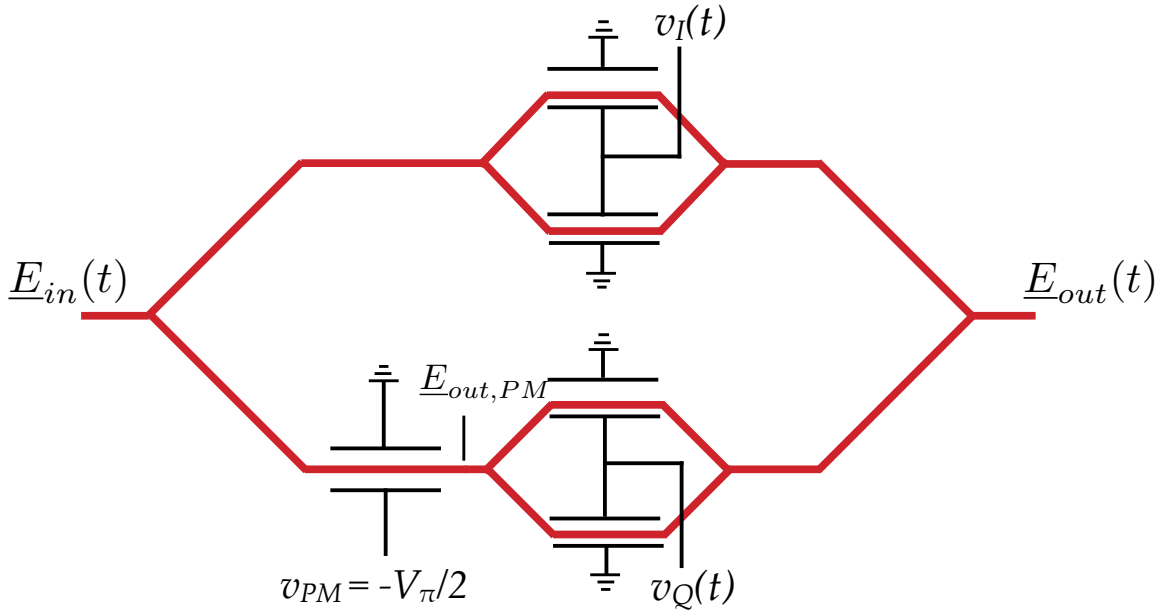

Figure 3.6: MZM electric field and power transfer characteristics.

The electric field and power transfer characteristics of the MZM are plotted in Figure 3.6.

Figure 3.7: Structure of an I/Q LiNbO$_3$ MZM

The normalized electric field follows the graph of the cosine function and the power, *P* which is the normalized power, can be calculated as,

$$P(t) = |\underline{E}_{out}|^2 = \left|\hat{\underline{E}}(t)\right| \cos^2\left(\frac{\pi}{V_{pi}} \cdot \frac{v(t)}{2}\right) \tag{3.29}$$

Depending on the region of operation, the MZM can be used to generate various modulation schemes. This is controlled by deciding on the *bias* point of the MZM and then choosing the required modulation voltage.

3.4.2 Generation of m-QAM signals

MZMs are also used in coherent optical communication transmitter system to generate m-QAM signals. One MZM can modulate only the in-phase component of the optical light. In order to modulate the quadrature component, a second MZM is used in parallel [3]. The construction of a single polarization I/Q MZM is shown in Figure 3.7.

A parallel arrangement of two MZMs is used to modulate two orthogonal optical carriers. The incoming electric field, $\underline{E}_{in}(t)$ is split in to two parts. One of the paths has an extra phase modulator, which introduces a permanent 90° phase shift between the upper and lower electric fields. Then, for :
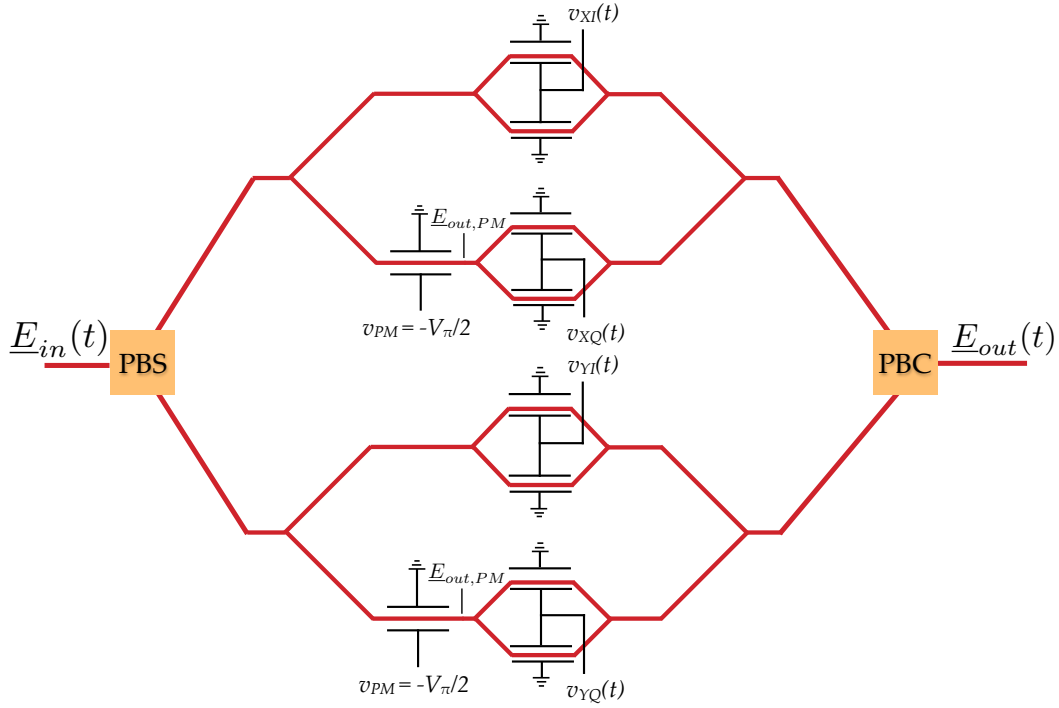
Figure 3.8: Structure of a Dual Polarization I/Q LiNbO$_3$ MZM

$$\underline{E}_{in}(t) = \hat{\underline{E}} \cdot e^{(j\omega_c t)} \tag{3.30}$$

$$\underline{E}_{out,PM} = \frac{\hat{\underline{E}}}{\sqrt{2}} \cdot e^{(j\omega_c t)} \cdot e^{-j\frac{\pi}{V_\pi} \cdot v_{PM}} \tag{3.31}$$

From Equation (3.28) and Equation (3.31), the output at the I/Q MZM is written as,

$$\underline{E}_{out}(t) = \hat{\underline{E}}_{out} \cdot \left[cos\left(\frac{\pi}{2} \cdot \frac{v_I(t)}{V_{pi}}\right) + jcos\left(\frac{\pi}{2} \cdot \frac{v_Q(t)}{V_{pi}}\right) \right] \cdot e^{(j\omega_c t)} \tag{3.32}$$

3.4.3 Generation of DP-m QAM signals

DP-m QAM (where *m* is the order of modulation) can be produced by an arrangement of MZMs as shown in Figure 3.8. The output of a LASER source is a linearly polarized light, consisting of two orthogonal polarizations, namely X and Y. As shown in the Figure 3.8, the incoming electric field from the LASER, $\underline{E}_{in}$ is split in to the two polarizations using a PBS.

Each polarization is then independently modulated with the digital data with an I/Q

MZM. Depending on the modulation voltages, various m-QAM (where $m = 2^n$ for n = 1, 2, 3..) modulation formats can be produced. After the individual and independent modulation on both the top and bottom I/Q MZM, the electric fields are combined using a PBC. The output electric field is then a DP-m-QAM signal.

The process of generation of the DP-m-QAM signals in this thesis was carried out using the principle of DP-MZM as explained in this section with LiNbO_3 technology. State-of-the-art LiNbO_3 modulators are able to support baud rates up to 64 GBaud with a V_π of 3.5 V and 3-dB bandwidth of 35 GHz making transmission of 400 Gbit/s on a single wavelength possible. There is, however, another class of MZMs which is based on the InP technology [46]. In comparison to LiNbO_3, these devices can potentially offer a lower V_π, smaller size and higher bandwidth [47] which make them an attractive alternative for the next generation power and cost-efficient coherent systems.

3.5 Transmitter Limitations

In the previous section, the major components of a high data rate optical communication were introduced and studied. These comprise of :

- A high sampling rate and bandwidth DAC

- A high bandwidth and linear electrical driver amplifier DA

- A dual polarization Mach-Zehnder modulator

Each of these electronic and opto-electronic components are not ideal and hinder system performance through their imperfections. While the high sampling rate DAC has been a technology enabler in transmitting DP-mQAM constellations with high baud rate (> 32 GBaud), it comes with its own limitations. The DA is the second electronic component in the chain which further deteriorates the analog electric signal when driven at higher gains. The DP-MZM is also a non-linear device which additionally impedes the transmitter output integrity.

The three major limitations of optical transmitters when driven at high data rates and modulation formats are :

- 3-dB bandwidth limitation

- Transmitter I/Q skew in each polarization

- Non-linear effects
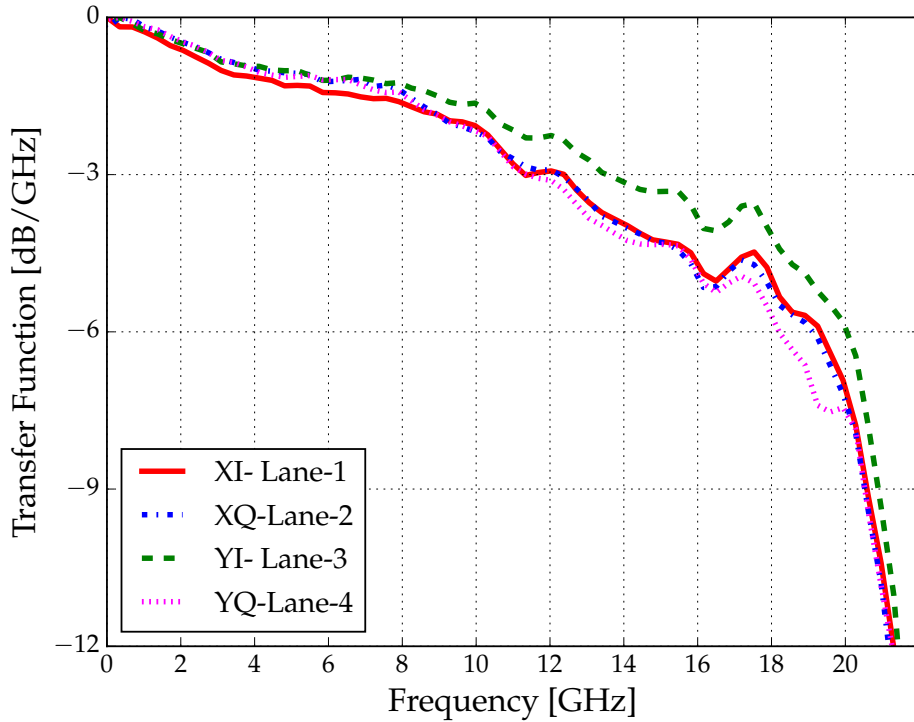
Figure 3.9: Transfer function of a 4-channel DAC for 32 GBaud transmission

3.5.1 Bandwidth Limitation

All the electrical and optical components of a coherent transponder system have a constitutional limitation arising from their bandwidth. The bandwidth of a system is defined as the band of frequencies which are allowed to pass through it when excited with a wideband input source. In this respect, the 3-dB bandwidth mark is considered an important figure-of-merit for qualification of various electronic components.

3-dB bandwidth plays a key role in design of coherent optical transponders [9, 10]. As data rates grew from 10 G to 600 G, so did the bandwidth demand of the underlying DACs, DAs and DP-MZM. Alas, the electronics industry doesn't grow at the same pace as the demands from the optics industry. For the transmission of 32 GBaud signals, DACs with bandwidth of approximately 16 GHz were made available in the market [48]. This was followed by an introduction of a 30 GHz analog bandwidth DAC [41] for the transmission of 64 GBaud signals, which is likewise insufficient for the generation of 64 GBaud signals without adequate DSP at the transmitter.

Transfer characteristics of one such DAC exemplar are shown in Figure 3.9. The DAC
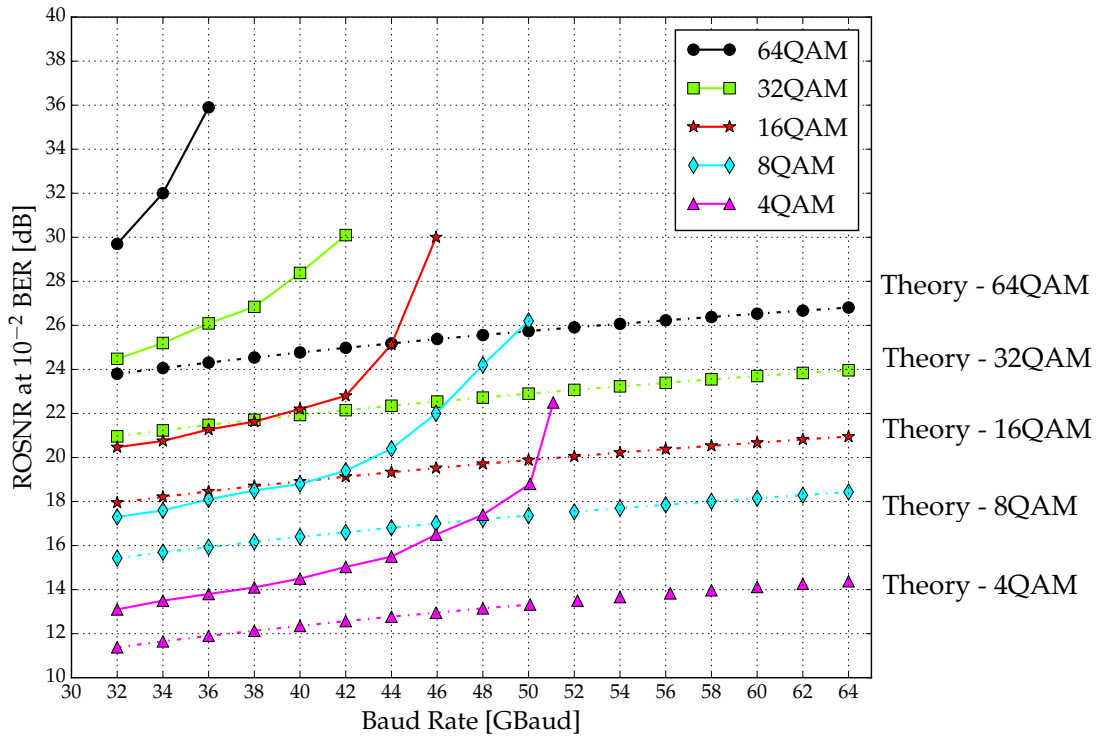
Figure 3.10: Required optical signal to noise ratio (ROSNR) as a function of increasing baud rate across various modulation formats

has 4 channels, viz. XI, XQ, YI and YQ signifying the respective lanes for a dual polarization signal. The transfer characteristics are obtained by stimulating the DAC with white noise digital signals and then capturing the output signal with a high sampling rate oscilloscope with 23 GHz bandwidth and 50 Gs/s sampling rate. The output digital signal is compared with the input signal and the respective transfer functions are obtained by finding the difference in the PSDs of the input and output signals of the individual tributaries.

Looking at the graph, the following two observations can be readily made:

1. The 4 lanes have a 3-dB bandwidth limitation and the 3-dB bandwidth for all the lanes lies between 12-14 GHz.

2. The 4 lanes have different transfer characteristics leading to different signal quality on the four lanes.

In [9,10], authors made deep simulation investigations on the impact of DAC bandwidth on the transmission performance of baud rates higher than 30 GBaud.

In this thesis, for the system under test, an experimental analysis of the impact of increasing baud rate due to transmitter limitations was carried out. The measured results of the same are plotted in Figure 3.10 (shown with continuous lines). The graph is evaluated for the DAC, the transfer characteristics of which are plotted in Figure 3.9. The DA has a high bandwidth of 30 GHz and the DP-MZM has a bandwidth of 23 GHz. In general, the transponders are limited by the DAC bandwidths, since their DA and DP-MZM counterparts normally have greater 3-dB bandwidths.

Theoretical curves are also drawn. As seen, for every modulation format, doubling the baud-rate increases the ROSNR by 3 dB. At the same baud-rate, greater OSNR is required for the higher modulation formats, due to the transmission of more number of bits/symbol, leading to higher energy requirements per bit. The measured ROSNR follows the trend of the theoretical results up to a point after which it escalates. This trend is distinguishable for all the modulation formats. What is more interesting to note is that even though state-of-the-art components have barely 16 GHz bandwidth, transmission of up-to 50 GBaud signals with DP-4QAM is feasible (provided a strong FEC is utilized).

The trend is, however, clear that increasing the baud-rate for a fixed transmitter bandwidth leads to signal degradation and ultimately results in a higher ROSNR for quality transmission. Component bandwidth limitations hence, is one of the critical issues to deal with for present and next generation power and cost efficient optical transponder systems.

3.5.2 Transmitter I/Q skew

The next linear effect arising from the transmitter components is the transmitter I/Q skew. Transmitter I/Q skew is defined as the different group delay between the in-phase (I) and quadrature (Q) components of a QAM signal. The root cause of this effect lies in the unequal lengths of physical interconnections used in the transmitter to connect various components, circuit paths and/or uneven transfer characteristics of the components.

Work on transmitter I/Q skew was barely done before the start of this thesis and transmitter I/Q skew was never quite considered. Transmitter I/Q skew is an effect which becomes crucial for higher baud rates. Up until the optics community was considering bit rates of 10 Gbit/s and 40 Gbit/s in legacy systems, the consequences of un-equalized I/Q skew never posed any problems. It, however, became a critical impairment when 100 Gbit/s and 400 Gbit/s systems were being developed.

Transmission of higher modulation formats such as DP-64QAM and DP-128QAM with high baud rates (> 32 GBaud) requires higher OSNR at the end of the link for successful

detection. For such a system, it is inevitable to optimize each and every parameter in the system chain. There should absolutely be no penalty or loss introduced due to the effects which are deterministic and can be mitigated with efficient signal processing.
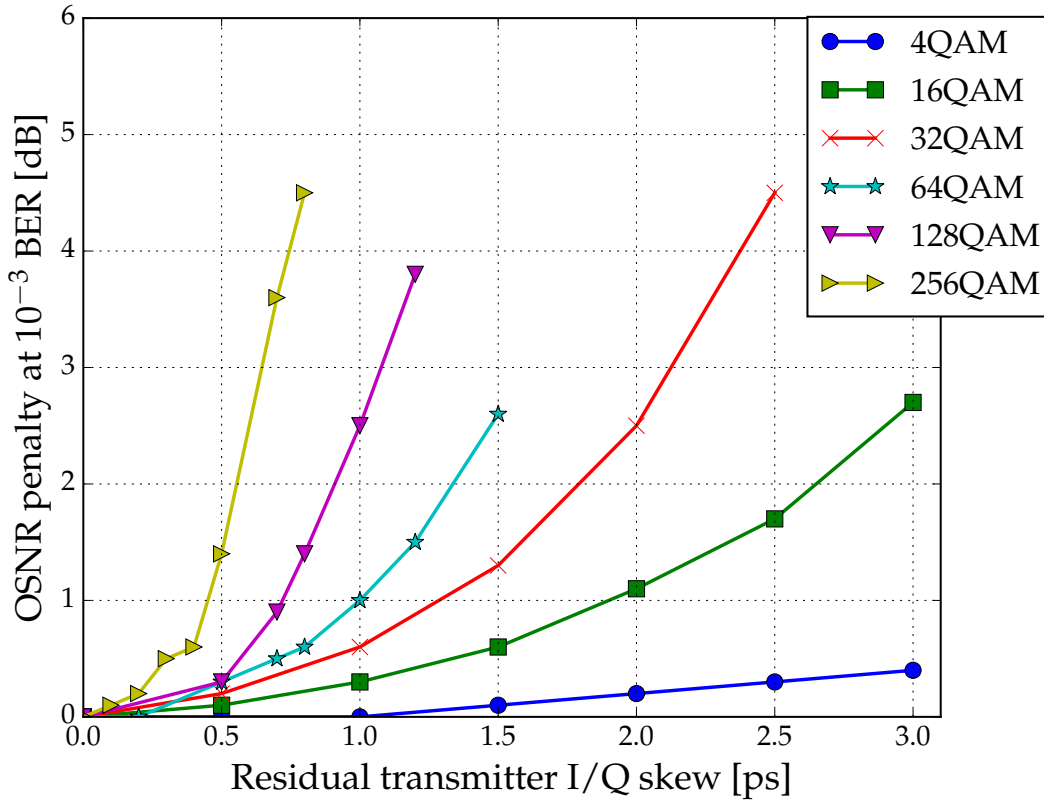
Figure 3.11: Effect of transmitter I/Q skew on OSNR for 37.41 GBaud signals

Figure 3.11 shows the OSNR penalty at a BER of 10^{-3} suffered by various modulation formats for 37.41 GBaud signals in simulations. For DP-4QAM signals, there is a gradual increase in the penalty as the residual transmitter skew increases from 0 ps to 3 ps. However, the penalty is almost negligible, only becoming significant for skew > 3 ps.

As the modulation format increases, the penalty rapidly increases. For DP-64QAM signal, there is almost a 3dB penalty for a skew of < 1.5 ps. The explanation for higher modulation formats suffering more from transmitter I/Q skew lies in the fact that these modulation formats are more densely packed and hence more susceptible to inter symbol interference (ISI) resulting from the skew. For DP-128QAM, a residual skew of 1.5 ps can lead to a OSNR penalty of > 5 dB. If overlooked, transmitter I/Q skew can undermine the

performance of the system and thus should be estimated and compensated in present and next-generation optical systems.

3.5.3 Non-linear effects

Non-linear effects are inherent to all electronic and opto-electronic components. While the linear effects such as bandwidth limitation and transmitter I/Q skew are always present, non-linear effects only surface when the components are operated in high power regions.

Conventionally, coherent systems are preferred to be operated in the linear regime, by keeping the gain of the DA small, and hence controlling the driving voltage to the MZM to enable the transmission of the symbols in the linear part of the MZM. Transmission in linear regime guarantees a low BER. At the same time, this causes a low transmit power and OSNR. Particularly, in WDM systems, which suffer from additional filter losses, the quality of transmit signal degrades significantly even before reaching the first booster amplifier. This forces the use of per channel EDFAs, which adds further to the cost and complexity of the transponder. This motivates the functioning of the components in the non-linear region, which comes with its own set of problems.

The transmission in the non-linear regime is more power and OSNR efficient, but it is riddled with various non-linear effects. When driven with higher input voltages, DAs exhibit the well-known phenomena of gain saturation which ultimately leads to output signal compression [19, 49]. For a higher input signal, the output remains the same, and the extra power is dissipated in the non-linear harmonics which are generated as a by-product [50]. The DP-MZM has a constitutional cosine curve (as explained in Section 3.4).

When the input driving voltages are increased, the MZM enters the non-linear part of the cosine [17, 21, 22, 27, 51]. The consequences of this is depicted in Figure 3.12. The output power at the MZM is increased by increasing the analog gain of the electrical DA. Ideally, for an increase in the transmit output power, there would be an increase in transmit OSNR and then BER should fall leading to low ROSNR. As we see, this is not the case. For an increase in transmit output power, the ROSNR increases, due to the prevalence of non-linear effects of the components. In addition, the modulation induced optical loss (MIOL) is also plotted corresponding to the individual output power. The MIOL gives an indication of the total amount of optical power loss due to insertion losses in the MZM (splitters, combiners) and modulation scheme. By driving the components in non-linear regime, this loss reduces, ultimately increasing the output power.

Overall, we would like to achieve a power and cost efficient design of an optical transmit-
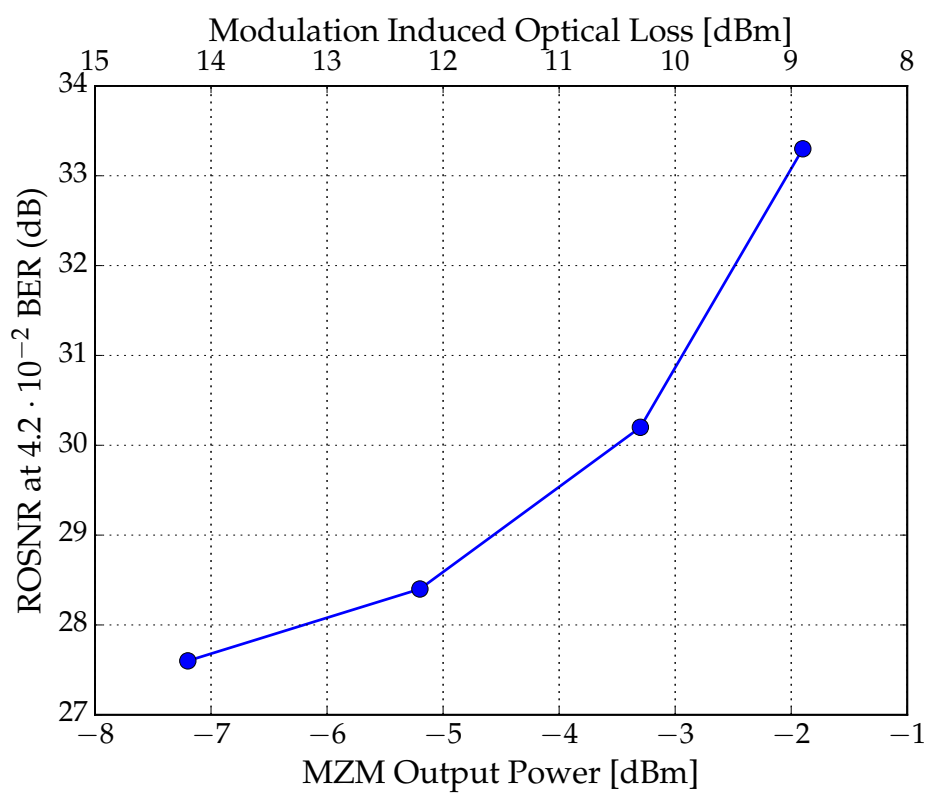
Figure 3.12: Effect of increasing MZM output power on ROSNR and modulation induced optical loss for DP-64QAM 40 GBaud signal

ter. This can be made possible by driving the components slightly in the non-linear regime. This must then be supported by a pre-distortion technique which reduces the deteriorating effects stemming from the non-linear effects.

3.6 Receiver Components

3.6.1 Optical Coherent Receiver

The optical coherent receiver is the innovative component of the receiver which facilitates the restoration of the amplitude, phase and polarization of the incoming optical signal in the electrical domain. Owing to its phase and polarization diversity nature [52], the optical signal's phase and polarization is linearly translated to the electrical domain [52].

Figure 3.13: Optical coherent receiver

The schematic diagram of a coherent front-end to detect a dual-polarization signal is shown in Figure 3.13. It consists of the following components :

1. Polarization beam splitter (PBS)

2. 2x4 90° hybrid

3. Photodiodes

The PBS splits the polarization of the incoming electric field, $\underline{E}_{rec}(t)$ into two orthogonal polarizations, $\underline{E}_X(t)$ and $\underline{E}_Y(t)$ and can be written as :

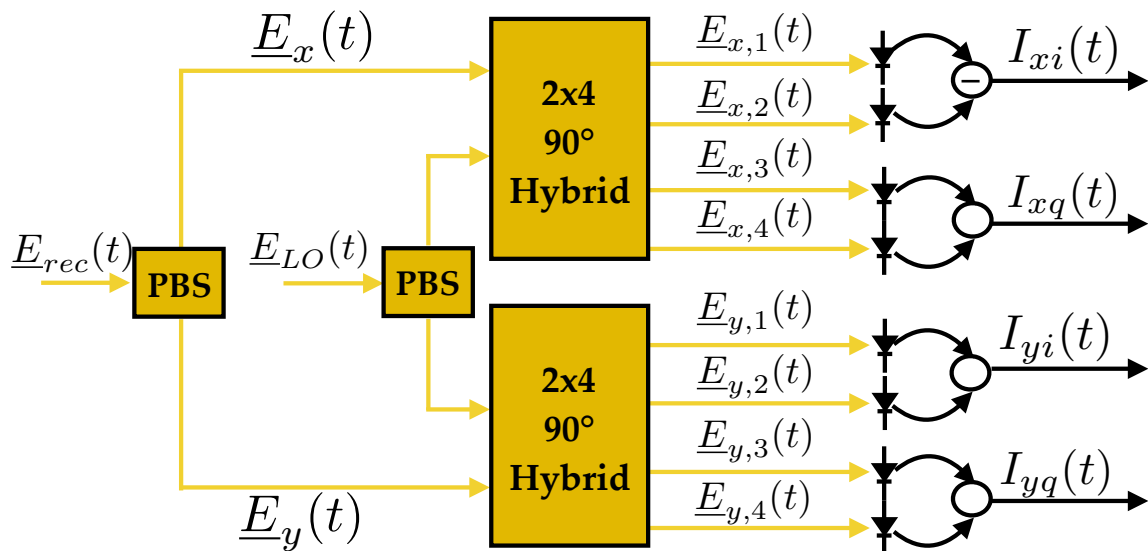$$\underline{E}_{rec}(t) = \begin{bmatrix} \underline{E}_x(t) \\ \underline{E}_y(t) \end{bmatrix} = \begin{bmatrix} \left|\underline{E}_{rec,x}(t)\right| \cdot e^{j\phi_x(t)} \cdot e^{j(\omega_c t + \phi_c(t))} \\ \left|\underline{E}_{rec,y}(t)\right| \cdot e^{j\phi_y(t)} \cdot e^{j(\omega_c t + \phi_c(t))} \end{bmatrix} \tag{3.33}$$

and the local oscillator (LO) is given as :

$$\underline{E}_{lo}(t) = \left|\underline{E}_{lo}(t)\right| \cdot e^{j(\omega_{lo}t + \phi_{lo}(t))} \tag{3.34}$$

where $\left|\underline{E}_{rec,x(t)}\right|$ and $\left|\underline{E}_{rec,y}(t)\right|$ are the modulated amplitudes of the electrical field in the X and Y polarization respectively. ϕ_x and ϕ_y contain the phase information. ω_c is the carrier frequency and $\phi_c(t)$ is the phase noise in the carrier. ω_{lo} is the LO frequency and $\phi_{lo}(t)$ is the phase noise in the LO.

The 2x4 90° component is able to do the simultaneous demodulation of the I and Q components of the electric field. The mixing of the received signal and the local oscillator signal takes place inside the 90° hybrid. This process is called demodulation. The received signal is split into two components, and the LO is split, and one of the outputs of the LO is further rotated by 90° to enable the quadrature demodulation.

Two of such hybrids are utilized individually for the X and Y polarizations of the received signal. The transmission matrix of an individual 2x4 90° hybrid is given as [3] :

$$\begin{bmatrix} \underline{E}_1(t) \\ \underline{E}_2(t) \\ \underline{E}_3(t) \\ \underline{E}_4(t) \end{bmatrix} = \frac{1}{2} \begin{bmatrix} 1 & 1 \\ 1 & -1 \\ 1 & j \\ 1 & -j \end{bmatrix} \cdot \begin{bmatrix} \underline{E}_{rec}(t) \\ \underline{E}_{lo}(t) \end{bmatrix}$$

where $\underline{E}_1(t)$, $\underline{E}_2(t)$, $\underline{E}_3(t)$ and $\underline{E}_4(t)$ are the 4 outputs. In case of the dual polarization receiver, there will be 8 outputs, 4 belonging to X and 4 to Y. For sake of brevity, the process of demodulation is analysed only for the X polarization. The four demodulated outputs, $\underline{E}_{x,1}(t)$, $\underline{E}_{x,2}(t)$, $\underline{E}_{x,3}(t)$ and $\underline{E}_{x,4}(t)$ are calculated as :

$$\underline{E}_{x,1}(t) = \frac{1}{2}[\underline{E}_{rec}(t) + \underline{E}_{lo}(t)] \tag{3.35}$$

$$\underline{E}_{x,2}(t) = \frac{1}{2}[\underline{E}_{rec}(t) - \underline{E}_{lo}(t)] \tag{3.36}$$

$$\underline{E}_{x,3}(t) = \frac{1}{2}[\underline{E}_{rec}(t) + j\underline{E}_{lo}(t)] \tag{3.37}$$

$$\underline{E}_{x,4}(t) = \frac{1}{2}[\underline{E}_{rec}(t) - j\underline{E}_{lo}(t)] \tag{3.38}$$

From [3, 52], the output of the photodiode is :

$$i(t) = R \cdot P(t) \tag{3.39}$$

$$P(t) = |\underline{E}(t)|^2 \tag{3.40}$$

where R is the responsivity of the photodiode [3].

Hence, the resulting four currents at the output of the photodiodes are :

$$i_{x,1}(t) = R \cdot \left|\underline{E}_{x,1}(t)\right|^2 = R \cdot \underline{E}_{x,1}(t) \cdot \underline{E}_{x,1}^*(t) \tag{3.41}$$

$$i_{x,2}(t) = R \cdot \left|\underline{E}_{x,1}(t)\right|^2 = R \cdot \underline{E}_{x,2}(t) \cdot \underline{E}_{x,2}^*(t) \tag{3.42}$$

$$i_{x,3}(t) = R \cdot \left|\underline{E}_{x,1}(t)\right|^2 = R \cdot \underline{E}_{x,3}(t) \cdot \underline{E}_{x,3}^*(t) \tag{3.43}$$

$$i_{x,4}(t) = R \cdot \left|\underline{E}_{x,1}(t)\right|^2 = R \cdot \underline{E}_{x,4}(t) \cdot \underline{E}_{x,4}^*(t) \tag{3.44}$$

which can be further expanded as :

$$i_{x,1}(t) = \frac{R}{4} \cdot [\underline{E}_{rec,x}(t) + \underline{E}_{lo,x}(t)] \cdot [\underline{E}_{rec,x}(t) + \underline{E}_{lo,x}(t)]^* \tag{3.45}$$

$$i_{x,2}(t) = \frac{R}{4} \cdot [\underline{E}_{rec,x}(t) - \underline{E}_{lo,x}(t)] \cdot [\underline{E}_{rec,x}(t) - \underline{E}_{lo,x}(t)]^* \tag{3.46}$$

$$i_{x,3}(t) = \frac{R}{4} \cdot [\underline{E}_{rec,x}(t) + j \cdot \underline{E}_{lo,x}(t)] \cdot [\underline{E}_{rec,x}(t) + j \cdot \underline{E}_{lo,x}(t)]^* \tag{3.47}$$

$$i_{x,4}(t) = \frac{R}{4} \cdot [\underline{E}_{rec,x}(t) - j \cdot \underline{E}_{lo,x}(t)] \cdot [\underline{E}_{rec,x}(t) - j \cdot \underline{E}_{lo,x}(t)]^* \tag{3.48}$$

$$I_{xi}(t) = i_{x,2}(t) - i_{x,1}(t) \tag{3.49}$$

$$= R \cdot \left|E_{lo,x}(t)\right| \cdot \left|E_{rec,x}(t)\right| \cdot \cos[(\omega_c - \omega_{lo})t + (\phi_c(t) - \phi_{lo}(t)) + \phi_x(t)] \tag{3.50}$$

and,

$$I_{xq}(t) = i_{x,4}(t) - i_{x,3}(t) \tag{3.51}$$

$$= R \cdot \left| E_{lo,x}(t) \right| \cdot \left| E_{rec,x}(t) \right| \cdot \sin[(\omega_c - \omega_{lo})t + (\phi_c(t) - \phi_{lo}(t)) + \phi_x(t)] \tag{3.52}$$

The currents in the Y polarization can be obtained likewise.

There are several terms to notice in Equation (3.50) and Equation (3.52) :

- The amplitude of the received wave can be read from $\left| E_{lo,x}(t) \right| \cdot \left| E_{rec,x}(t) \right|$. Moreover, a stronger signal is obtained for a higher LO power. This directly relates the receiver performance to the input LO's power and received signal's power.

- The phase of the received wave is determined from $\phi_x(t)$.

- $\omega_c - \omega_{lo}$ is the beating term. For perfect frequency synchronization of the transmit and LO laser, this term reduces to 0.

- $\phi_c(t) - \phi_{lo}(t)$ denotes the residual phase noise. The residual phase noise can deteriorate the information contained in the $\phi_x(t)$ of the received signal and hence it is critical to implement phase noise estimation and compensation algorithms in the receiver DSP [53].

Based on the frequency synchronization of the carrier and LO, the received signal can be demodulated in three ways [52] :

Homodyne Detection

Homodyne detection is the simplest form of demodulation where the transmitter and receiver LASERs have the same frequency and phase. This means that $\omega_c = \omega_{lo}$. Such a scheme eventually leads to a relaxation in the receiver DSP carrier recovery algorithms. But, at the same time is extremely difficult to implement in practice, since it demands the use of an optical phase locked loop (PLL) which makes the overall transponder design complex [52].

Heterodyne Detection

In heterodyne detection, two free-running LASERs, one at the transmitter and other at the receiver are used. The frequency difference, $\omega_c - \omega_{lo} \gg 1/T_s$ where T_s is the symbol rate of

the transmit signal. Such a scheme demodulates the signal to an intermediate frequency which needs to be further processed, either by an electrical PLL or by suitable receiver DSP algorithms.

Intradyne Detection

Intadyne detection is the most favorable of all the detection schemes. It requires two different LASERs, one for the transmitter and the other at the receiver, where $\omega_c - \omega_{lo} \approx 0$. The residual frequency and phase noise terms are then separately compensated in the receiver DSP [54]. Such a scheme relaxes the requirements on the additional PLLs required in the other detection schemes. In almost all experiments and commercial products, this is the scheme of choice.

In this thesis, intradyne detection was the most used detections scheme. In one experiment, homodyne detection was used. The use of the schemes will be mentioned individually in the respective experiments.

3.6.2 ADC

The analog to digital converter (ADC) is the key component in the receiver which makes various DSP operations possible. ADCs are electronic devices which enable the conversion of electrical signals from the coherent receiver into digital data which can then be further processed in the receiver DSP [5].

An ADC consists of two building blocks : a sample and hold (S/H) circuit and a quantizer. This is seen in Figure 3.14. The S/H circuit maintains a constant voltage to the quantizer during the time when the conversion is taking place. The output of the S/H circuit modifies at specific intervals, which is regulated by the ADC sampling rate. In the first step the continuous time variable is converted into time-discrete samples. The quantizer then converts the continuous amplitude values of the signals into specific digital values. These digital values are determined by the quantization bits of the ADC. For an *n-bit* ADC, there are 2^n levels, meaning that given an 8-bit ADC, the device can convert analog signal in range from -1 V to 1 V to a digital signal which lies between 0 and 256 or -128 to 127.

Figure 3.15 shows the input analog signal, the corresponding quantized signal and the quantization error with a 3-bit uniform ADC. The analog signal is between -1 V and 1 V. The signal is converted in the digital domain, where the signal can hold any digital value in the range of the 3-bit quantizer. The red curve shows the quantization error, which is also known as the quantization noise. Essentially, the input analog signal is the summation
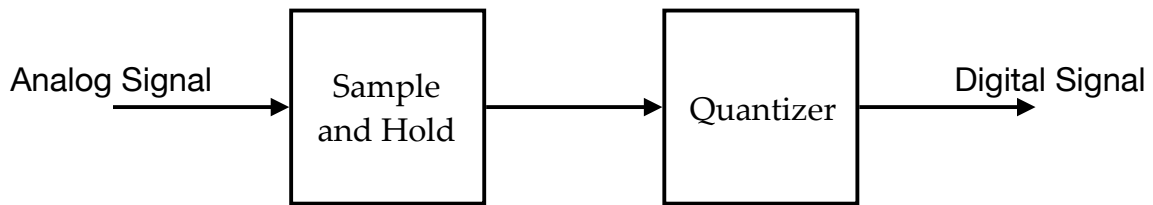
Figure 3.14: Sample and hold and Quantizer in an ADC
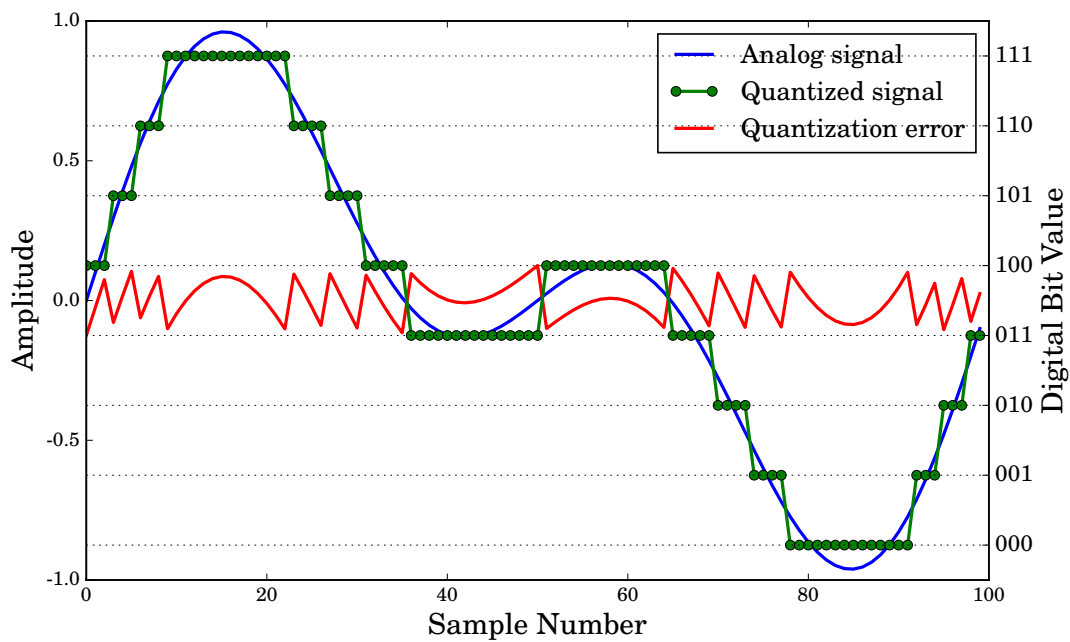
Figure 3.15: ADC analog input and digital output signals

of the quantized signal and the quantization error. In literature, this noise is shown to be an additive noise which is characterized by a uniform distribution with mean zero and standard deviation of $1/\sqrt{12} \cdot LSB$, where LSB is the value of the least significant bit [55,56]. Futhermore, the noise is uncorrelated with the input signal. Such a model is mostly adopted for modelling ADCs with higher resolution bits.

While the resolution of N bits determines the physical number of bits in the ADC, the ENOB is a figure of merit which is used to characterize the overall dynamic performance of the ADC after including other distortions [5]. ADCs are further characterized based on their analog bandwidth performance. As with the DACs, ADCs also suffer from a 3-dB analog bandwidth which further puts a limit on the transmission of higher data rate

signals.

As shown in the Walden plot in [5, Figure 12], the ENOB is inversely proportional to the frequency of the input signal. As the signal bandwidth increases, the ENOB value reduces. This decrease in ENOB ultimately causes deterioration in the transmission of higher modulation formats at higher bandwidths. For coherent systems, the fabrication of high resolution ADCs is a challenging task. The manufacturing of such ADCs is governed by the Walden plot [57], where as the sampling rate of the ADC increases, the ENOB decreases.

In order to overcome the limitation posed by the low ENOBs, authors in [58] presented a novel modelling technique to compensate for the quantization noise in low-resolution ADCs.

The ADC used in this thesis was operated at a sampling rate of 80 Gs/s with an analog bandwidth of 18 GHz.

3.7 Digital Signal Processing Algorithms

A detailed explanation of each of these blocks can be separately read in [59–61] and the references mentioned within. We will give an overview here. As a part of the thesis work, a brief description of the several block will be given in this section. The DSP algorithms can be divided into two main subparts namely, the transmitter DSP and the receiver DSP. Throughout this thesis a data-aided DSP was utilized, unless otherwise specified.
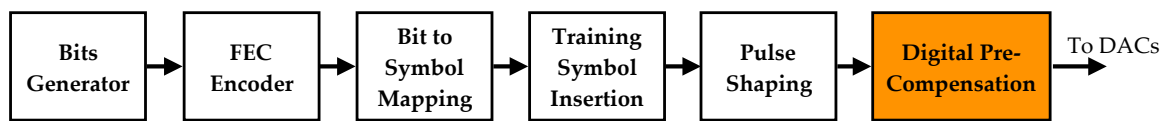
3.7.1 Transmitter DSP

Figure 3.16: Description of transmitter DSP blocks

We will take up the distinct blocks in the transmitter DSP chain and describe them in brief. The transmission starts from a bit source which is the bit generator. In real transmission these are typically the data bits which have to be communicated. For our purposes, random bits were generated using a pseudo random binary sequence (PRBS) generator. The bits are then encoded using a FEC encoder with several overhead percentage, details of which are out of the scope this thesis. The bits are arranged in frames with distinct lengths. Thereafter, the encoded bits are mapped to the chosen modulation format, which can be any of the m-QAM modulation formats (m being the modulation order such that $m = 2^n \ \ \forall n \in \{1, 2, 3, 4, 5, 6, 7\}$. Then, training symbols are inserted periodically at the start of each frame. These training symbols are later used in the receiver DSP to recover the frame start. The next step is the pulse shaping block. Pulse shaping has become very popular in the optical community. Typically RRC pulse shaping filters with several roll-offs are used in this block to produce pulses with specific bandwidth generating signals with better spectral efficiency and bandwidth requirements [62, 63]. Unless otherwise specified, the pulse shaping filter in the thesis was operated at a roll off of 0.2. For detailed description refer to [64] where an elaborate explanation is provided on the design of such filters. Following this comes the block of digital pre-compensation DPC which forms essential part of the thesis. An overview of th DPC block was provided in Chapter 2 and more elaborate discussion on this block is provided in the following chapters. The digitally pre-compensated signals are then uploaded to the DACs and after optical modulation sent over the fiber.

   After the transmission over the fiber, the optical signal accumulates several degrading linear distortions arising from the optical fiber, component imperfections, clock and carrier desynchronization. Some of these effects are deterministic while others are random. After obtaining the electrical baseband signal at the output of the coherent receiver, the electrical signals are converted to digital samples with the aid of an ADC. Next follows the processing of these digital samples in several blocks which are collectively called receiver DSP. The flow of the signal through the receiver DSP is depicted in Figure 3.17.

3.7.2 Receiver DSP

This section describes the standard DSP algorithms which are utilized to recover the received signals after transmission. Please note that the blocks explained in this section are later re-used in the discussion related to the development of receiver DSP required for performing digital pre-compensation. It is proposed to the readers to regard this as a standalone section which provides an overview of a typical receiver DSP and take it as reference for later chapters.
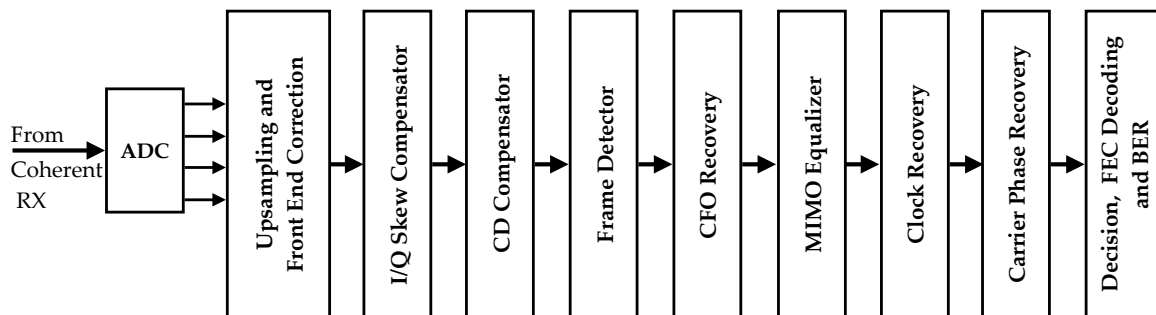
Figure 3.17: Description of receiver DSP blocks

Resampling and Front-End Correction

The first step in the receiver DSP is the resampling of the incoming samples to two times the symbol rate. This is ideally done by using a sinc interpolation filter. The upsampling/interpolation is performed for each ith tributary of the received signal.

Receiver I/Q Skew Compensation

The wires from the coherent receiver to the ADC are not perfectly matched. Due to this there may exist a receiver I/Q skew which needs to be compensated before performing

any other DSP operation. This is a simple operation which can be implemented either by a simple shift of samples in the time domain or by converting the samples in the frequency domain and compensating by a simple multiplication with the corresponding transfer function. Additional information on the working of the block is provided in Section 4.5.1 where receiver I/Q skew is compensated for a 4-D real signal.

Chromatic Dispersion (CD) Compensation

Chromatic dispersion (CD) is a linear impairment introduced by optical fibers. While for legacy IM/DD systems, CD is compensated in-line by using dispersion compensating fiber (DCF)s, such fibers are irrelevant for state of the art coherent systems. The task of the estimation and compensation of accumulated CD is executed in the receiver DSP. The effect of CD on an optical pulse, $\mathbf{E}(z, t)$ traveling in the fiber can be represented by the following transfer function, $H\left(L, f\right)$ [60, 61]:

$$H\left(L, f\right) = e^{-j\frac{\lambda_c^2 \pi}{c} D L f^2} \tag{3.53}$$

where D is the dispersion parameter, which in case of SSMF is typically 16.9ps/nm/km, L is the length of the fiber, λ_c is the reference wavelength and c is the speed of light.

The effect of CD is independent of the polarization and is just an all-pass filter which alters only the phase of the spectral components of the signal and leaves the magnitude undisturbed. Once the length of the link is fixed, CD value remains quite static and can be compensated by taking the conjugate of the transfer function shown in Equation (3.53). This compensation can either be employed in time-domain or in frequency domain. CD compensation can either be performed by simply calculating the accumulated CD value or letting it be estimated as done in [59]. In this thesis, a frequency domain based CD compensation block is used where the accumulated CD value is already estimated using the link length and dispersion parameter D.

Frame Detector

Since the signal is always transmitted in frames, the frame detector enables the identification of the start of the frame. In case of data-aided DSP, a copy of the training symbols is loaded on to the receiver side to enable frame detection. The start of the frame can then be estimated by performing a correlation between the received and sent signal.

CFO Recovery

Demodulation is the process of detecting the signal with a LO. The optical signal can be detected either in homodyne or intradyne configuration. In case of homodyne (which is possible only in the lab) the same transmitter LASER is split between transmitter and receiver. This leads to a perfect matching between the phase and frequency of the receiver LO and transmitter LASER. Therefore, in Equation (3.50) and Equation (3.52) :

$$\omega_c = \omega_{lo} \tag{3.54}$$

$$\phi_c(t) = \phi_{lo}(t) \tag{3.55}$$

Real systems are run with intradyne detection where a frequency offset in the order of 1 GHz can exist. Perfect hardware synchronization of the transmitter and receiver LASER is however not possible in real systems. This calls for a further frequency offset compensation in the DSP domain. The carrier frequency offset (CFO) estimation and compensation can be implemented in various ways. One of the ways is to use the 4th power of the received signal which removes the modulation and then use time-domain differential phase methods or frequency domain FFT methods to get an estimate of the coarse frequency offset [54, 60, 65]. Another way is to do a blind frequency search [65]. There are a class of algorithms based on training and feedback, which are independent of the modulation formats used [60]. In this thesis, the CFO recovery block was based on an in-house proprietary algorithm which in principle is data-aided and exploits the principles of time shift and correlation.

MIMO Equalization

In dual-polarization systems, as the two polarizations travel in the optical fiber, they will get affected by random time-varying polarization coupling and polarization mode dispersion [59–61, 63]. These effects are linear and are compensated by a 2×2 MIMO equalizer. The MIMO equalizer has a typical butterfly structure. Equalizers can be either blind or data-aided [61]. In case of a data-aided equalizer training symbols are utilized to estimate the equalizer taps by using a minimum mean square error criterion. In this thesis, a data-aided equalizer is used which is able to overcome the random polarization fluctuations and coupling. The coefficients of the equalizer are updated periodically in order to track the dynamic variations in the transmit signal.

Clock Recovery

At this stage the coarse frequency offset has been removed from the received samples. The received samples are, however, not synchronized with the frequency and the phase of the ADC clock. The task of the clock recovery block is to synchronize the received symbols. Various algorithms and structures exist in research and commercial products which are used for correcting the sampling frequency and phase offset error. Some solutions such as the Gardner's algorithm and Square Timing Recovery aim to estimate the timing information from the received samples [66, 67]. Another famous data-aided algorithm is the Mueller and Muller algorithm [68].

Typically, the digital clock recovery blocks include an interpolator [60]. Intermediate samples are then generated and inserted between the actually sampled digital samples. In this work, the square timing recovery is implemented to perform clock recovery.

Carrier Phase Recovery

Finally, the signals are processed to remove the excess phase noise resulting from the transmit and receiver LASERs. One of the most famous and used algorithms to remove the phase noise is the Viterbi and Viterbi algorithm [69] which was also employed in the receiver DSP in the thesis.

FEC Decoder and BER Calculation

Once the samples are free from all the distortions, they are ready to be decoded by the FEC decoder. FEC has become a powerful technique to aid the transmission of high data rate optical communication systems. FEC codes with various overheads such as, 7%, 15%, 25% and 35% have been published and some have also been deployed in commercial transponders. For this thesis a proprietary FEC algorithm was utilized wherever necessary.

4

Adaptive Digital Pre-Compensation

In the previous chapter, an overview of the transmitter and receiver components was provided. A comprehensive description of the various linear and non-linear effects of the transmitter components was presented as well. Digital pre-compensation (DPC) is a popular linearization technique to alleviate these effects. In Section 2.3, a summary of similar works related to DPC was provided. In this chapter, the adaptive DPC developed in the scope of the thesis will be discussed. We will discuss the building principles of the DPC block in the transmitter. Next, the memory polynomial model of the transmitter is introduced along with the indirect learning architecture (ILA) which form the core of the DPC block. Thereafter, the procedure to identify the DPC coefficients is explained. The operation of the DPC algorithm for various electrical and optical link scenarios is examined. In that respect, various system models are taken up and the application of the scheme is further developed and presented. This chapter specifically describes the *how-to* of the DPC algorithm and lays down steps to implement DPC in an optical transmitter.
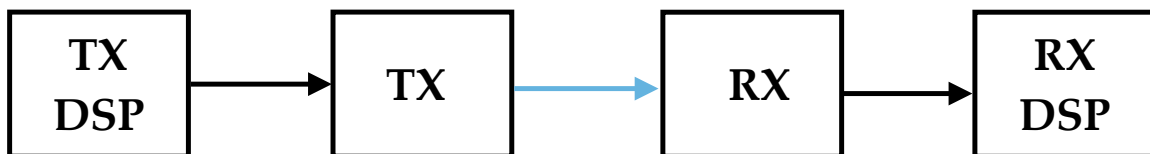

Figure 4.1: A standard transmitter receiver pair. The setup could be back-to-back or connected over a fiber.

Let us start by looking at Figure 4.1. This figure depicts a simple transmitter-receiver
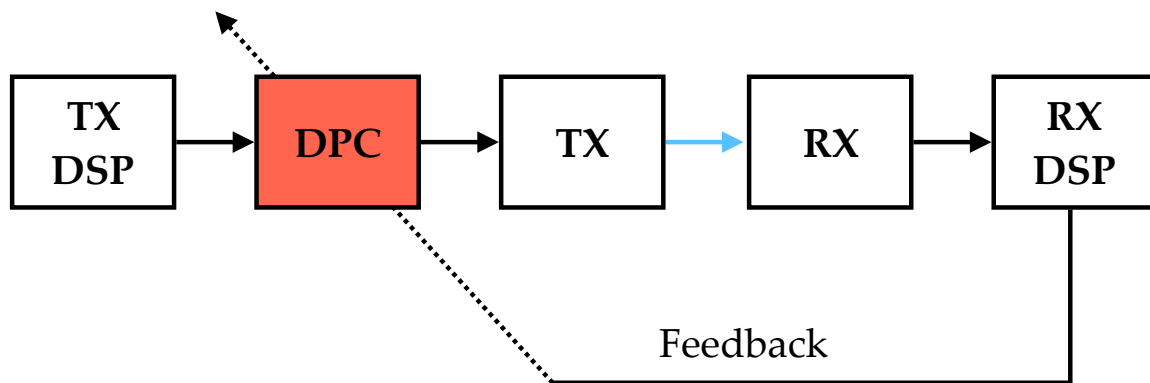
Figure 4.2: Proposed digital pre-compensation block architecture. The DPC block becomes an integral part of TX DSP. The coefficients within the DPC block can be updated

pair. Note that the two could be connected either directly which is called the *back-to-back* scenario or over the link, after transmission. Intuition tells us that in order to overcome the adverse effects of the transmitter components, a DPC block can be placed before the transmitter. Provided such a block is able to capture and invert the transmitter transfer function, the combination of the DPC block and the transmitter will produce a better quality signal. This is the main idea behind the implementation of this block which is depicted in Figure 4.2. Another notable feature of the proposed scheme is its ability to update the DPC block characteristics over time. This is shown by the feedback signal provided by the receiver to the DPC block. The *feedback* is an imperative part of the scheme. The feedback signal adds another advantage to the proposed scheme, in that it enables the tracking of the transmitter characteristics over time, hence being *adaptive*.

In a nutshell, the adaptive DPC scheme is built on the following foundations:

1. Memory polynomial model

2. Indirect learning architecture

3. Feedback from the receiver with suitable DSP operations

We will examine each of these principles in the following pages.

4.1 Memory Polynomial Model

A crucial aspect of any DPC scheme is the modeling of the system it is trying to compensate. For this work, we are interested in the modeling of the characteristics of the optical communication transmitter. The components in the optical transmitter which are the digital-to-analog converter (DAC), the electrical driver amplifier (DA) and the dual-polarization Mach-Zehnder Modulator (DP-MZM) can be unitedly modeled as time invariant non-linear system with memory. In literature it is established, that such systems can be modeled with Volterra series [70]. Variants of these models, like memory or memoryless systems are also used in modeling of wireless transmitter's components [20, 23, 70] which have their respective advantages and disadvantages. We will start by looking at the Volterra series and make our way to the memory polynomial model.

In discrete time domain, the Volterra series takes the following form:

$$y[n] = \sum_{p=1}^{P} \sum_{m_1=0}^{M} \sum_{m_2=0}^{M} \cdots \sum_{m_p=0}^{M} h_p[m_1, m_2, ..m_p] \cdot \prod_{j=1}^{P} x[n - m_j] \tag{4.1}$$

where $x[n]$ and $y[n]$ are input and output discrete samples of the system. P is the order, M is the memory accounted for in the system and $h_p[m_1, m_2, ...m_p]$ are the Volterra kernels. Depending on the order and memory chosen, these kernels are the pth order impulse responses of the system. It is evident that the sheer number of coefficients for Volterra series makes it difficult to implement in practice. Hence, other truncated variants of the series are adopted for practical applications [20]. In this work, an approximate memory polynomial model representation of the Volterra series is adopted, which was shown for the first time in [19] and used in [20].

The simplest non-linear model is when $M = 0$ for which Equation (4.1) becomes :

$$y[n] = \sum_{p=1}^{P} h_p[0]x^p[n] \tag{4.2}$$

This is called the *memoryless* model. Such a model, however, is too simple and will not account for any memory, and hence is not suitable to capture the memory effects such as the bandwidth limitation of the DAC, DA and DP-MZM.

If, however, we adopt a slightly complicated model and consider the Volterra kernels, for which

$$m_1 = m_2 = \cdots = m_p = m \tag{4.3}$$

we reduce the number of Volterra kernels drastically from $\sum_{p=0}^{P}(M + 1)^P$ to $(M + 1)P$. The resulting series can then be written as :

$$y[n] = \sum_{p=1}^{P} \sum_{m=0}^{M} h_{m,p}[m]x^p[n - m] \qquad (4.4)$$

Following non-causal representation for the memory polynomial in Equation (4.4) is chosen in this thesis:

$$y[n] = \sum_{p=1}^{P} \sum_{m=-(M-1)/2}^{(M-1)/2} h_{m,p}x^p[n - m] \qquad (4.5)$$

Equation (4.5) is utilized to model the non-linearities of order P and memory M in the transmitter. $h_{m,p}$ are the respective coefficients.

For $P = 1$, Equation (4.5) becomes:

$$y[n] = \sum_{m=-(M-1)/2}^{(M-1)/2} h_m x[n - m] \qquad (4.6)$$

which is a linear time-invariant finite impulse response (FIR) filter. This linear model is used for modeling transmitter linear effects which are the 3-dB bandwidth effect of the transmitter and the transmitter I/Q skew.

As seen in this section, memory polynomials are a good compromise between the full blown Volterra series and the memoryless system shown in Equation (4.2) in terms of computational and implementation complexity. Therefore, the memory polynomial model is chosen as the basis of modeling the transmitter components and for implementing the inverse of the transmitter transfer characteristics in the DPC block. This section then concludes the discussion on memory polynomial model which is the first principle DPC is based upon.

4.2 Indirect Learning Architecture

The second principle of the DPC algorithm is the Indirect learning architecture (ILA). ILA is a measurement procedure which was first introduced by Eun and Powers [18]. It is a suitable method to identify the inverse of any system, namely linear and non-linear systems with or without memory. The ILA technique is useful to calculate the inverse of the system without calculating the transfer function of the channel or system under consideration,
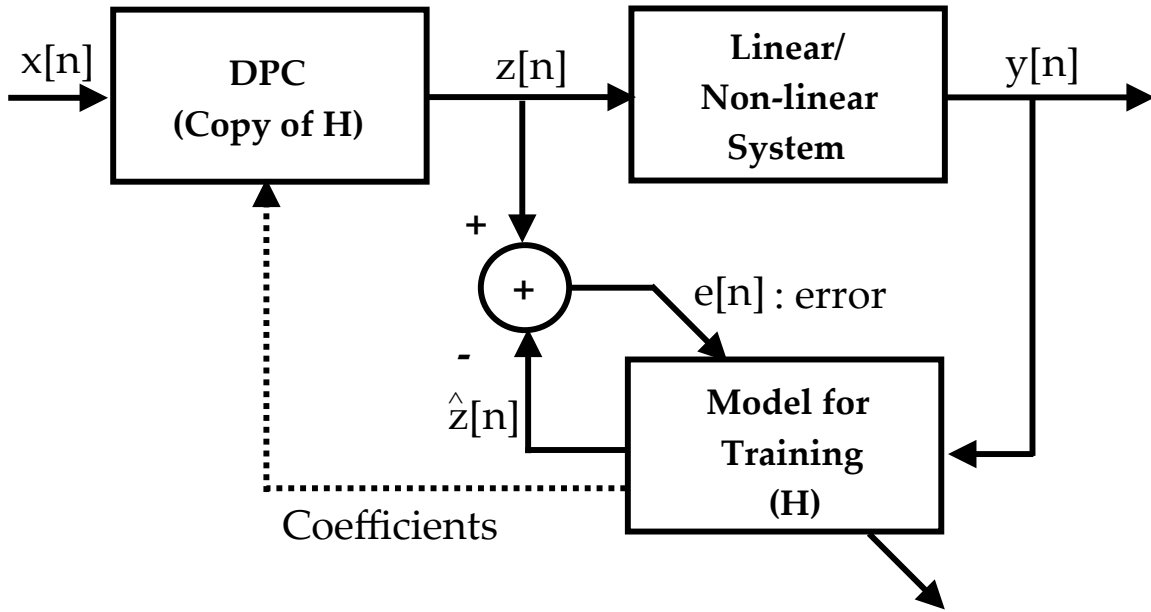
Figure 4.3: Indirect learning architecture [18]

hence the name ILA.

In this thesis work, the method is used for identifying the filter coefficients of the DPC block. The block diagram of ILA is drawn in Figure 4.3. Note that there are two identical blocks, H, one in the feedback path for training the memory polynomial model and the other block which is a replica of the training block in the forward path of DPC.

The forward path to the DPC block has digital samples, $x[n]$ at its input and $z[n]$ at its output. The output of the system is $y[n]$ which is also the input to the *training block*. The output of the *training block* is $\hat{z}[n]$. Ideally, we want $y[n] = x[n]$. A suitable model, which in our case is the memory polynomial model, is adopted for H in the *training block*. Given $z[n]$ and $y[n]$, the task is then to first find H. This phase is called training and the DPC block is set to identity such that the samples are just multiplied by 1 in this block. The training mode aims at minimizing the power of the error signal $e[n]$ by a least-squares algorithm. As $e[n]$ reaches zero, the training model synthesizes the inverse of the transmitter. At this point, $z[n]$ becomes equal to $\hat{z}[n]$ and $x[n]$ becomes almost identical to $y[n]$.

After the training mode, the parameters of *training block* are copied into the DPC block. The cascade of the DPC block with the system then becomes the identity operator. The signal $z[n]$ is called the digitally pre-compensated signal. It should be noted that the training mode can be run during factory calibration or, if the transmitter characteristics drift

over time, taking into account component ageing, the procedure could be run periodically, even during operation.

In the next subsection, we will discuss the identification of the parameters of the training block. Henceforth, the parameters are addressed as the coefficients of the DPC block.

4.2.1 DPC Coefficient Identification

The identification of the DPC block coefficients is realized by utilizing the ILA and the *least-squares* algorithm [71].

The identification of the model H is carried out by estimating the coefficients of the model denoted as $\mathbf{h}$. This can be achieved by following the given steps:

- **Step 1**

  Collect a block of successive N samples of a digital input signal $\mathbf{x}$ and digital output signal, $\mathbf{y}$, where:

$$\mathbf{x} = \Big[x[0], x[1], \cdots x[N-1] \Big]^T_{N \times 1} \tag{4.7}$$

$$\mathbf{y} = \Big[y[0], y[1], \cdots y[N-1] \Big]^T_{N \times 1} \tag{4.8}$$

  Normalize signals $\mathbf{x}$ and $\mathbf{y}$ such that :

$$\mathbf{x} = \frac{\mathbf{x}}{max(\mathbf{x})} \tag{4.9}$$

$$\mathbf{y} = \mathbf{y} \cdot \sqrt{\frac{\sum_{i=0}^{N-1} x_i^2}{\sum_{i=0}^{N-1} y_i^2}} \tag{4.10}$$

- **Step 2**

  Choose a suitable model for the system to be equalized. As explained in Section 4.1, we select the memory polynomial model with initial number of memory taps, M and order P. In order to characterize the inverse of the system, the respective signals are chosen and Equation (4.5) takes the form :

$$\hat{z}[n] = \sum_{p=1}^{P} \sum_{m=0}^{M} h_{m,p} y^p[n-m] \tag{4.11}$$

$$\hat{\mathbf{z}} = \left[\hat{z}[0], \hat{z}[1], \cdots \hat{z}[N-1] \right]^T_{N \times 1} \tag{4.12}$$

$\hat{z}[n]$ is the output at the DPC training block. Note that Equation (4.11) models the inverse of the system in contrast Equation (4.5) which models the system itself.

Let us collect the individual coefficients, $h_{m,p}$ in a vector $\mathbf{h}$:

$$\mathbf{h} = \left[h_{0,1}, \cdots h_{M,1}, h_{0,2}, \cdots h_{M,2}, \cdots h_{M,P} \right]^T_{(M+1)P \times 1} \tag{4.13}$$

and define a matrix $\mathbf{B}$, which will be called the base function matrix and is constructed by collecting several time shifted copies of signal $\mathbf{y}$ as :

$$\mathbf{B} = \left[\mathbf{y}_{0,1}, \cdots \mathbf{y}_{M,1}, \mathbf{y}_{0,2}, \cdots \mathbf{y}_{M,2}, \cdots \mathbf{y}_{M,P} \right]^T_{N \times (M+1)P} \tag{4.14}$$

where each column of the matrix is a vector $\mathbf{y}$ with a corresponding delay m and order p defined as:

$$\mathbf{y}_{m,p} = \left[y_{m,p}[0], y_{m,p}[1], \cdots, y_{m,p}[N-1] \right]^T_{N \times 1} \tag{4.15}$$

and

$$y_{m,p}[n] = y^p[n-m] \tag{4.16}$$

We can re-write Equation (4.11) in matrix form as:

$$\hat{\mathbf{z}} = \mathbf{B} \cdot \mathbf{h} \tag{4.17}$$

- **Step 3**

  The next step is to find the coefficients, $\mathbf{h}$ such that the error, $\mathbf{e}$ is minimized. This problem can be formulated as :

$$\mathbf{e} = \min_{\hat{h}} \left\| \mathbf{z} - \mathbf{B} \cdot \hat{h} \right\| \tag{4.18}$$

with the error vector,

$$\mathbf{e} = \Big[e[0], e[1], \cdots e[N-1] \Big]^T \tag{4.19}$$

Given $\mathbf{y}$, constructing matrix $\mathbf{B}$ is straightforward. In step 1, the DPC block is set to identity, hence $\mathbf{z}$ is set to $\mathbf{x}$. Following this substitution, Equation (4.18) becomes :

$$\mathbf{e} = \min_{\hat{h}} \left\| \mathbf{x} - \mathbf{B} \cdot \hat{h} \right\| \tag{4.20}$$

which is a linear system of equations with more equations than unknowns, popularly known as an over-determined system in literature [71]. Such a system of equations often has no solution. However, an estimate of the coefficients, $\hat{\mathbf{h}}$ can be obtained by making the error as small as possible and reaching the *least−squares−solution* [20,71]. This is accomplished by solving the following *normal equation*,

$$\hat{\mathbf{h}} = (\mathbf{B}^T \cdot \mathbf{B})^{-1} \cdot \mathbf{B}^T \cdot \mathbf{x} \tag{4.21}$$

The least squares solution to Equation (4.21) only exists when $(\mathbf{B}^T \cdot \mathbf{B})^{-1}$ exists. This can be guaranteed by eliminating all the dependent columns in $\mathbf{B}$ beforehand and is often not an issue in practical applications.

- **Step 4**

  After obtaining the inverse coefficients, $\mathbf{h}$ and plugging into the DPC block, it is seen that,

$$\mathbf{x} \approx \mathbf{y} \tag{4.22}$$

$$\mathbf{z} \approx \hat{\mathbf{z}} \tag{4.23}$$

$$\mathbf{e} \approx 0 \tag{4.24}$$

  The estimated coefficients, $\mathbf{h}$ from the training model are then copied to the DPC block. Input samples, $\mathbf{x}$ are then convoluted with $\mathbf{h}$ to produce DPC signal $\mathbf{z}$ which can then be further transmitted.
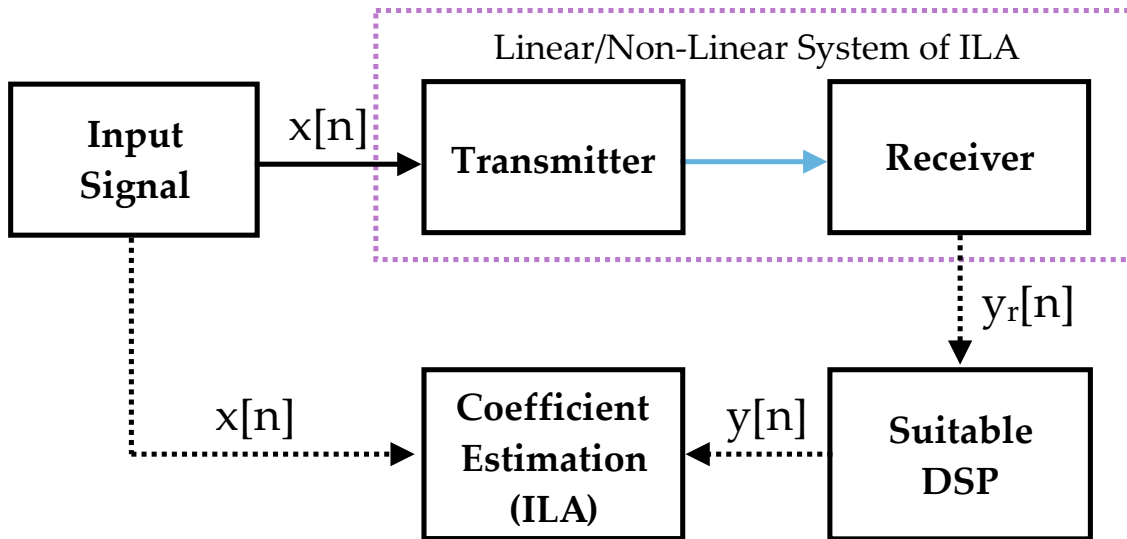
Figure 4.4: Training mode of the implementation. In the training mode, the system is connected in back-to-back.

4.3 DPC Implementation with Feedback from Receiver

Up until now we have discussed the memory polynomial model, the ILA and the procedure of least squares solution to find the DPC coefficients with it. The third principle upon which the DPC algorithm is established is getting *feedback from receiver*. In this section, we will take up the principle of ILA and combine it with feedback from receiver to achieve a working implementation of DPC in a system with transmitter and receiver blocks.

The working of DPC can be divided into two modes, namely:

1. Training Mode

2. Working Mode

Figure 4.4 shows the setup when the system is in training mode. In this phase, the system is connected in a *back-to-back* scenario to acquire feedback signal from the receiver. The diagram is similar to Figure 4.3 but with special addition of the transmitter and receiver blocks which make up the linear/non-linear system. The transmitter is the block we are interested in compensating for. Digital signals are denoted with black lines and the analog signal (electrical or optical) between receiver and transmitter is denoted with a blue color. After receiving samples from the receiver, digital samples, $y_r[n]$ are processed with suitable
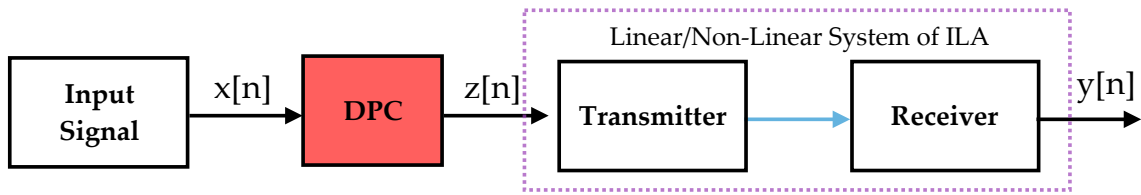
Figure 4.5: Working mode of the implementation.

DSP. These samples are forwarded to the coefficient estimation block. Once the coefficients are estimated, the training mode is concluded and DPC enters the *working-phase*.

In the *working phase*, the DPC coefficients obtained from the training mode are copied into the DPC block from Figure 4.3 and the system is left to work. In the normal working of the transponder, any input signal passing through the DPC block will get processed and then transmitted. Figure 4.5 depicts this phase.

Of course the two phases can be alternated as per requirements. The combined system architecture for DPC's training and working mode is depicted in Figure 4.6. The lower dotted branch is switched on when the DPC coefficients have to be calculated and copied into the DPC block. Afterwards, the training branch is switched off and normal transmitter operation is carried out with the DPC coefficients.

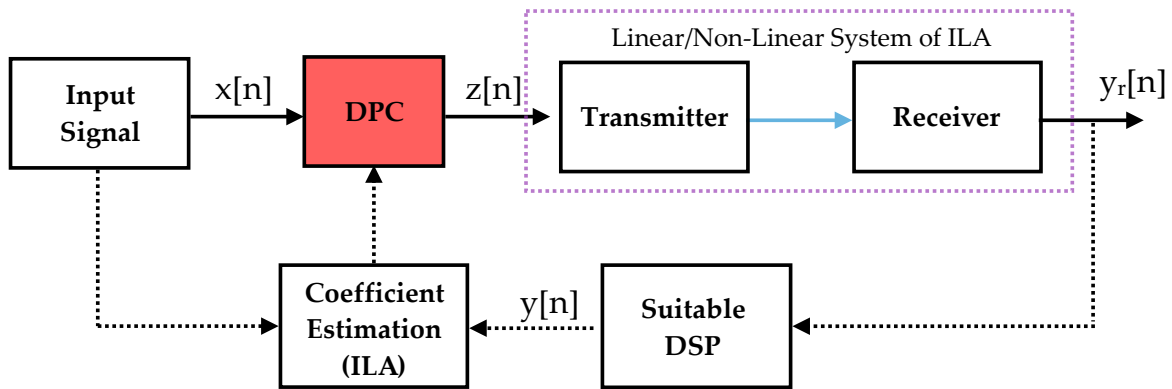Figure 4.6: Combined training and working mode of the implementation.

We have discussed the two phases of DPC implementation. In addition to this, we saw that a feedback signal from the receiver is a fundamental requirement. This feedback signal can take various forms, like electrical or optical. In this work, DPC was developed and implemented for the following feedback scenarios:

1. Electrical back-to-back

2. Optical back-to-back with homodyne and intradyne detection

3. Optical feedback from far-end receiver

In the next section, we will go through each of these feedback scenarios and examine the application of the DPC scheme along with the block *suitable DSP* for the respective cases.

4.4 System Model : Electrical Back-to-Back

The design of a dual polarization coherent optical communication system was described in Chapter 3. Figure 4.7 shows the block diagram of the transponder when the DAC is directly connected to the ADC. This is known as electrical back-to-back configuration. It consists of a transmitter DSP block which is generating transmit samples of various modulation formats. The digital samples are then uploaded to the DAC which converts the digital samples to analog signals. The analog signals are then received with a high sampling rate ADC which converts the electrical signals to digital domain. The received digital samples can then be suitably processed in the receiver DSP.
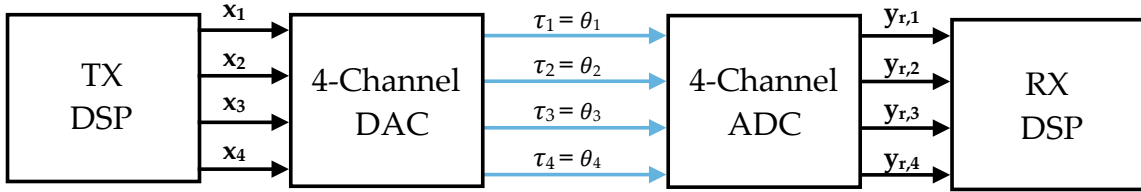

Figure 4.7: Block diagram of electrical back-to-back setup

A baseband equivalent model of Figure 4.7 is shown in Figure 4.8. A dual polarization system consists of four input tributaries. Let us consider a 4-D input vector, $\mathbf{X} \in \mathbb{R}^{4 \times N}$ to represent these 4 signals. This is represented in matrix form as :

$$\mathbf{X} = \begin{bmatrix} \mathbf{x_1} \\ \mathbf{x_2} \\ \mathbf{x_3} \\ \mathbf{x_4} \end{bmatrix} = \begin{bmatrix} x_1[0] & x_1[T_s] & x_1[2T_s] & \cdots & x_1[(N-1)T_s] \\ x_2[0] & x_2[T_s] & x_2[2T_s] & \cdots & x_2[(N-1)T_s] \\ x_3[0] & x_3[T_s] & x_3[2T_s] & \cdots & x_3[(N-1)T_s] \\ x_4[0] & x_4[T_s] & x_4[2T_s] & \cdots & x_4[(N-1)T_s] \end{bmatrix}_{4 \times N} \tag{4.25}$$

and T_s is the symbol interval.

The vector of the impulse response of the four individual DACs and the subsequent connecting wires is denoted by $\mathbf{p} \in \mathbb{R}^{4 \times L_{dac}}$, where L_{dac} is the discrete filter length after
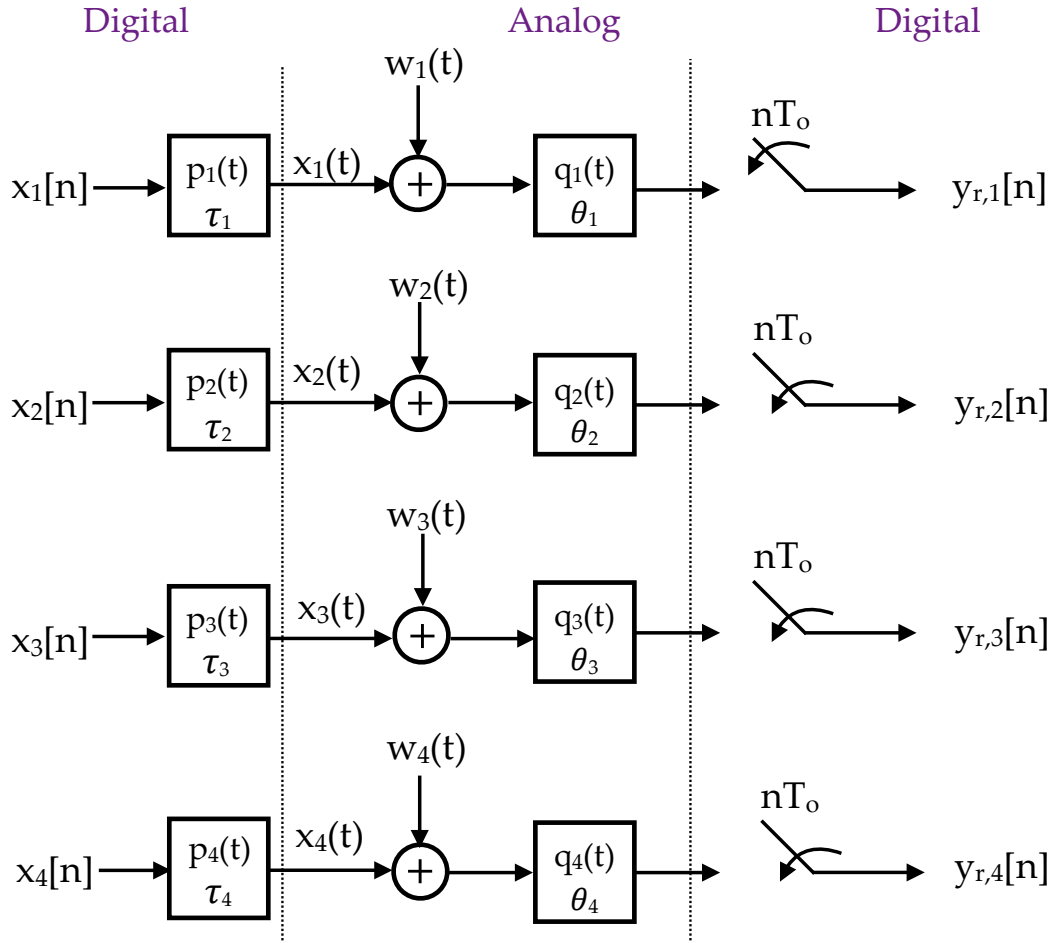
Figure 4.8: Baseband equivalent model of electrical back-to-back setup

sampling. The linear effects i.e. the bandwidth limitation and the I/Q skew for each ith ($i = 1, 2, 3, 4$) tributary are modeled with a filter with impulse response $p_i(t)$:

$$\mathbf{p} = \begin{bmatrix} p_1(t) \\ p_2(t) \\ p_3(t) \\ p_4(t) \end{bmatrix}_{4 \times L_{dac}} \tag{4.26}$$

The transmitter I/Q skew of the four tributaries can be explicitly expressed by the vector $\boldsymbol{\tau} \in \mathbb{R}^{4 \times 1}$ with impulse response:

$$\tau = \begin{bmatrix} \delta(t - \tau_1) \\ \delta(t - \tau_2) \\ \delta(t - \tau_3) \\ \delta(t - \tau_4) \end{bmatrix} \tag{4.27}$$

The linear impulse response of the ADC for the four tributaries is collected in $\mathbf{q} \in \mathbb{R}^{4 \times L_{adc}}$, and can be written analogous to Equation (4.26) with L_{adc} as the discrete filter length after sampling. The receiver skew is represented by the vector, $\boldsymbol{\theta}$, with the impulse response,

$$\theta = \begin{bmatrix} \delta(t - \theta_1) \\ \delta(t - \theta_2) \\ \delta(t - \theta_3) \\ \delta(t - \theta_4) \end{bmatrix} \tag{4.28}$$

The vector of impulse response of additive white gaussian noise (AWGN), $\mathbf{w}$ is added to each tributary independently.

In the case of electrical back-to-back, the transmitter and receiver I/Q skew are the same for each ith tributary (as also demonstrated in Figure 5.2). Therefore,

$$\tau_i = \theta_i \tag{4.29}$$

The combined channel response of the system is written as the convolution of the impulse responses, $p_i(t)$ and $q_i(t)$:

$$s_i(t) = p_i(t) * q_i(t) \tag{4.30}$$

where $p_i(t)$ is the impulse response of the ith DAC and wire and $q_i(t)$ is the impulse response of the ith ADC. $*$ is the convolution operator.

The received samples, $y_{r,i}[n]$ are then obtained as a convolution of $x(t)$ and $s(t)$ and given as:

$$y_{r,i}[n] = y_{r,i}[nT_o] = \sum_{m=-\infty}^{\infty} x_i[mT_s] \cdot s_i(nT_o - mT_s - \tau_i) + w_i(nT_o) \tag{4.31}$$

where T_o is the sampling period and T_s is the symbol period.

In addition to the standard convolution operation, a 4-D delay operator, $\mathbb{D}$, is introduced which is utilized for modeling of the delays incurred by the signals during transmission.

This operator works in the following way:

$$\mathbb{D}(\mathbf{X}, \boldsymbol{\tau}) = \begin{bmatrix} x_1[-\tau_1] & x_1[T_s - \tau_1] & x_1[2T_s - \tau_1] & \cdots & x_1[(N-1)T_s - \tau_1] \\ x_2[-\tau_2] & x_2[T_s - \tau_2] & x_2[2T_s - \tau_2] & \cdots & x_2[(N-1)T_s - \tau_2] \\ x_3[-\tau_3] & x_3[T_s - \tau_3] & x_3[2T_s - \tau_3] & \cdots & x_3[(N-1)T_s - \tau_3] \\ x_4[-\tau_4] & x_4[T_s - \tau_4] & x_4[2T_s - \tau_4] & \cdots & x_4[(N-1)T_s - \tau_4] \end{bmatrix}_{4 \times N} \quad (4.32)$$

During transmission from the DAC to the ADC, input signals, $\mathbf{X}$ experience a delay arising due to transmitter I/Q skew. Accompanying the individual I/Q skews, there is a coarse delay, $\boldsymbol{\tau_g} \in \mathbb{Z}^{4 \times 1}$ arising due to the processing in the DACs and ADCs. This delay is a deterministic delay and can be factored out. Hence, in terms of the delay operator, the output signal matrix, $\mathbf{Y_r}$ can be written as :

$$\mathbf{Y_r} = \mathbb{D}\left(\mathbf{X}, \boldsymbol{\tau_g} + \boldsymbol{\tau}\right) \quad (4.33)$$

Assuming that we know the $\boldsymbol{\tau_g}$, the task is then to estimate the inverse of $\mathbf{s}$ using the DPC training mode. Let us denote the inverse of $\mathbf{s}$ as $\mathbf{h}$. The estimation of $\mathbf{h}$ will lead to the inverse transfer function of the system, from which the frequency response and transmitter I/Q skew can be further obtained. In the following subsection, we will look into the *suitable DSP* block for the electrical back-to-back scenario which is necessary to enable the function of the DPC training mode.

4.4.1 Suitable DSP for Electrical Back-to-Back

Figure 4.9 shows the DSP blocks required for electrical back-to-back setup. Our task is to obtain the 4-D vector $\mathbf{Y}$, given $\mathbf{Y_r}$.

Upsampling and interpolation

Depending upon the sampling rates of the DACs and ADCs, appropriate resampling is performed. For the case in this thesis, $T_{dac} < T_{adc}$. Therefore the received samples, $\mathbf{Y_r}$ at T_{adc} should be first upsampled to the DAC sampling rate, T_{dac}. This is ideally done by using a sinc interpolation filter. The upsampling/interpolation is performed for each ith tributary of the received signal 4-D vector, $\mathbf{Y_r}$. The output after the upsampling is $\mathbf{Y_u}$.
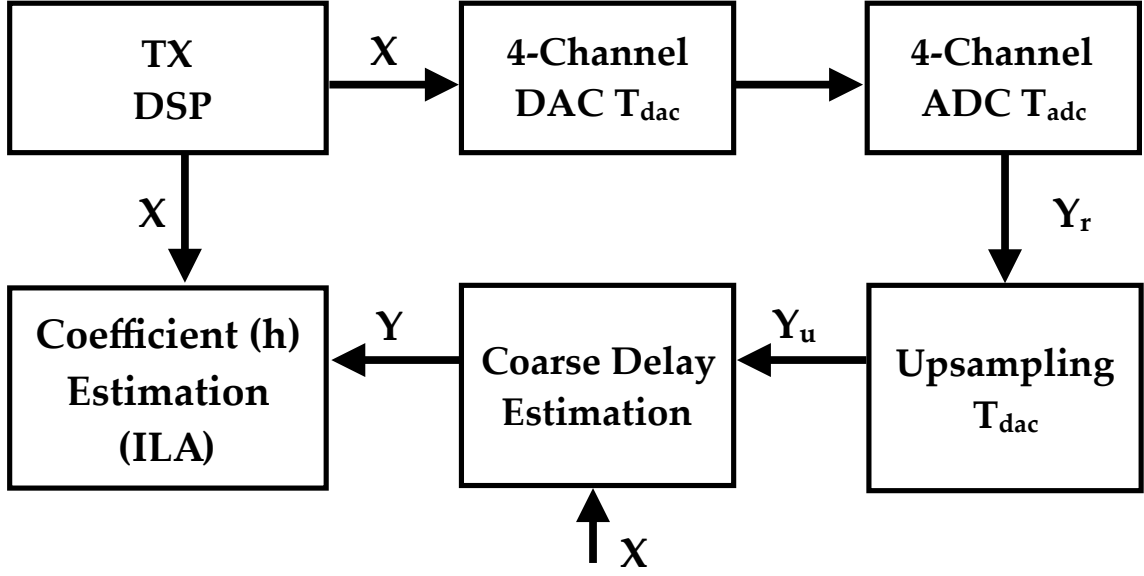
Figure 4.9: DPC architecture for electrical back-to-back

Coarse Delay Estimation and Compensation

After resampling, an estimate of the coarse processing delay $\boldsymbol{\tau_g}$ between the input signal $\mathbf{X}$ and upsampled signal $\mathbf{Y_u}$ is obtained by doing a cross-correlation which becomes a simple multiplication in the frequency domain. The delay for the ith tributary is then given as:

$$C_i[n] = \mathcal{F}(x_i[n]) \cdot (\mathcal{F}(y_{u,i}[n]))^* \tag{4.34}$$

$$\tau_{g,i} = \operatorname{argmax} \mathcal{F}^{-1}(C_i[n]) \tag{4.35}$$

where $\mathcal{F}$ is the Fourier transform operator for the digital signals. The coarse processing delay is then removed from the signals $\mathbf{Y_u}$ by employing the delay operator,

$$\mathbf{Y} = \mathbb{D}\left(\mathbf{Y_u}, -\tau_g\right) \tag{4.36}$$

Signals $\mathbf{X}$ and $\mathbf{Y}$ are then the relevant input signals for the *coefficient estimation* block. $\mathbf{h}$ can then be calculated by following the steps mentioned in Section 4.2.1. Note that the estimation gives an inverse of the whole electrical transmitter and electrical receiver chain in this case.

4.4.2 Calculation of transmitter I/Q skew

The transmitter I/Q skew can be calculated from the estimated DPC coefficients, $\mathbf{h}$ as follows:

A phase response, $\phi_i(\omega)$ for each FIR-filter $h_i(t)$ is obtained. The corresponding group delay, $\hat{\tau}_i$ is obtained as:

$$\hat{\tau}_i = -\frac{d\phi_i(\omega)}{d\omega}\bigg|_{\omega=0}, \tag{4.37}$$

where $i = [1, 2, 3, 4]$. Then, we obtain the estimated TX I/Q skew for the X and Y polarization axes as

$$\tau_{XQ-XI} = \hat{\tau}_2 - \hat{\tau}_1 \tag{4.38}$$

and

$$\tau_{YQ-YI} = \hat{\tau}_4 - \hat{\tau}_3 \tag{4.39}$$

In following sections, τ_{XQ-XI} and τ_{YQ-YI} terminology will be used to address the transmitter I/Q skew values.

4.5 System Model : Optical Back-to-Back

The next scenario which was taken up is the optical back-to-back case. The optical back-to-back setup for the transponder is shown in Figure 4.10. In addition to the blocks of transmitter DSP and DAC, there are additional blocks of the electrical driver amplifier DA and dual polarization Mach-Zehnder Modulator DP-MZM which makes the overall system more complicated. The signal from the DP-MZM is fed directly into the coherent receiver for demodulation with a LO. Demodulated signals are forwarded to the ADC, where they are sampled at T_o and then sent to the receiver DSP block.

An equivalent baseband model of the optical back-to-back scenario for a dual-polarized coherent system is drawn in Figure 4.11. The definitions of $\mathbf{X}$, $\mathbf{p}$, $\mathbf{q}$, $\boldsymbol{\tau}$, $\boldsymbol{\theta}$ and $\mathbf{w}$ remain the same as explained in Section 4.4.

The DP-MZM and the short optical fiber used in this scenario are modeled by the transfer matrix, $\mathbf{C} \in \mathbb{R}^{4 \times 4}$ [35]. A multiple input multiple output (MIMO) structure is chosen here to represent the various effects contained in the matrix, $\mathbf{C}$. This matrix is a linear model of the various effects which are the linear amplification of the DA and the polarization rotation introduced by the DP-MZM and the short optical fiber connecting the transmitter
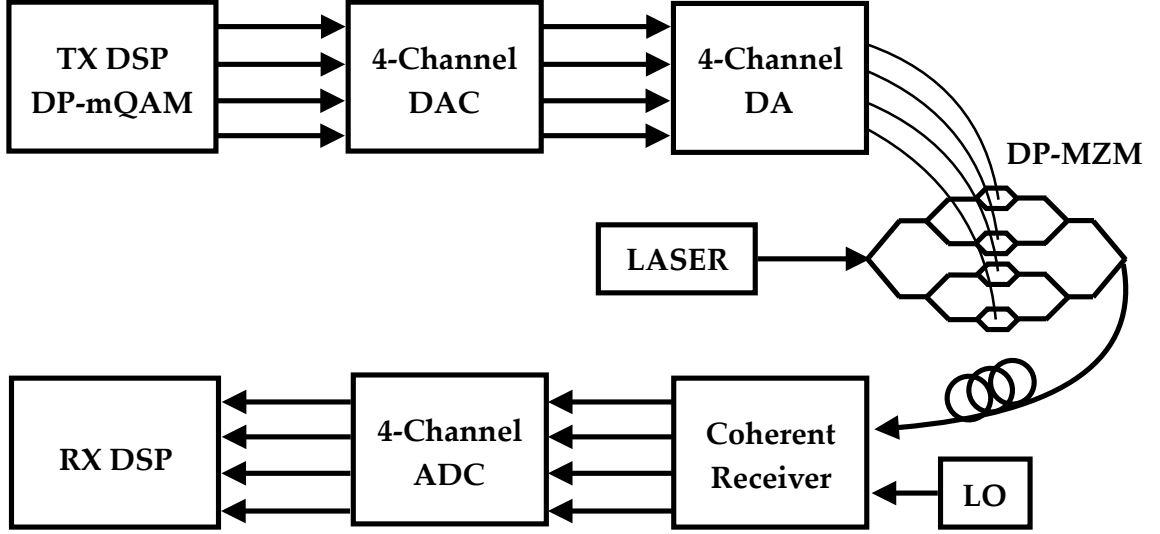
Figure 4.10: Block diagram of optical back-to-back setup

to the receiver. The DP-MZM is assumed to be working in the linear region of its operation. This matrix $\mathbf{C}$ is made up of two parts: an amplification matrix, $\mathbf{A} \in \mathbb{R}^{4 \times 4}$ and a unitary rotation matrix, $\mathbf{R} \in \mathbb{R}^{4 \times 4}$ and is given as :

$$
\mathbf{C} =
\begin{bmatrix}
c_{11} & c_{12} & c_{13} & c_{14} \\
c_{21} & c_{22} & c_{23} & c_{24} \\
c_{31} & c_{32} & c_{33} & c_{34} \\
c_{41} & c_{42} & c_{43} & c_{44}
\end{bmatrix}_{4 \times 4}
\tag{4.40}
$$

$$
\mathbf{C} = \mathbf{A} \cdot \mathbf{R} =
\begin{bmatrix}
a_{11} & 0 & 0 & 0 \\
0 & a_{22} & 0 & 0 \\
0 & 0 & a_{33} & 0 \\
0 & 0 & 0 & a_{44}
\end{bmatrix}_{4 \times 4}
\cdot
\begin{bmatrix}
r_{11} & r_{12} & r_{13} & r_{14} \\
r_{21} & r_{22} & r_{23} & r_{24} \\
r_{31} & r_{32} & r_{33} & r_{34} \\
r_{41} & r_{42} & r_{43} & r_{44}
\end{bmatrix}_{4 \times 4}
\tag{4.41}
$$

After the addition of an individual AWGN vector, $\mathbf{w}$ to the output at $\mathbf{C}$, demodulation is performed. A CFO Δf is introduced by the LO during demodulation. Additionally, the phase noise due to the laser linewidth of the transmitter and receiver LASERs is contained in $\varphi(t)$.
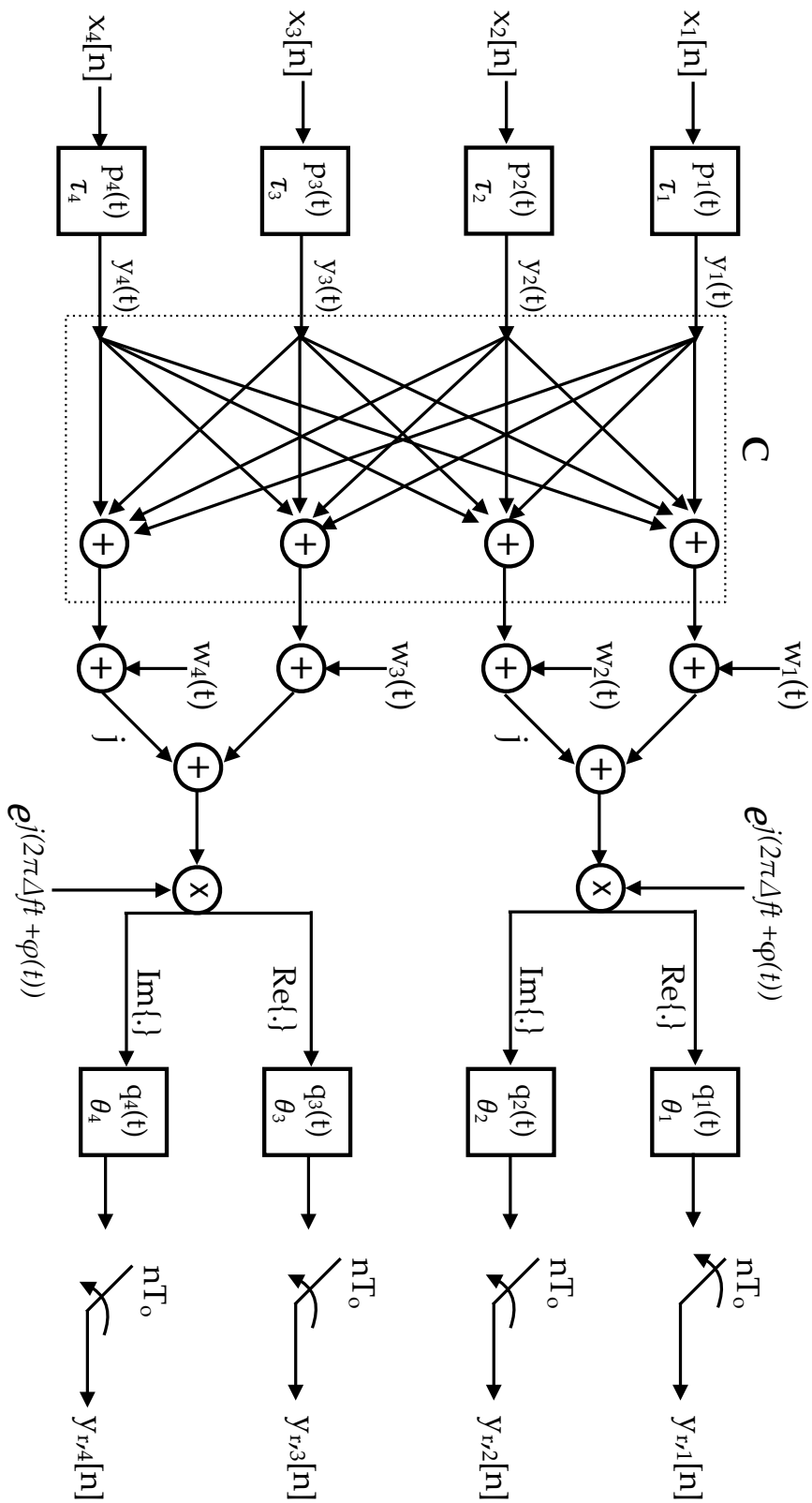
Figure 4.11: Baseband equivalent model of optical back-to-back setup.

The overall output, $y_{r,i}(t)$ is given by the following equation:

$$y_{r,i}[nT_o] = \sum_{m=-\infty}^{\infty} \sum_{k=1}^{4} x_k[mT_s] \cdot s_k(nT_o - mT_s - \epsilon) \cdot c_{i,k} \cdot e^{j(2\pi\Delta fnT_o + \varphi(nT_o)} + w_i(nT_o) \quad (4.42)$$

The impulse response, $\mathbf{s} \in \mathbb{R}^{4 \times L}$ is the combined impulse response of the DAC, DA, DP-MZM and ADC as shown in Equation (4.30). The above model is slightly more complicated than its electrical scenario and hence requires more steps in the DSP to output signals which can be used by the DPC training block where coefficient estimation can be performed. We will discuss the required DSP steps in the following subsection.

4.5.1 Suitable DSP for Optical Back-to-Back

Similar to Section 4.4.1, suitable algorithms have to be implemented at the receiver and transmitter to obtain corresponding input signals to the DPC block in optical back-to-back configuration. The required setup and DSP blocks are shown in Figure 4.12.
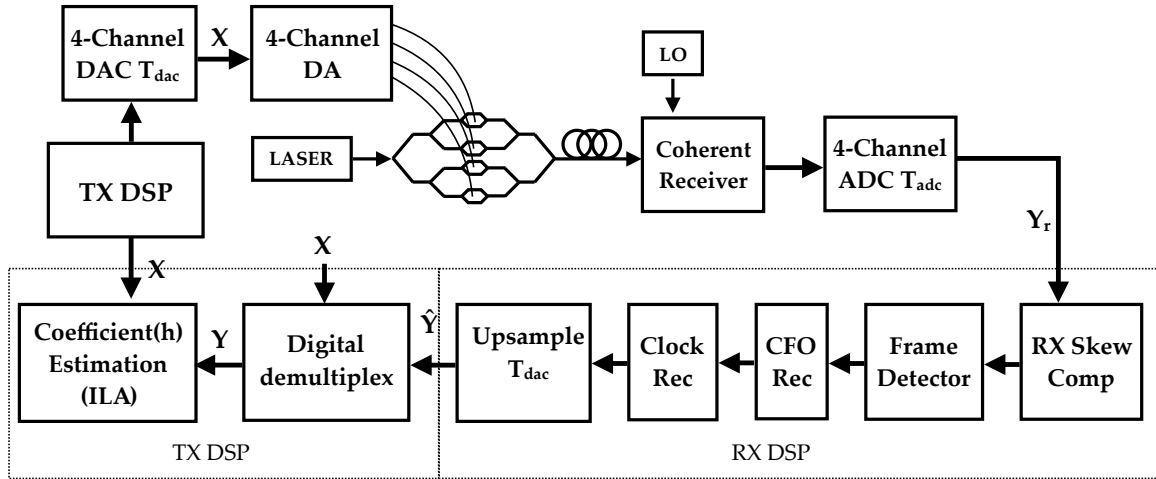
Figure 4.12: DPC architecture for optical back-to-back.

The individual DSP blocks can be divided into the receiver DSP chain and transmitter DSP chain. The receiver DSP block makes use of standard receiver algorithms and forwards the signal to the transmitter DSP block.

At the receiver, the received signals, $\mathbf{Y_r}$ have to be first synchronized. This is achieved by implementing a series of time and frequency synchronization algorithms. The receiver skew is first to be compensated in the incoming digital signals. This is followed by a frame

detector, CFO recovery block and a clock recovery block. Finally, depending on the sampling rate of the ADC and receiver DSP, the samples are upsampled to the DAC sampling rate and sent to the transmitter DSP. A detailed analysis of the synchronization blocks is beyond the scope of this thesis. A description of the blocks is provided in Section 3.7.2 and we will just briefly discuss the required receiver DSP blocks.

Receiver skew compensation

An estimate of the receiver skew can be obtained by sweeping the skew values and optimizing it for the minimum BER at a particular modulation format and baud-rate for a fixed ROSNR. Let us denote the estimated receiver skew values in samples as :

$$\hat{\theta} = [\hat{\theta}_1, \hat{\theta}_2, \hat{\theta}_3, \hat{\theta}_4] \tag{4.43}$$

The receiver skew can then be subsequently compensated for each $i - th$ tributary as :

$$y_{i,rx-skew}[n] = \mathcal{F}^{-1}\left(\mathcal{F}(y_{r,i}[n]) \cdot e^{j(2\pi f \hat{\theta}_i)}\right) \tag{4.44}$$

where $\mathcal{F}$ and $\mathcal{F}^{-1}$ are the Fourier and Inverse Fourier transform operator.

Frame detector

Please refer to Section 3.7.2 for this DSP component.

Coarse CFO estimation and compensation

As seen from Section 3.7.2, perfect synchronization of the transmitter and receiver LASER is not possible in real systems. Nevertheless, in case of DPC in homodyne configuration the CFO block can be omitted. In the thesis, the DPC was implemented in an intradyne configuration. In such a configuration, the transmitter and receiver LASER could have a frequency offset in the order of~1 GHz. For CFO compensation algorithm, the reader is refered to Section 3.7.2.

Clock recovery

After implementing the CFO estimation and compensation algorithm, the received digital signal at this point in the DSP chain could be written as :

$$y_{r,i}[nT_o] = \sum_{m=-\infty}^{\infty} \sum_{k=1}^{4} x_k[mT_s] \cdot s_k[nT_o - mT_s - \varepsilon] \cdot c_{i,k} + w_i[nT_o] \qquad (4.45)$$

where ε is the timing error.

After employing one of the various algorithms mentioned in Section 3.7.2, the synchronized output samples after the clock recovery block is:

$$y_{r,i}[nT_o] = \sum_{m=-\infty}^{\infty} \sum_{k=1}^{4} x_k[mT_s] \cdot s_k[nT_o - mT_s] \cdot c_{i,k} + w_i[nT_o] \qquad (4.46)$$

Upsampling

After the carrier and clock synchronization, the samples are upsampled to the DAC sampling rate and sent to the transmitter DSP block.

Digital Demultiplex

The digital demultiplexing block was developed in this thesis as an addendum to the DPC block. This block forms a crucial part before samples are sent to the DPC block. Due to the arbitrary polarization rotation of the optical signal introduced from the DP-MZM and the fiber, each received tributary of the 4-D vector, $\hat{\mathbf{Y}}$ contains a mix of all transmitted tributaries. De-multiplexing of the mixed tributaries and mapping them to the respective $\mathbf{Y}$ is then mandatory. This block also consists of a delay estimation and synchronization routine.

After coherent demodulation and carrier and clock synchronization, the upsampled digital signal, $\hat{\mathbf{Y}}$ is given as :

$$\hat{y}_i[nT_o] = \sum_{k=1}^{4} c_{i,k} \cdot y_k[nT_o - \tau_{i,k}] \cdot + w_i[nT_o] \qquad (4.47)$$

We first assume that the filters $\mathbf{p}$ and $\mathbf{q}$ are all-pass filters and introduce only a delay. This is necessary to facilitate the estimation of the transfer matrix, $\mathbf{C}$. Equation (4.47) can be re-written as:

$$\hat{y}_i[nT_o] = \sum_{k=1}^{4} c_{i,k} \cdot x_k[nT_o - \tau_{i,k}] \cdot + w_i[nT_o] \qquad (4.48)$$

where $c_{i,k}$ are unknown coefficients of the transfer matrix, $\mathbf{C}$ and $\tau_{k,i}$ are the unknown gross delay $\in \mathbb{R}^{4 \times 4}$ between k^{th} transmitted and i^{th} received tributary.

The first step is calculation of a delay matrix, $\tau_{\mathbf{g}} \in \mathbb{R}^{4 \times 4}$. Delay $\tau_{i,k}$ between k^{th} transmitted and i^{th} received tributary is estimated as :

$$r_{i,k}[n] = \mathcal{F}(\hat{y}_i[n]) \cdot (\mathcal{F}(x_k[n]))^* \tag{4.49}$$

where $\mathcal{F}$ is the Fourier transform operator for the digital signals and $\mathbf{r_{i,k}}$ is the cross-correlation vector. The delay is then given as:

$$\tau_{i,k} = \operatorname{argmax} \mathcal{F}^{-1}(\mathbf{r}_{i,k}[n]) \tag{4.50}$$

After substituting the estimated $\tau_{i,k}$ in Equation (4.48), we can represent it in the following matrix notation :

$$\hat{\mathbf{Y}} = \mathbf{C} \cdot \mathbf{X} + \mathbf{W} \tag{4.51}$$

Equation (4.51) is an over-determined linear system of equations with more equations than unknowns and can be solved by ordinary least squares [71]. The estimated channel matrix, $\hat{\mathbf{C}}$ is calculated as:

$$\hat{\mathbf{C}} = \left(\mathbf{X} \cdot \mathbf{X}^T\right)^{-1} \cdot \hat{\mathbf{Y}} \cdot \mathbf{X}^T \tag{4.52}$$

where T is the transpose operator.

$\hat{\mathbf{C}}$ can then be used to find $\mathbf{Y}$:

$$\mathbf{Y} = (\hat{\mathbf{C}})^{-1} \cdot \hat{\mathbf{Y}} \tag{4.53}$$

The estimated de-multiplexed 4-D signal, $\mathbf{Y}$ is then forwarded to the coefficient estimation block where the DPC coefficients are found by using the method outlined in Section 4.2.1.

4.6 System Model : Far-End Receiver

Until now we have gone through the functioning of the DPC in training mode by evaluating the electrical and optical back-to-back setups. The optical back-to-back setups are most often used to perform calibration of the transmitter components at the time of man-

ufacturing or deployment. Such schemes need an auxiliary receiver at the transmitter. Another elegant solution is to make the estimation of the DPC coefficients possible after receiving from a *far end* receiver. Far-end means the receiver is located several kms from the transmitter and is not co-located. Such a DPC architecture could further empower the characterization of the transmitter components and facilitate the continuous tracking of transmitter imperfections without requiring an auxillary receiver. The system block diagram is similar to Figure 5.6, but instead of going back-to-back we consider N spans of fiber with erbium doped fiber amplifier (EDFA)s.

We consider the operation of the optical system in linear regime and neglect the nonlinearities from the fiber. In this case, the optical fiber only attenuates the signal and distorts the signal with CD. The received optical signal is demodulated using intradyne detection. Receiver effects such as carrier frequency offset and clock offset remain the same as explained in the previous section.

4.6.1 Suitable DSP for Optical Feedback from Far-End Receiver

The attenuation introduced by the optical fiber is compensated by using EDFAs. In addition to compensating for the receiver effects, the receiver DSP must include a block to compensate for the accumulated CD.
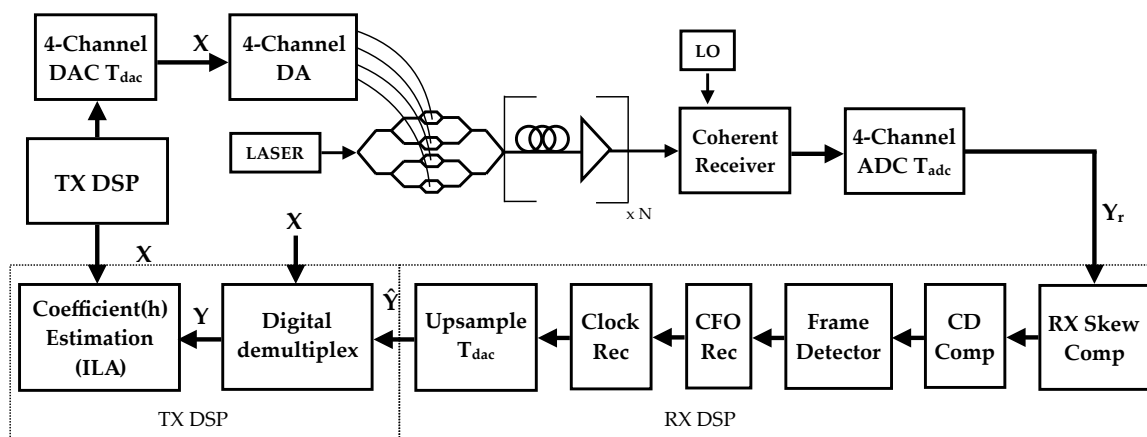

Figure 4.13: DPC architecture for feedback from far-end receiver

Before CD compensation, the appropriate receiver skew values are first compensated.
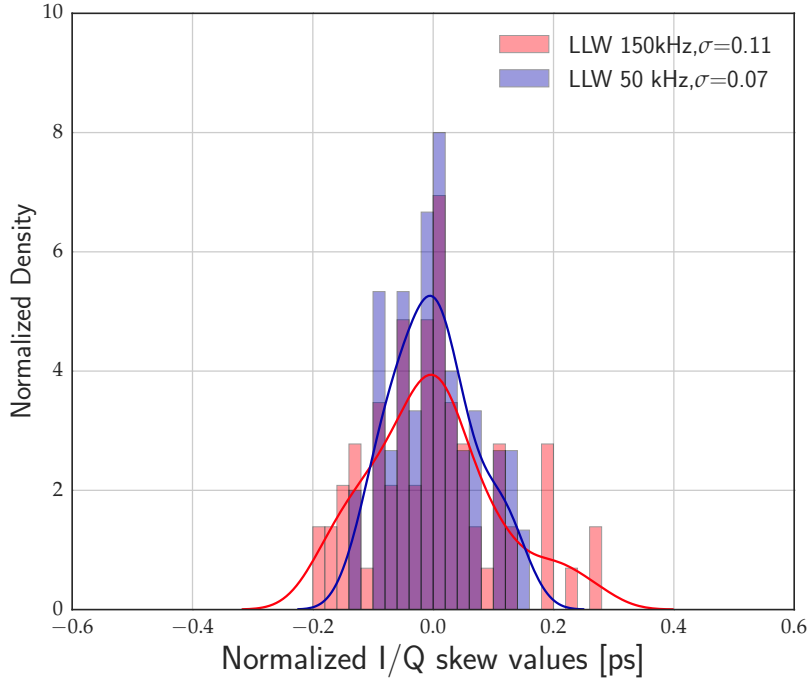
Figure 4.14: Effect of different LLW on transmitter I/Q skew estimation.

CD compensation

The collected CD in the digital signal can be compensated by a simple inverse transfer function explained in Section 3.7.2, After CD compensation, the signal is further processed using the same blocks as explained in Section 4.5.1 to recover the signal required for coefficient estimation.

4.7 Building an Accurate DPC Block with a Phase Noise Canceller

In our discussions, we have gone through the three scenarios, namely electrical back-to-back, optical back-to-back and optical feedback from far-end receiver and have analyzed the procedures to estimate the coefficients of the DPC block using indirect learning architecture. We have also studied the characteristics of the LASER in Section 3.1 where it was mentioned that there are no ideal LASERs. All LASERs impair the transmit signal due to their non-zero LASER linewidth (LLW) and introduce phase noise in the signal [72].
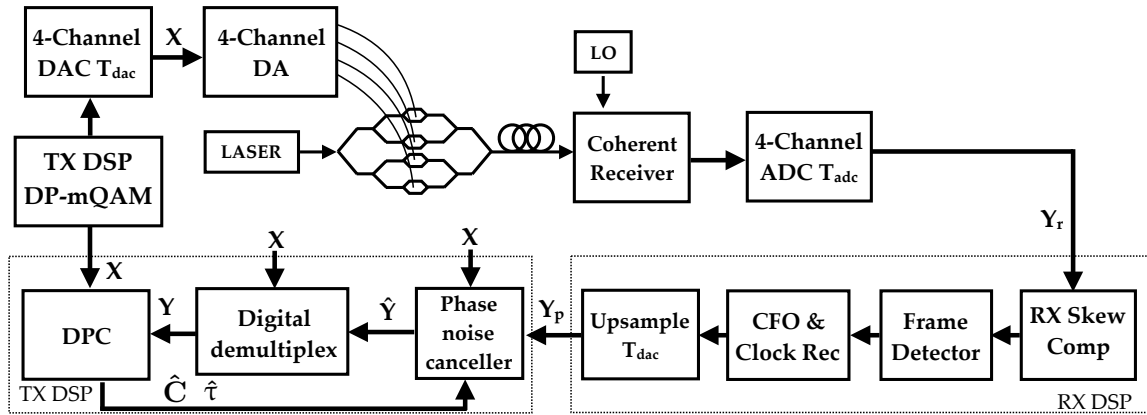
Figure 4.15: DPC architecture with PNC

While performing various experiments to calculate the coefficients of the DPC block, we also carried out analysis to study the impact of various LASERs with low and high LLWs. The impact of the LLWs was recorded by performing DPC coefficient estimation multiple number of time and collecting the transmitter I/Q skew values obtained thereafter. A histogram of the estimated skew values was plotted. The standard deviation of the value is the chosen figure-of-merit which reflects the effect of LASER on estimated value. A higher value of standard deviation, meaning a broader curve points to a worse LASER (higher LLW and hence more phase noise). This is clearly seen in Figure 4.14. The red curve with a higher standard deviation refers to a higher LLW LASER and the one with a sharper peak is the one with a lower LLW. The blue curve therefore, on an average will give a transmitter I/Q skew value which is more reliable than the one delivered by the algorithm when a worse LASER source is employed.

For system vendors, the cost of the transponders plays a significant role in the system design. LASERs with lower LLW ($\sim$ 1-100 kHz) are more expensive than the LASERs with higher LLW. In order to cut costs, a cheap LASER might be used which leads to an inaccurate DPC coefficient estimation. In order to circumvent this problem a DSP solution is desired which is able to overcome the phase noise effects of cheap LASERs with higher LLW. To alleviate the effects of LASER phase noise, a phase noise canceler was implemented [35] in the thesis. As the name signifies, this block removes the phase noise from the input signals to the DPC coefficient estimation block. The removal of phase noise, hence, makes the input signals to the coefficient estimation block cleaner, resulting in better assessment of the transmitter I/Q skew values. The working of the phase noise canceller (PNC) and its functioning with the DPC coefficient estimation block are explained here.

To start with, we will look at Figure 4.15 where the DPC architecture with a PNC is drawn. The receiver DSP remains the same as explained in the previous sections. An additional block of PNC is added in the transmitter DSP before the signals are sent to the digital de-multiplexer. 4-D signals, $\mathbf{Y_p}$ and $\hat{\mathbf{Y}}$ differ only by a phase noise term, $\varphi[nT_o]$. The phase noise is attributed to the LLW of the transmitter and the receiver LASERs.

For intradyne detection, we can write Equation (4.42) as:

$$y_{p,i}[nT_o] = \sum_{m=-\infty}^{\infty} \sum_{k=1}^{4} x_k[mT_s] \cdot s_k[nT_o - \tau_{i,k}] \cdot c_{i,k} \cdot e^{j\varphi[nT_o])} + w_i[nT_o] \qquad (4.54)$$

where $\varphi[nT_o]$ is the system phase noise (see Figure 4.11). We consider the same phase noise on both the polarizations since the same LASER is used for both the polarizations. We are essentially interested in finding out the phase noise vector and do an inverse operation on the signals $\mathbf{Y_p}$ to obtain phase noise free signals, $\mathbf{Y}$. Such an operation would look like :

$$\hat{\mathbf{Y}} = \mathbf{Y_p} \cdot e^{-j\hat{\varphi}[nT_o]} \qquad (4.55)$$

with $\hat{\varphi}[nT_o]$ being the estimated phase noise. The following section will go over the procedure to estimate phase noise.

4.7.1 Phase Locked Loop for Phase Noise Estimation

A conventional 2nd order PLL is utilized to estimate the phase noise $\hat{\varphi}[nT_o]$ [73]. The working of the PLL is shown in Figure 4.16. The PLL operates in a proportional-integral mode with a numerically controlled oscillator (NCO). K_p and K_i are the respective proportionality constants for the proportional and integral paths. The PLL estimates the phase noise and also removes any residual CFO. The parameters of the PLL can then be derived as :

$$K_p = 2\zeta\omega_n \qquad (4.56)$$

$$K_i = \omega_n^2 \qquad (4.57)$$

$$\omega_n = \frac{2B_n}{(\zeta + \frac{0.25}{\zeta})} \qquad (4.58)$$

where ζ is the damping factor, ω_n is the natural frequency of the loop filter and B_n is the

noise bandwidth of the PLL. $\hat{\phi}[n]$ is read at the output of the NCO.

What is important here is to check the input signals required for the PLL. The PLL block works on a dual-polarization signal. It expects two 4-D signals, $\mathbf{X}$ and $\mathbf{Y_p}$, an initial estimate of the transmitter I/Q skew values and an estimate of the channel matrix, $\hat{\mathbf{C}}$. The following gives a step-wise procedure to estimate the phase noise and obtain signals, $\mathbf{Y}$ from $\mathbf{Y_p}$.

The procedure for calculating the DPC coefficients with the aid of a PNC proceeds in the following manner. Note that each of these steps work on a frame-by-frame basis. A frame means that a block of N samples of $\mathbf{Y_p}$ and $\mathbf{X}$ are obtained and each of the given operations are performed on this frame.

- **Step 1** In the first step, the PNC is disabled and the standard procedure of DPC as explained in Section 4.5.1 and Section 4.2.1 is employed. This step yields an initial estimate of transmitter I/Q skew vector, $\hat{\boldsymbol{\tau}}$ and channel matrix, $\hat{\mathbf{C}}$.

- **Step 2**

  Input signals, $\mathbf{X}$ are processed with the estimated skew vector $\hat{\boldsymbol{\tau}}$ and then transformed with the channel matrix $\hat{\mathbf{C}}$ to signals $s_X[n]$ and $s_Y[n]$. At the same time, signals $\mathbf{Y_p}$ are obtained and transformed to signals $r_X[n]$ and $r_Y[n]$ by the simple operation (for sake of brevity the operations are shown only for the samples $s_X[n]$ and $s_Y[n]$) :

$$s_X[n] = \hat{x}_1[n] + j\hat{x}_2[n] \tag{4.59}$$
$$s_Y[n] = \hat{x}_3[n] + j\hat{x}_4[n] \tag{4.60}$$
$$r_X[n] = y_{p,1}[n] + jy_{p,1}[n] \tag{4.61}$$
$$r_Y[n] = y_{p,3}[n] + jy_{p,4}[n] \tag{4.62}$$
$$\tag{4.63}$$

The resulting signal, $\mathbf{r}$ differs from $\mathbf{s}$ only due to the additive noise, $\mathbf{w}$ and phase noise, $\varphi(t)$ (refer Figure 4.11). The phase difference between the two signals is measured and is used as the input to the PLL. This phase difference is fundamentally the phase noise contained in the signal. The PLL follows this phase noise and gives an

estimate of this phase noise given by $\hat{\varphi}[n]$.

$$\mathbf{r} = \mathbf{s} \cdot e^{j\hat{\varphi}[nT_o]} + \mathbf{w} \tag{4.64}$$

- **Step 3**

  After estimating $\hat{\varphi}[n]$, signal $\hat{\mathbf{Y}}$ is then calculated using the conjugate of estimated phase noise by using Equation (4.55).

The signals, $\hat{Y}$ after the removal of phase noise can then be used further in the digital-demultiplexing block. Since the input to the block is free from the phase noise it is expected that the end estimation of the DPC coefficients and the transmitter I/Q skew will be more exact. The results related to this section are discussed further in Section 5.5
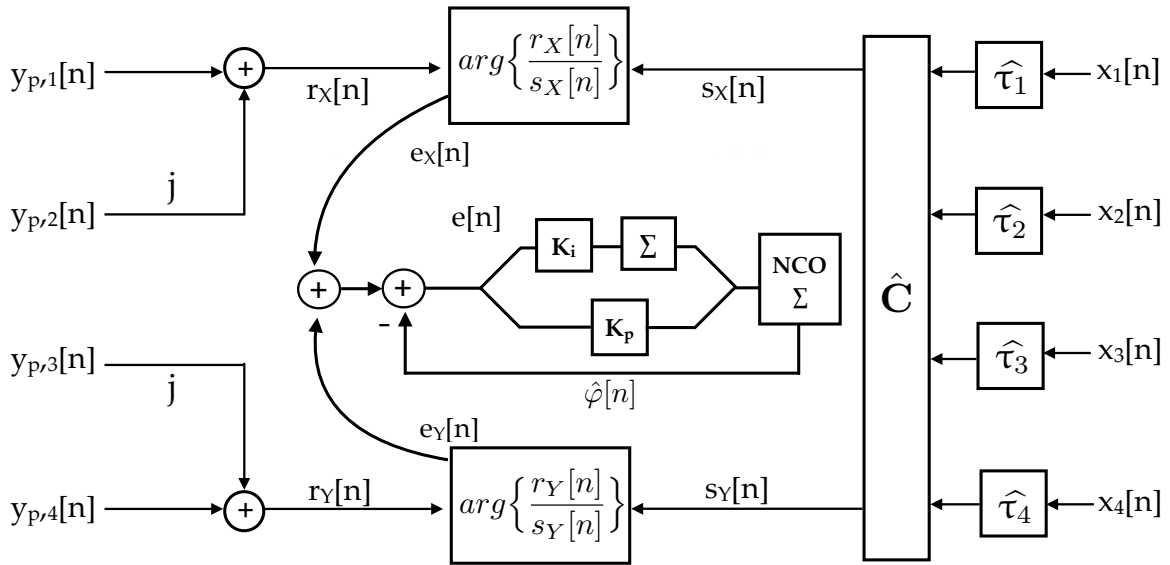

Figure 4.16: Estimation of phase noise with a PLL

4.8 Summary

In this chapter, the main principles of DPC are formally introduced.

The memory polynomial, the ILA and feedback from receiver are the three main principles of the proposed DPC. A detailed analysis of the chosen memory polynomial model is presented where the memory polynomial model is shown as a trade off between a Volterra series and Taylor series. ILA which forms the core of the DPC is described.

The problem for the identification of DPC coefficients is analyzed in Section 4.2.1 and a least squares solution for the same is discussed.

Four configurations of feedback from receiver are illustrated. For each of the configurations, an analogous system model and the required receiver DSP blocks are provided.

The simplest dual polarization electrical back-to-back setup with the corresponding system model is first presented. This is followed by the classical optical back-to-back system. A precise system model discussing filtering, polarization rotation and transmitter and receiver I/Q skew is provided. A detailed breakdown of the required receiver DSP blocks consisting of receiver I/Q skew compensation, frame detection, CFO compensation, clock recovery and upsampling is reviewed.

The solution for the de-multiplexing of the polarization multiplexed signal before DPC is derived. This block forms an indispensable part of the transmitter DSP and could be included within the DPC block.

DPC over the optical fiber with feedback from receiver is analyzed. Finally a PNC based on a 2nd order PLL is introduced to enable an even finer estimation of transmitter I/Q skew.

In the next chapter experimental results for the various configurations are demonstrated and discussed. The following chapter serves as an experimental proof-of-concept of the main ideas developed in this chapter.

5

Experimental Validation

In chapter 4, the memory polynomial model and ILA were explained as basic building blocks of digital pre-compensation (DPC) block. We analyzed various electrical and optical back-to-back configurations and formed the mechanism to obtain the DPC coefficients in the respective scenarios.

In this chapter, experimental proof of the proposed DPC scheme implemented on various system configurations will be presented and discussed. As a starting point, experiments are conducted with the most basic electrical back-to-back scheme and the complexity of the setups is then increased gradually. Such an approach enables a systematic way to analyze the limitations of the components one by one and permits a methodical approach to compensate for the same. A recap of the central memory polynomial model equation used to model the inverse of the transmitter components equation is provided here :

$$z[n] = \sum_{p=1}^{P} \sum_{m=0}^{M} h_{m,p} y^{p}[n - m] \tag{5.1}$$

where P is the order, and M is the memory depth accounted for in the system and h_m, p are the respective coefficients. The above model can be adopted according to the system under consideration. Henceforth, Equation (5.1) will always be used for modeling the transmitter. For each of the investigated systems, a corresponding memory polynomial model (Eq. 5.1) is chosen and the DPC architecture is implemented. For the special case of a linear system Equation (5.1) becomes,

$$z[n] = \sum_{m=0}^{M} h_m y[n - m] \qquad (5.2)$$

whereas for the modeling of the non-linearities, Equation (5.1) retains its form. The following experimental setups were investigated for the implementation of the DPC algorithm:

1. Electrical back-to-back with DP-mQAM signals at 37.41 GBaud

2. Optical back-to-back with DP-mQAM signals across baud rates from 32 GBaud up to 57 GBaud

3. Optical back-to-back in a highly non-linear transmitter

4. Optical feedback from a far-end receiver with 200 Gbit/s and 400 Gbit/s signal transmission

5. Accurate estimation of transmitter I/Q skew with a phase noise canceler with single carrier 400 Gbit/s and 600 Gbit/s signals

We will now take up each of these experimental setups individually and explain the results obtained.

5.1 Electrical Back-to-Back

The results of this section are based on the article [15]. Owing to its simplistic nature the electrical back-to-back setup is the first setup which was investigated in the thesis. In such a setup the DAC is directly connected to the oscilloscope as seen in Figure 5.2. Since we focus here on linear effects, namely the 3-dB bandwidth limitation of the DAC and the transmitter I/Q skew, the memory polynomial model of Equation (5.1) reduces to a simple FIR filter written as :

$$z_i[n] = \sum_{m=0}^{M} h_{m,p} y_i[n - m] \qquad (5.3)$$

where z_i and y_i are the respective input and output signals of the system for each ith ($i = 1,2,3,4$) tributary. Figure 4.3 depicts the implementation of ILA in an electrical back-to-back environment. In this case, 11 linear taps were used to model the system.
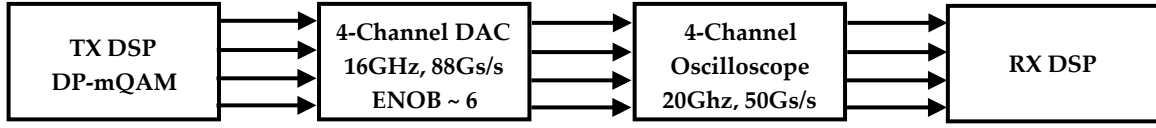
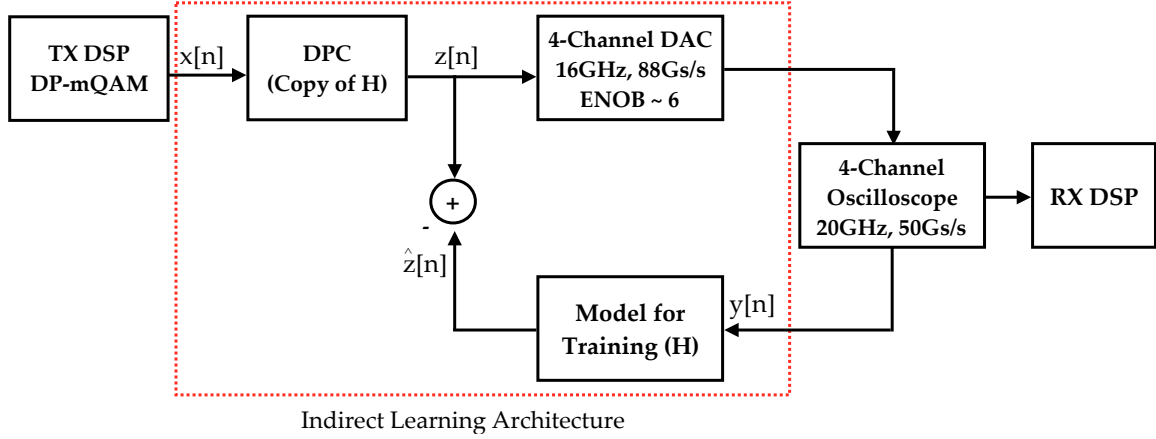Figure 5.1: Experimental electrical back-to-back setup

Figure 5.2: ILA in electrical back-to-back setup

5.1.1 Experimental setup

The performance of the DPC algorithm was verified in a dual polarization environment in an electrical back-to-back scenario. The standard setup consists of 4 channels, each corresponding to the I and Q channels of the two polarizations. The experimental setup consists of a transmitter which is realized by a 4-channel high-sampling rate DAC with internal memory to store the transmit waveform. The DAC is operating at 88 Gs/s, has a 3-dB bandwidth of 16 GHz and a ENOB of 6 [48]. A transmission signal baud rate of 37.41 GBaud is chosen. Such a baud rate facilitates the working of the DAC in its 3-dB bandwidth limited region, since the measured bandwidths of the DACs was barely 12-13 GHz (see Figure 3.9). At the receiver, a 4-channel digital storage oscilloscope with 3-dB bandwidth of 20 GHz with sampling rate 50 Gs/s is used to capture a shot of 500,000 samples for each of the four tributaries.

In each iteration suitable RRC Nyquist pulses with roll-off 0.2 at 37.41 GBaud for DP-16QAM, DP-32QAM, DP-64QAM, DP-128QAM and DP-256QAM are uploaded to the DAC. The RRC pulses aren't a necessary requirement and any PRBS can be used to run the procedure. The transmitted as well as the captured signals are used to adapt the DPC model according to the steps outlined in Section 4.4. Once the DPC coefficients have been esti-

mated, the coefficients are copied to the DPC block and DPC is switched from the training to the working mode.

Experimental results are obtained for all the above modulation formats with the respective signals with and without DPC.

5.1.2 Experimental Results

For sake of brevity, the gains obtained from DPC are plotted here only for DP-64QAM 37.41GBaud signals. The trend however of the results remains consistent across all the other modulation formats. The gain obtained from DPC is assessed by looking at the following figure of merits before and after DPC:

- Compensation of 3-dB bandwidth limitation

- Mitigation of transmitter I/Q skew

- Reduction in electrical back-to-back BER

Bandwidth compensation

The PSD of the input signal, i.e., the desired signal to be transmitted and the two received signals namely the output signal without any DPC and output signal with DPC are plotted in Figure 5.3. The input signal follows the spectrum of a DP-64QAM 37.41 GBaud signal with Nyquist pulse shaping. It is seen in the PSD of the signal without any DPC that the higher frequency components suffer from the low bandwidth effect of the DAC and the oscilloscope (although in this setup the major limitation comes from the DAC). In contrast however, almost a flat spectrum is obtained when input signals with DPC are sent in to the transmitter and the corresponding output signals are captured and analysed.

Transmitter I/Q skew

The group delay of the 4 channels of a DP-mQAM signal, i.e. XI, XQ, YI and YQ with and without DPC are plotted in Figure 5.5a and Figure 5.5b respectively. The calculation of the group delay is carried out according to Section 4.4.2.

A transmitter I/Q skew of almost 4 ps is observed in the X polarization and about 1 ps is noticed for Y polarization. Moreover, a frequency dependence of the skew is seen.
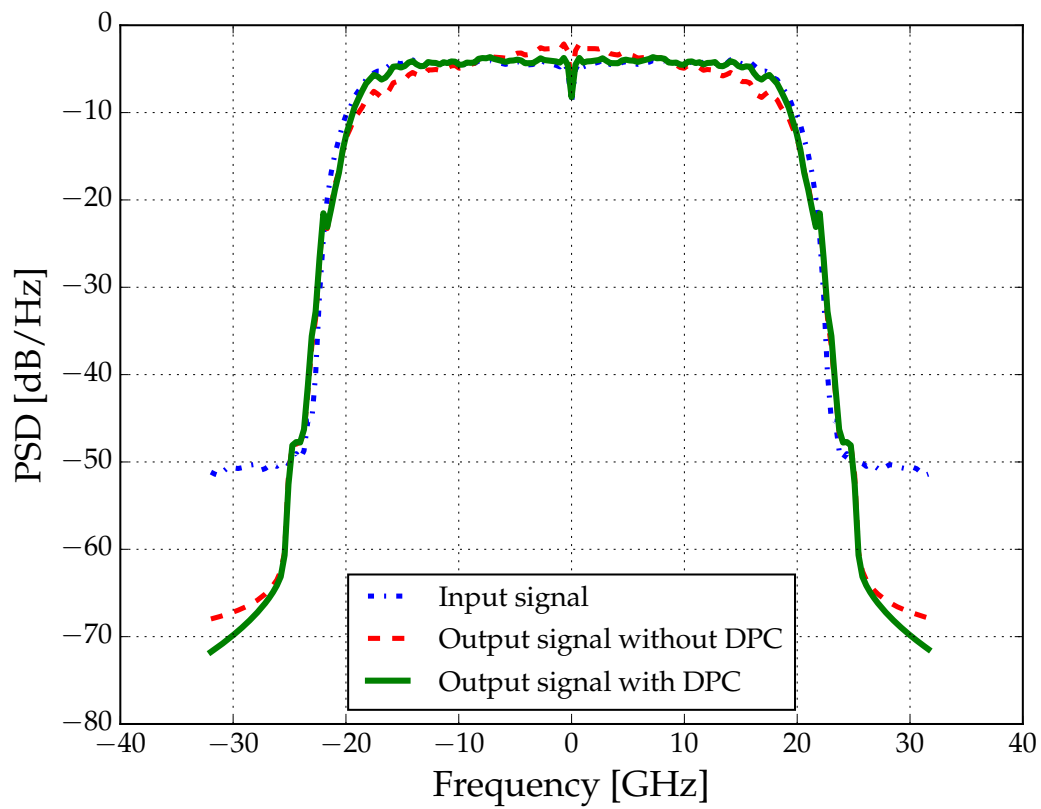
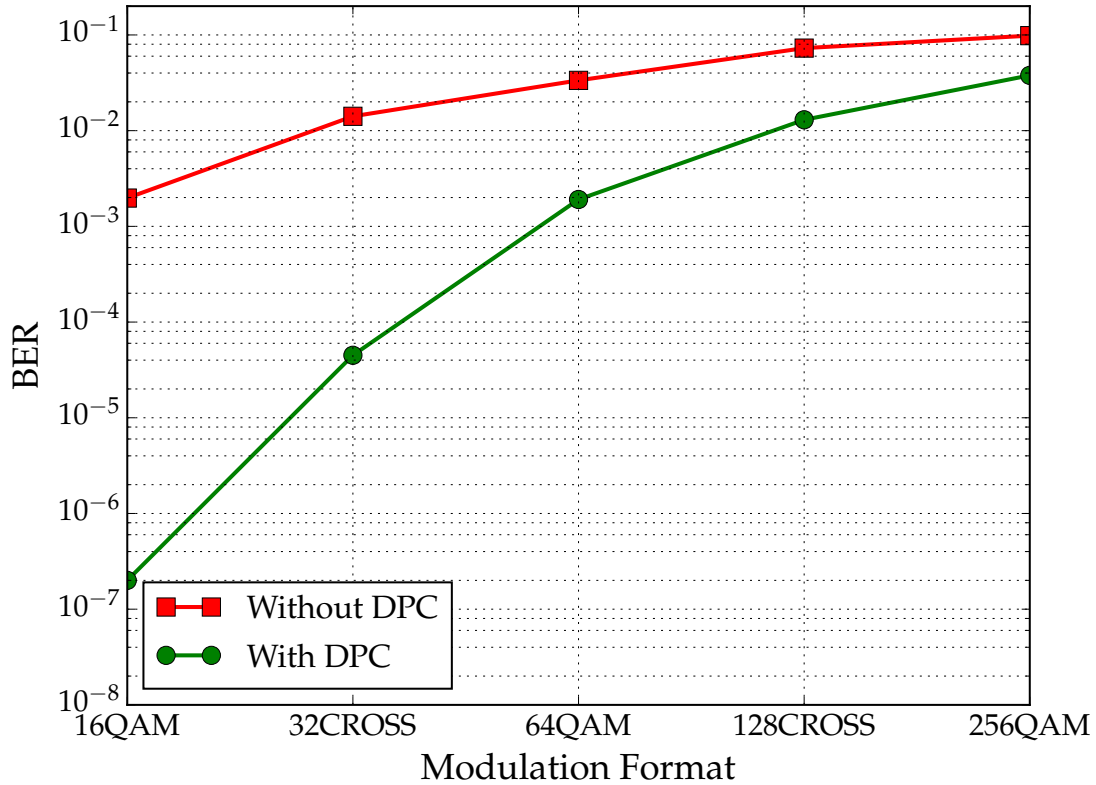Figure 5.3: PSD of DP-64QAM signals at 37.41 GBaud with and without DPC

Figure 5.4: Electrical back-to-back BER for DP-mQAM 37.41 GBaud signals

After uploading signals with DPC, and measuring the group delay, the transmitter skew is reduced to a maximum of 0.2 ps and the frequency dependent nature of the skew has also been mitigated.

Bit Error Rate

To asses the joint contribution from compensating the limited bandwidth of the DAC and the correction of the skew, a plot of BER in back-to-back constellation is plotted in Figure 5.4. Analogous to the BER vs OSNR, this measurement is simply used as an indicator of the improvement in the overall system performance. From the plot, it can be concluded that the DPC brings an improvement of several orders of magnitude for DP-16QAM and a substantial improvement for the other higher order modulation formats. The lower improvement for higher order modulation formats can be explained by the higher quantization noise present due to the limited resolution of both the DAC and oscilloscope.
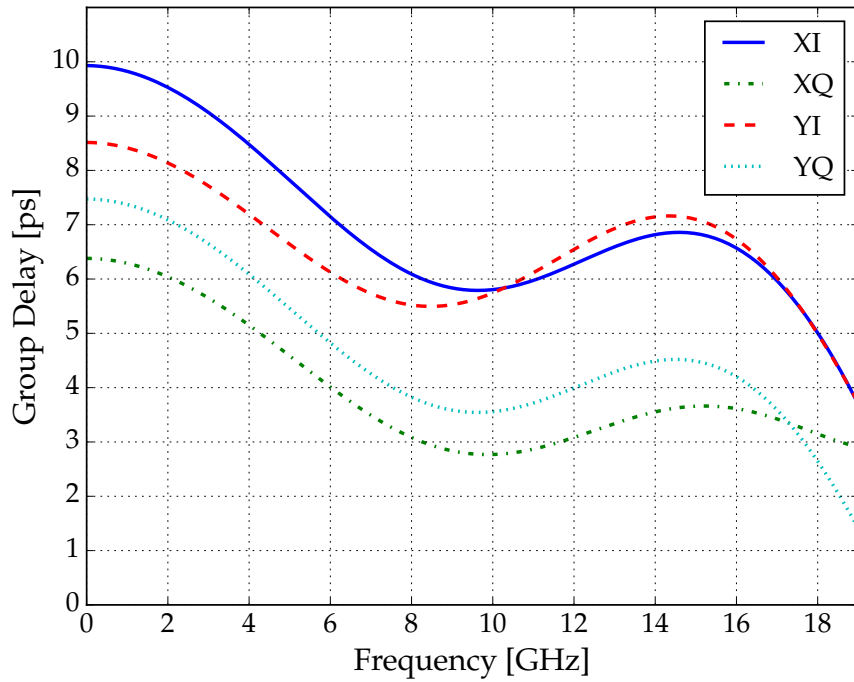
(a) Transmitter I/Q skew without DPC
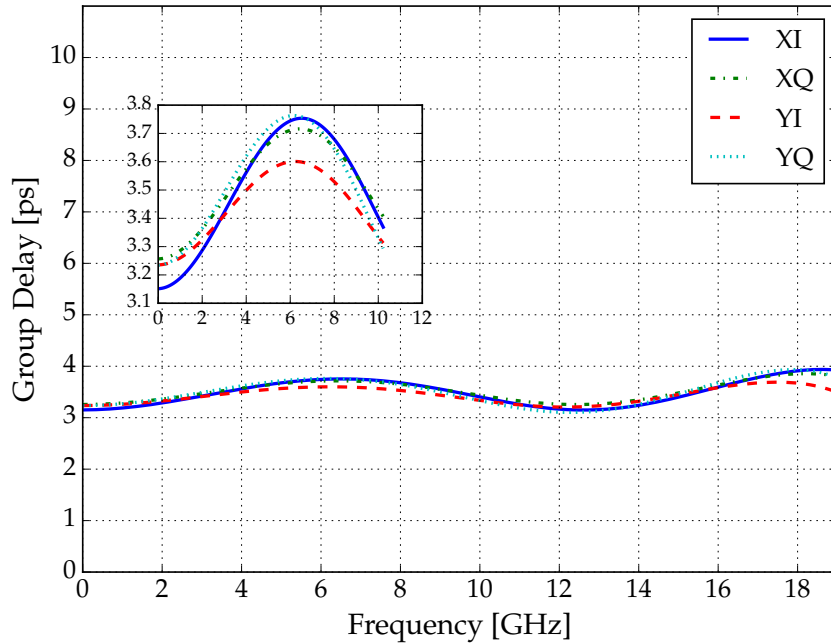
(b) Transmitter I/Q skew with DPC

Figure 5.5: Transmitter I/Q skew compensation

5.1.3 Summary

This experiment laid the initial foundations of the DPC scheme. DPC is used in the electrical back-to-back scenario to establish a proof of concept of the proposed algorithm across various modulation formats. The algorithm is capable of joint mitigation of transmitter frequency response and I/Q skew without need of any pre-knowledge of any of the electrical transmitter components. The results show significant improvement obtained by using the DPC scheme. Following this, the DPC scheme is enhanced to the optical back-to-back scenario which is more challenging and complicated than it's electrical counterpart.

5.2 Optical Back-to-Back : Weakly non-linear system

We will now take up the results of the utilization of the DPC block in an experimental optical back-to-back scenario. In comparison to the electrical setup, implementation of the scheme in this setup holds more practical relevance for optical system design and deployment. The results in this section are based on the publication [29]. The previous DPC algorithm in electrical back-to-back was extended to compensate the additional non-linear distortions and imperfections introduced by electrical driver amplifier (DA) and dual-polarization MZM. Let us start by looking at the experimental setup.

5.2.1 Experimental setup

Figure 5.6 shows the experimental setup as well as the signal flow for the DPC in the working mode. It consists of essentially two blocks : an optical transceiver and a DPC block.
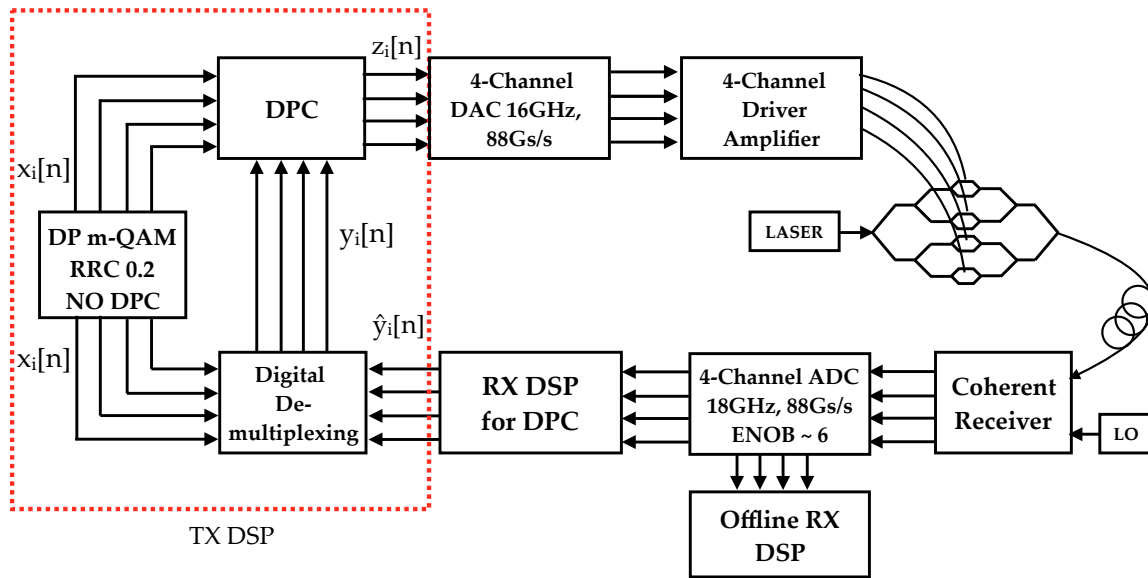
Figure 5.6: DPC with optical back-to-back setup

The optical transmitter consists of the same DAC with a 3-dB bandwidth of 16 GHz, sampling rate of 88Gs/s and ENOB of 6. Analog signals from the DAC are then amplified using an electrical DA. The operating point of the DA is kept in a fairly linear regime. The amplified output of the DA then modulates the incoming carrier wave of the LASER with the DP-MZM. The output of the transmitter is fed into a coherent receiver with a

short SSMF to make the back-to-back transmission possible. The optical front-end converts the incoming optical signals to the electrical domain. A high sampling rate ADC with sampling rate 80 Gs/s and 3-dB bandwidth of 18 GHz converts the analog signals to the digital domain. The ADC captures 5×10^5 samples for each of the four tributaries.

At the beginning of the training mode the DPC block is an identity block. DP-mQAM symbols are uploaded to the transmitter and sent over the setup. Once the digital samples are captured with the ADC, they are forwarded to the required receiver DSP blocks as already explained in Section 4.5.1, which includes: receiver I/Q skew compensation, frame detection, CFO compensation and clock recovery.

The upsampled samples at 88 Gs/s, $\hat{y}_i[n]$ are forwarded to the digital de-multiplexing block, where de-rotation of the incoming mixed tributaries takes place as discussed in Section 4.5.1. The de-multiplexed signals are then used for calculating the appropriate DPC coefficients, using the same procedure covered in Section 4.2.1. Once the corresponding inverse of the transmitter has been trained, the DPC coefficients are loaded onto the DPC block and is switched to the working mode. Now the transmitter is loaded with the new signals with DPC.

At the receiver, the incoming signals are first coherently demodulated with the optical front-end. The ADC captures shots of each incoming tributary and converts them into digital domain. Digital samples are then suitably processed in the receiver, where estimation and correction of CFO is performed. After data-aided 2×2 equalization and clock recovery, carrier phase estimation uses distributed pilot symbols to enable differential transmission. Finally, de-mapping is performed and BER is estimated by error counting.

5.2.2 Experimental results and discussions

To assess the affects of the DPC algorithm on the system performance, adaptive DPC was tested for DP-4QAM, DP-8QAM, DP-16QAM, DP-32QAM and DP-64QAM Nyquist signals with roll-off 0.2 at different baud rates (>32 GBaud). It is assumed that the receiver has been properly calibrated and the required steps before DPC as mentioned in Section 4.5.1 have been applied. It is also assumed that the receiver bandwidth is larger than the DAC which is a reasonable assumption for state-of-the-art DACs and their counterpart ADCs. The system is run in the weakly non-linear regime of the DA and DP-MZM and hence the following memory polynomial model for each ith tributary is considered :
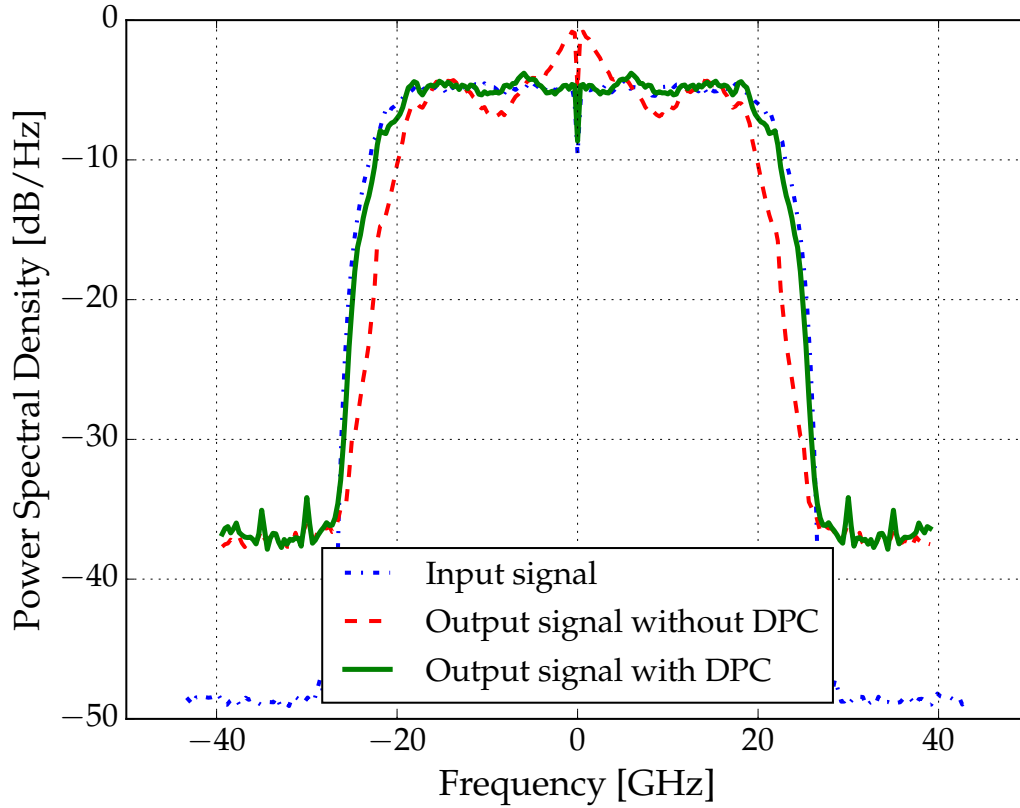
Figure 5.7: PSD of DP-64QAM signals at 40 GBaud with and without DPC

$$z_i[n] = \sum_{m=-7}^{7} h_{i,m,p} y_i[n-m] + h_{i,0,3} x_i^3[n] + h_{i,0,5} x_i^5[n] \tag{5.4}$$

where 15 linear taps and the main tap for non-linearity order of 3 and 5 are considered. The evaluation of the gains from DPC are presented in the following way:

- Compensation of transmitter 3-dB bandwidth

- Correction of transmitter I/Q skew

- Overall gain in ROSNR at a BER of 10^{-2}

Compensation of optical transmitter 3-dB bandwidth

Similar to the previous case, the PSDs of the input signal which is a DP-64QAM 40 GBaud signal, output signals with and without DPC are plotted. It is seen in Figure 5.7 that the

signals with DPC do not get affected by the 3-dB bandwidth limitation of the DAC, DA and DP-MZM and the spectrum is almost flat in the region of interest. In contrast to the electrical case, the noise floor is higher in the optical back-to-back measurements. This can be attributed to the additional noise from the DA, LASER and the EDFA in the transmitter.

Correction of transmitter I/Q skew

The measured group delay from the coefficients for the case without and with DPC is plotted in Figure 5.8a and Figure 5.8b. A skew of -0.4 ps and 2.5 ps is measured for the *X* and *Y* polarizations. The skew values for the optical case are obviously different than the electrical scenario because of the use of a different set of wires in the setup. The effect of transmitter I/Q skew is mitigated when samples with DPC are uploaded. This is seen in Figure 5.8a. What's more impressive to notice is the mitigation of the transmitter I/Q skew over the entire signal bandwidth which is not achieved with the samples without DPC.

Overall gain in ROSNR

In order to assess the overall gain obtained from DPC on DAC, DA and DP-MZM low pass filtering, I/Q skew and non-linear distortions, the ROSNR (0.1 nm) was measured in a back-to-back configuration at a BER level of 10^{-2}. The benefit obtained by using the algorithm is clearly seen in Figure 5.9. The figure shows the ROSNR plotted as a function of baud rate from 30 GBaud to 56 GBaud. Generating such high baud rates with low bandwidth components is a challenge in itself and the proposed algorithm clearly brings a gain.

A general consistent trend of increasing ROSNR gain with DPC is seen across all modulation formats. The gain increases with baud rate which is intuitive since high baud rate signals suffer more from low performance due to low bandwidth components. For DP-4QAM with DPC baud rates up to 56 GBaud could be realized with 16 GHz 3-dB bandwidth components. In comparison, DP-4QAM without DPC requires a sufficiently higher ROSNR even for a 51 GBaud signal.

Another observation is that at any symbol rate, higher order modulation formats exhibit a higher gain and benefit from DPC than their lower order counterparts. This is due to the higher sensitivity to non-linear effects for the higher modulation formats even for the same baud rate and same system conditions. For e.g., for a 40 GBaud signal, an improvement in ROSNR of 0.8 dB for DP-4QAM, 1.1 dB for DP-16QAM, 2.3 dB for DP-32QAM is achieved. For DP-64QAM, transmission of 40 GBaud signal is not even possible without DPC. The highest achievable baud rate increases considerably for all considered modulation formats
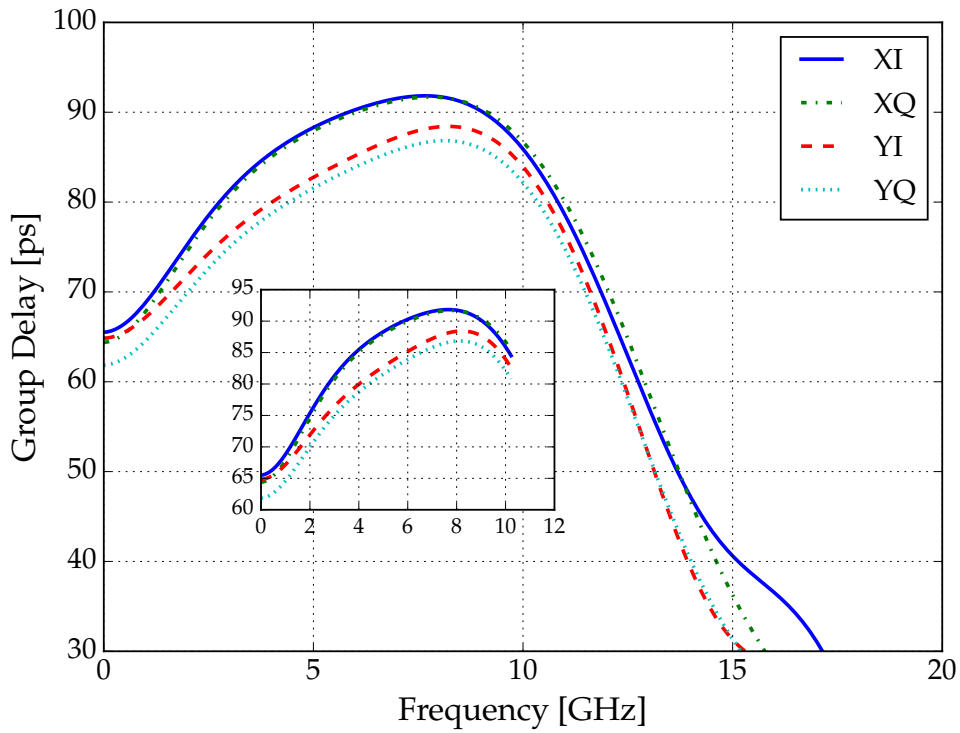
(a) Transmitter I/Q skew without DPC
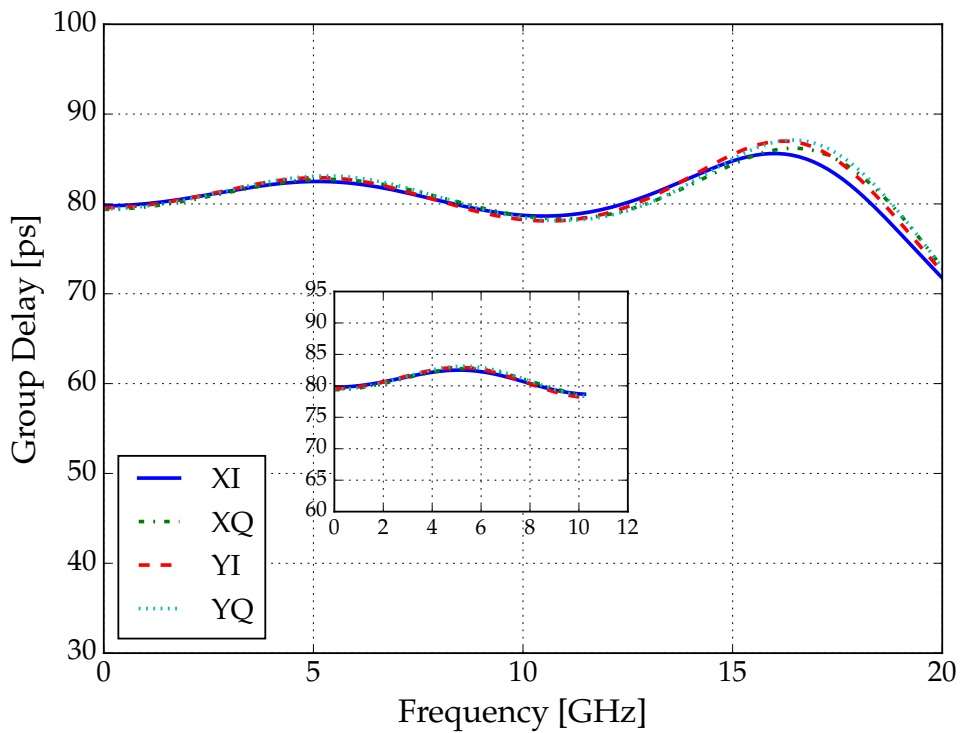
(b) Transmitter I/Q skew with DPC

Figure 5.8: Transmitter I/Q skew compensation
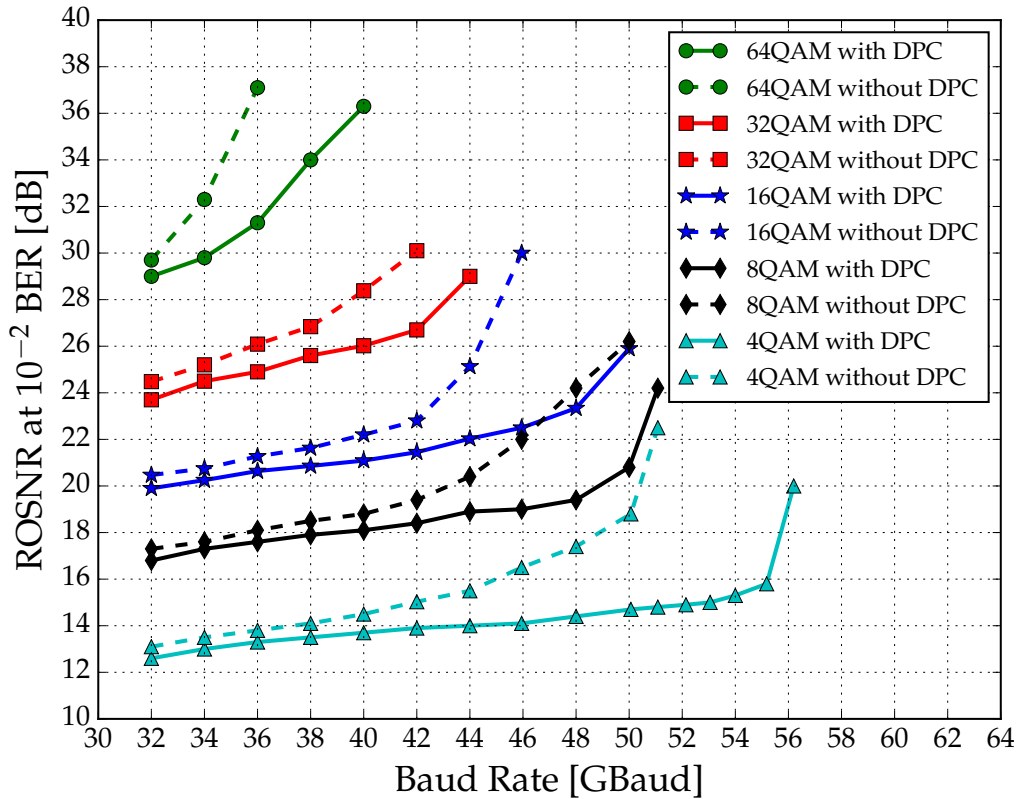
Figure 5.9: ROSNR with DPC in optical back-to-back for various DP-mQAM formats

for the considered transmitter and receiver components.

DPC Performance on the Number of Linear Taps

We will evaluate the performance of DPC with increasing number of linear taps. The analysis was carried out for a DP-16QAM at 34 GBaud signal. The Figure 5.10 shows how the error between the sent signal and the output signal obtained after DPC evolves with increasing number of taps. The experimental results confirm the assumption that as the number of taps will be increased, so will the resemblance of the output signal to the input signal. We observe that with only 1 tap, i.e. the case when no DPC is actually utilized, the error is the highest. A significant drop is observed when the number of taps are increased from 9 to 11 due to a further compensation of the bandwidth effect due to deeper memory depth. In the experiment, we employed a linear filter with 15 taps since baud-rates considerably higher than 34 GBaud are considered.
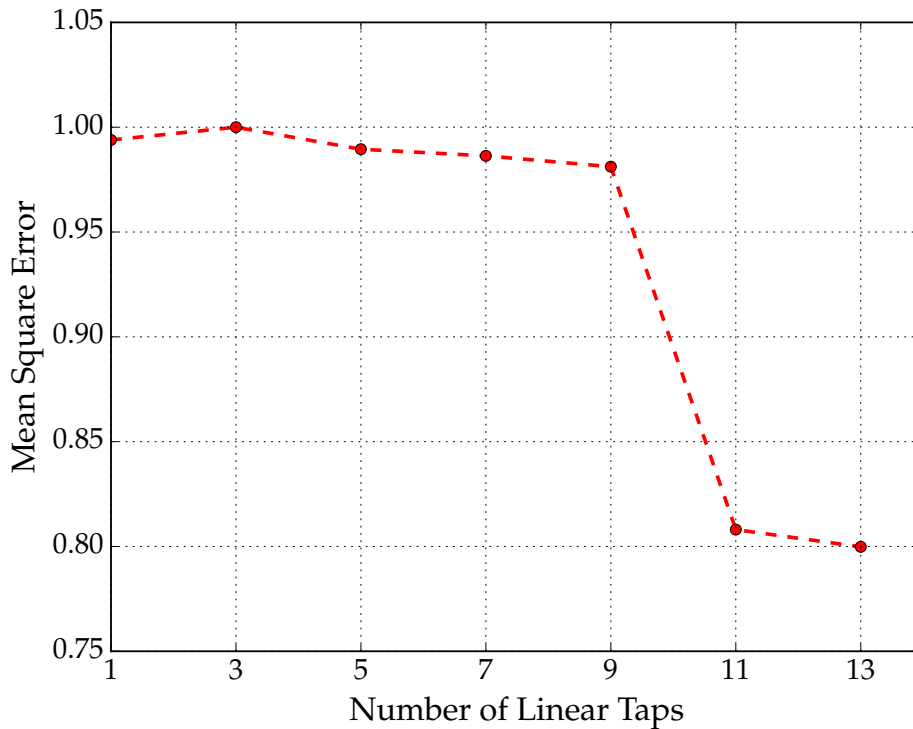
Figure 5.10: Mean square error with increasing number of linear taps

The result is however not exhaustive, since such an optimization of the number of taps is required to be done for each baud-rate separately. Nonetheless, 15 taps makes a good trade-off between performance and complexity induced due to the high number of DPC taps in hardware.

The PSD of the individual signals obtained after the corresponding DPC filters with variable number of linear taps is shown in Figure 5.11. The spectrum of signals generated with 1 and 3 number of linear taps clearly overlap the spectrum of the output signal without DPC. It is seen that the spectrum of the output signal becomes closer to the spectrum of the input samples with increasing number of taps, until a point when they all start to overlap each other, thereby confirm the trend of Figure 5.10.

A Note on Accuracy

Let us discuss here the accuracy of the DPC algorithm. It is difficult to quantify the quality of the DPC coefficients given by the ILA block of the DPC. One way which is adopted is to quantify the accuracy by collecting the estimated transmitter I/Q skew values over several
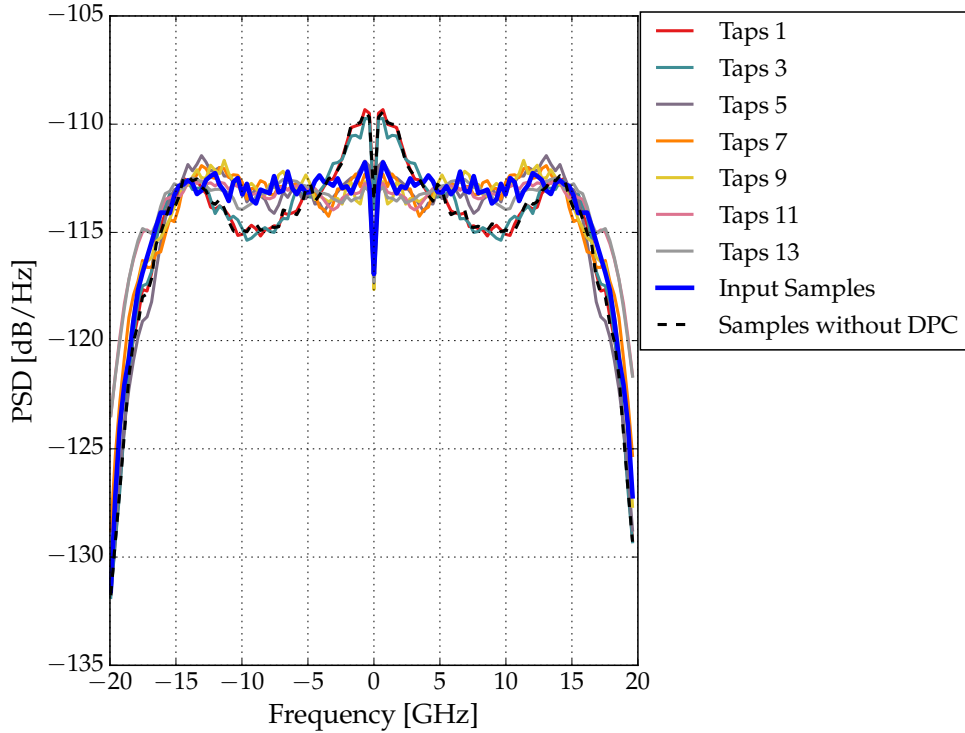
Figure 5.11: Power Spectral Density with increasing number of linear taps

measurements and then appraising the DPC coefficients based on I/Q skew estimation accuracy.

As studied, the DPC algorithm works by processing a set of N samples of the input and the output. This set of N samples is known as a frame. When we run the algorithm on hardware components, it is critical to understand how many of such frames are needed. Plus what is important is also to take into consideration the length of each of these frames. Figure 5.12 shows a relationship between the standard deviation and the number of frames utilized to estimate the transmitter I/Q skew. We evaluated this graph for 50 back-to-back measurements of I/Q skew estimation for a frame length of 50000 samples and 80000 samples for DP-16QAM and DP-64QAM samples respectively. The results are shown in Figure 5.12.

Each point on the graph corresponds to the standard deviation obtained over 50 measurements. The x axis denotes the number of frames utilized by the DPC algorithm to estimate a skew value. 1 signifies that the a single frame from the receiver was employed and 10 means that 10 such frames from the receiver were captured and then the estimation

was made. Obviously, the more the number of frames, the better is the estimation, which is seen from the decreasing standard deviation value. In the experiments, always a minium of 10 frames were used to estimate the DPC coefficients and hence the I/Q skew value. The initial higher standard deviation value for DP-64QAM could be due to the existence of imperfect carrier or clock synchronization. Nonetheless, for both the cases the standard deviation decreases to an acceptable value of < 0.1 ps. We will see later in Section 4.7, how this estimate could be made even better. In [38], the authors made a similar analysis but
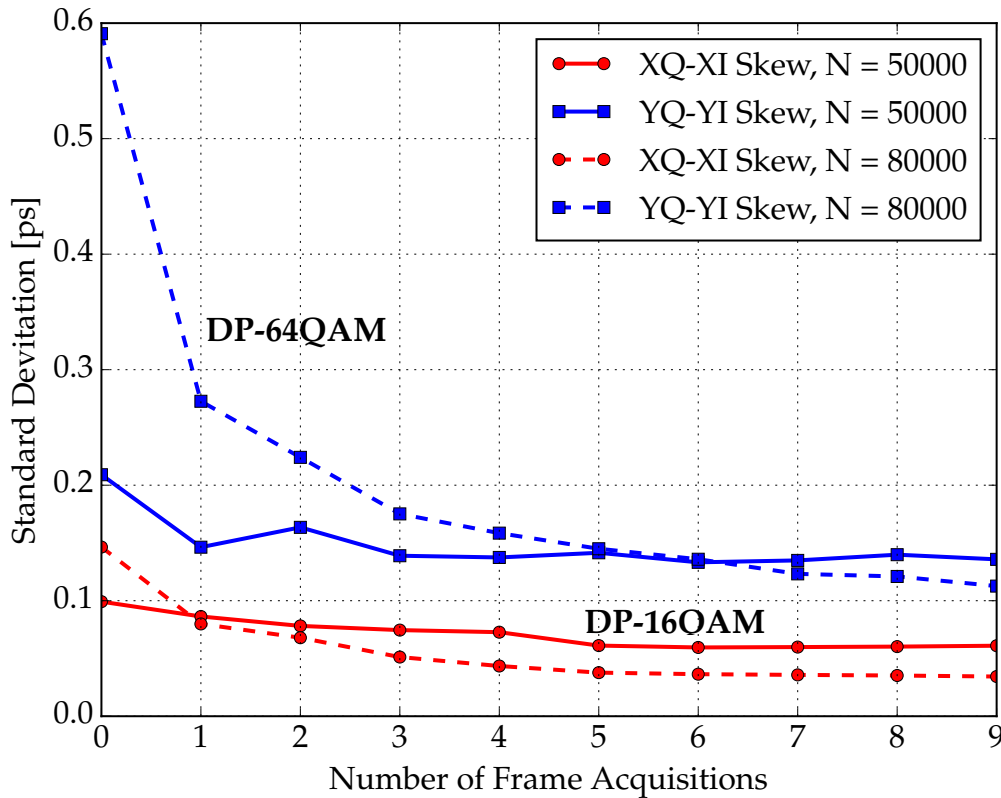
Figure 5.12: Standard deviation over several number of frames used for estimation

with frame with 16000 samples. Similar results were obtained there.

5.2.3 Summary

The proposed DPC algorithm was implemented in a linear optical back-to-back scenario and its performance was experimentally assessed over various higher order modulation formats, DP-4QAM, DP-8QAM, DP-16QAM, DP-32QAM and DP-64QAM. Mitigation of 3-dB bandwidth limitation and transmitter I/Q skew is shown. The attractive advantage to

this algorithm is it's capability to characterize the impairments without any individual measurements of the transmitter components.

5.3 Optical Back-to-Back : Highly non-linear system

One of the motivations to enable higher transmit output power is to assess the possibility of removing the additional EDFA at the transmitter. Additional EDFAs at the transmitter incur further costs and complexity to the design. The removal of the EDFA will however lead to lower transmit signal power, which is undesirable. There are then two possibilities to increase the transmit output power namely, increasing the digital signal power or increasing the analog gain of the electrical driver amplifier (DA). The digital signal power can only be increased up to a point when the penalty from the clipping of the DAC starts to surface. The transmit power can be further raised by increasing the analog gain of the electrical DA. Nonetheless this comes at the cost of higher non-linear effects in the transmitter. These non-linearities may lead to severe degradation in the system performance.

To overcome these distortions the DPC algorithm is adopted in a way to accommodate a non-linear digital pre-distortion part in the memory polynomial model. In this section, we discuss the application of the DPC scheme in highly non-linear transmitter components. The results documented in this section are based on the publication [22].

5.3.1 Experimental Setup

Since the same experimental setup is used, the reader is referred to Section 5.2.1.

5.3.2 Memory polynomial model

To model the additional non-linear effects, Equation (5.1) model is adopted. The model takes the following form for the identification of the DPC coefficients for each ith tributary:

$$z_i[n] = \sum_{m=-15}^{15} h_{i,m} y_i[n-m] + \sum_{l=-(L-1)/2}^{(L-1)/2} (h_{i,l,3} x_i^3[n-l] + h_{i,l,5} x_i^5[n-l]) \qquad (5.5)$$

The above model could be visualized as one part consisting of the linear model responsible for compensation of linear impairments and the last two terms included for additional mitigation of non-linear effects. In the non-linear part, non-linear order of 3 and 5 is considered with varying memory taps. Hence, 31 linear taps were imposed on the DPC block to compensate for the frequency response transmitter I/Q skew. For the non-linear term, with $P = 3$ and $P = 5$ with $L = 1$, signifying memoryless non-linearity and $L = 3$ and 5 memory taps are treated.

5.3.3 Experimental results and discussion

In order to examine the effectiveness of the additional non-linear DPD coefficients in the DPC block, a DP-64QAM system with various baud rates and various transmitter output powers was evaluated. Higher modulation formats such as DP-64QAM suffer the most from the non-linear distortions and therefore, are a suitable candidate to assess the performance of DPD. Moreover, DP-64QAM is seen as a suitable candidate to enable future 400 Gbit/s and 600 Gbit/s optical transponders.

In order to generate higher non-linearities at the transmitter the driver gain of the electrical DA was increased. This also provides an increase in total transmit optical output power.

DP-64QAM signals at 40 GBaud were generated at the transmitter and using the model in Equation (5.5) suitable DPD coefficients were generated. Digitally pre-compensated DP-64QAM samples were again uploaded into the transmitter. Performance of signals with and without DPC was then evaluated.

Gain attained from the non-linear DPC is assessed by comparing the ROSNR with and without DPC over various baud rates and transmitter output powers. The ROSNR is evaulated at a BER threshold of $4.2 \cdot 10^{-2}$

Effect of DPC on increasing TX output power

Figure 5.13 shows the ROSNR as a function of increasing MZM output power. The blue curve shows the ROSNR for a DP-64QAM 40 GBaud signal without DPC, but with manual skew compensation. It is clearly seen that the ROSNR increases as the output power increases. This is explained by the presence of higher non-linearities of the DA and DP-MZM as the driver gain is increased.

The green curve shows the performance curve when only linear DPC is realized. This involves using only the linear part of Equation (5.5) and, thus carrying out only compensation of 3-dB bandwidth and transmitter I/Q skew. In terms of performance improvement, the linear DPC provides the largest amount of gain of up to 3 dB at a transmit output power of -2 dBm. The next curve shows the calculation of DPC coefficients with the linear part and non-linear part but without any memory. In this case only the center tap is used for calculating the coefficients. This step leads to a further gain of around 0.8 dB in higher output power region. It is also observed that there is almost no gain from non-linear order taps at lower input power. After all, there are almost no non-linearities from the DA and DP-MZM at lower transmitter output power.
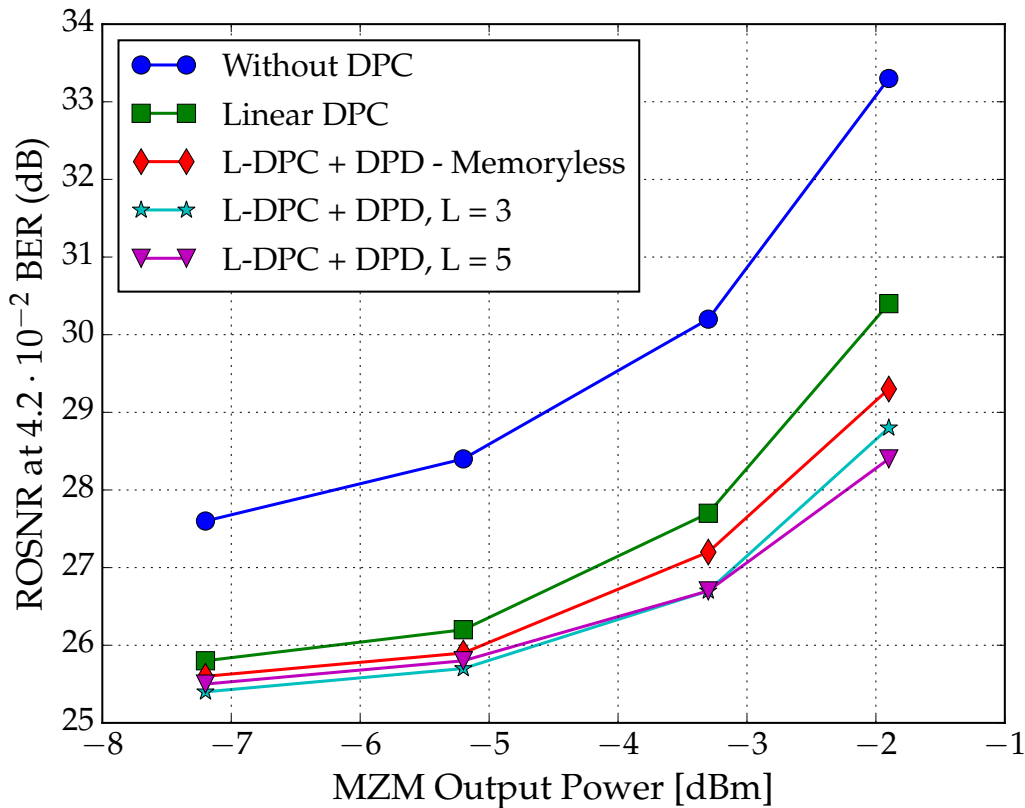
Figure 5.13: ROSNR vs MZM output power and gain with various DPC schemes for DP-64QAM 40 GBaud

DPC was also implemented for the case with $L = 3$ and 5 where memory was included in the higher order taps where an additional gain of 0.4 dB is obtained at a high transmit output power of -2 dBm. Results of memory taps $L = 3$ and $L = 5$ are shown to bring only minimal improvements in the performance. The trend of the graph conveys that the gain from non-linear DPC seems to saturate and adding additional non-linear order or memory taps would not lead to any drastic enhancement in it.

Non-linear energy factor

To quantify the contribution of the non-linear taps in the model the non-linear energy factor, as a figure of merit is defined as :

$$\text{Non-linear energy factor} = \frac{\sum\limits_{i=1}^{4} \sum\limits_{l=-(L-1)/2}^{(L-1)/2} h^2_{i,l,3} + h^2_{i,l,5}}{\sum\limits_{i=1}^{i=4} \sum\limits_{m=-(M-1)/2}^{(M-1)/2} h^2_{i,m,1}} \tag{5.6}$$

The non-linear energy factor is the ratio of the energy of the non-linear coefficients to the energy of linear coefficients.
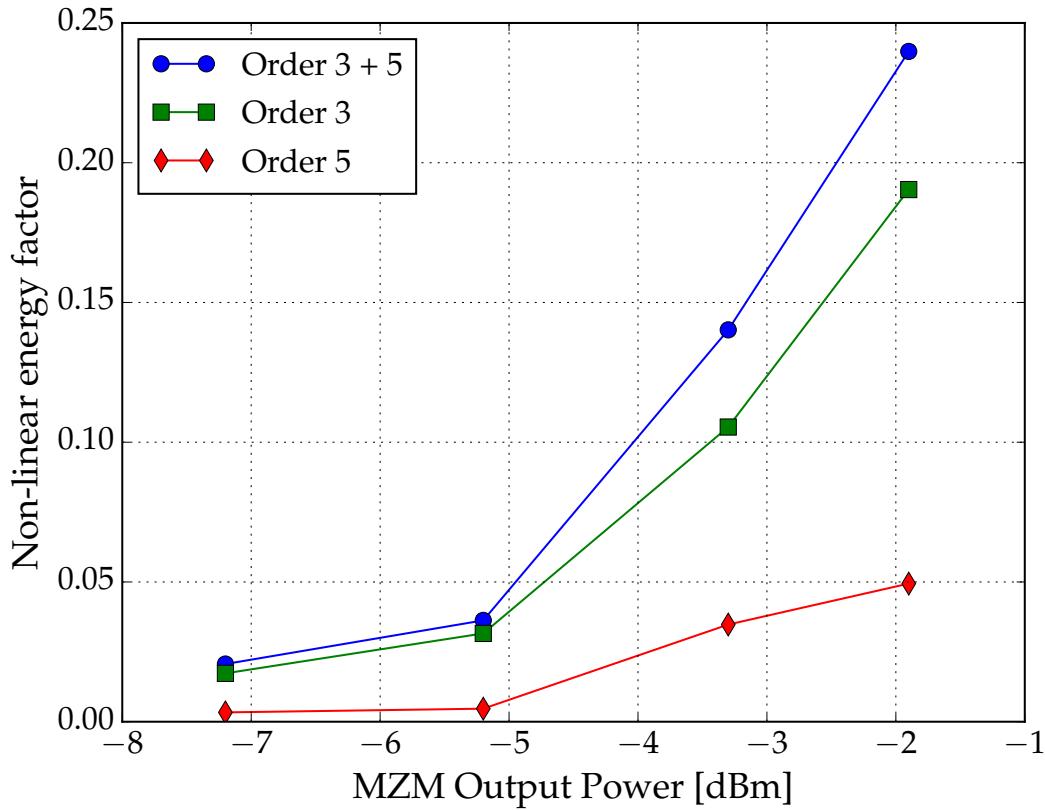
Figure 5.14: Non-linear energy factor vs MZM output power for DP-64QAM 40 GBaud

The normalized non-linear energy factor is plotted for $L = 3$ and $L = 5$ in Figure 5.14. It is seen in Figure 5.14 that the value of this factor increases with increasing transmit output power. Physically, this factor is a gauge for the degree of the non-linearities present in the transmitter. It is easy to perceive that for higher output powers this factor increases, implying the higher non-linearites which were mitigated with DPD. Another meaningful observation is that 3rd order non-linearities dominate the transmitter system and a minor

contribution is seen for order 5. This can be understood because both the DA and DP-MZM non-linear curve follows a cosine nature which can be mathematically modelled with a Taylor series polynomial having only odd order non-linearity. This again confirms the insight that a higher number of non-linear order taps will not bring any significant improvements. We haven't considered the impact of the even order taps. This is based on the assumption that the non-linearities arising from the electrical DA and DP-MZM follow a sine curve which doesn't need the contribution of the even-order terms to be modelled. This, however, could be taken up in the future to be evaluated in experiments.
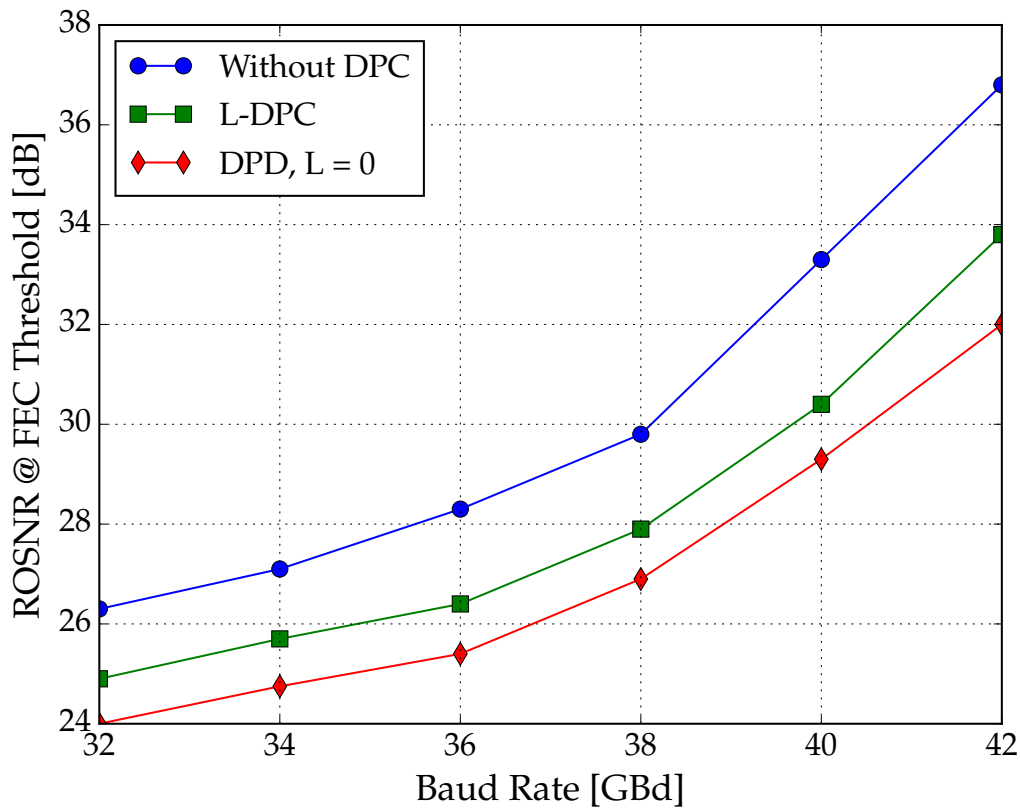
Dependence on baud rate

Figure 5.15: Dependence of ROSNR on baud rate for DP-64QAM signals

The dependence of ROSNR on baud rate for DP-64QAM signal is plotted in fig. 5.15. The DA gain was kept the same for all cases. Due to the difference in the baud rate of

the signals, there was a slight variation in the output transmit power, which varied within 0.3 dB from 32 GBaud up to 42 GBaud.

For each baud-rate, a linear DPC scheme and then a memoryless non-linear model was applied. The new samples with various DPC coefficients were uploaded and the corresponding ROSNR was measured. The blue curve shows the performance without any DPC. We observe a recognizable trend of increasing ROSNR with baud rate. In the first step, the green curve shows the performance with only linear DPC where the gain obtained in ROSNR gradually increases with increasing baud rate. The gain from implementation of the non-linear DPD, shown in red remains however uniform over the different baud rates.

5.3.4 Summary

We considered here the application of DPC in a highly non-linear optical transmitter. In order to achieve higher powers at the transmitter output, one option is to increase the analog gain of the electrical DA. This functional mode of the transmitter, however causes the non-linear effects to emerge. These non-linear effects damage the transmission signal quality and require a mitigation scheme. In this context, the DPC scheme is implemented by extending it to the non-linear model. The success of the scheme is demonstrated in experiments over distinct baud rates for a DP-64QAM signal. Contribution of the non-linear order is also reviewed where it is observed that increasing the non-linear order beyond 3 will lead to minor improvements in performance. This is further backed by the assessment of the contribution with the non-linear energy factor. Finally, the dependence of gain from non-linear DPC is evaluated over various baud rates, where the gain is seen to remain constant over the baud rates considered with an effective gain of more than 4 dB (between blue and red curve) at a baud rate of 40 GBaud.

5.4 Optical feedback from far-end receiver

In previous sections DPC was discussed in the scope of several back-to-back scenarios. The coefficient estimation was performed after receiving the feedback signals from a receiver located right next to the transmitter which necessitates the use of a secondary receiver with the transmitter. The identification of the DPC coefficients can then occur either at the time of manufacturing at the vendor side or at the time of deployment with the operators. A more refined solution could be to facilitate the identification of the DPC coefficients after collecting the feedback signals sent from a far-end receiver. Such a receiver can be located several kms away. One advantage of the scheme is that it saves the installation of the secondary receiver, thereby saving costs and cutting down the complexity. Plus, it also benefits the vendors by enabling a smoother porting of the DSP parameters required for the DPC. Such an architecture is also capable of continuous monitoring and compensation of transmitter imperfections. The results in this section are based on the publication [34]. Experimental setup and results are presented for various link configurations and the application of DPC for a state-of-the-art DP-16 QAM net 200 Gbit/s system as well as for a future optical DP-64 QAM 400Gbit/s (45.25 GBaud) systems.

5.4.1 Memory polynomial model

In order to avoid any non-linear effects arising from the fiber transmission we run the experiment in a purely linear environment. The modelling of the linear impairments of the transmitter is then performed by the following linear FIR model:

$$z_i[n] = \sum_{m=-15}^{15} h_{i,m} y_i[n-m] \tag{5.7}$$

5.4.2 Experimental setup

A field deployment scenario was emulated in the lab by building the setup shown in Figure 5.16. The transmitter and the receiver consist of the same components as mentioned in Section 5.2.1.

In addition to the transmitter and receiver, the setup consists of an optical fiber link with SSMF. The optical link consists of a configurable number of SSMF spans of 95 km with attenuation of 0.2 dB/km and CD of 16.9 ps/nm/km. The optical signal is amplified with EDFAs with a noise figure of approximately 6 dB. At the receiver, the signal is suitably
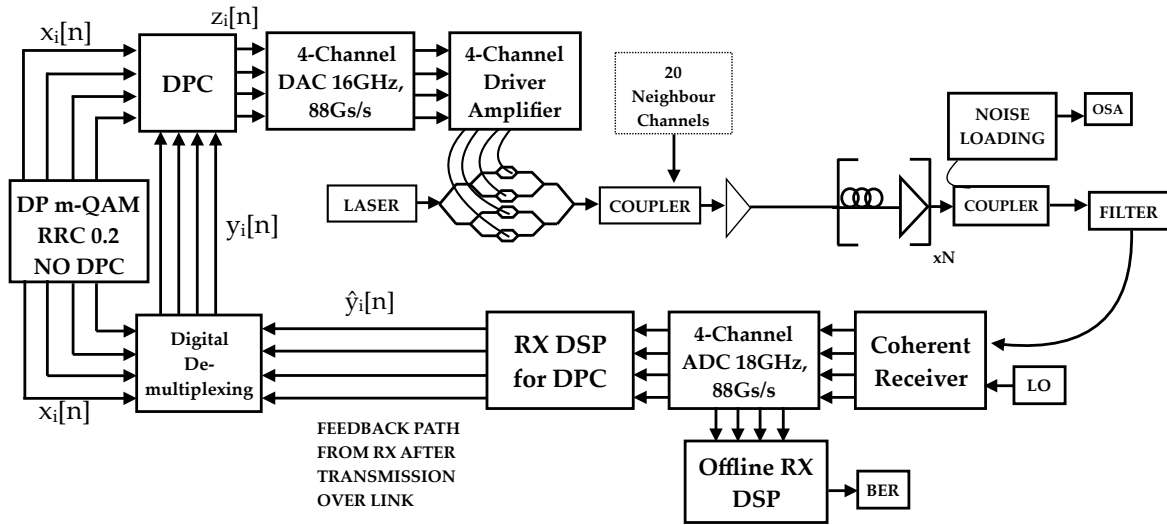
Figure 5.16: Experimental setup for DPC with feedback over fiber link

processed in the receiver DSP according to the steps mentioned in Section 4.6. The processed samples are then forwarded to the transmitter over a feedback channel. Note that the feedback channel is not required to be a high data-rate link. Once at the transmitter, the 4 tributaries are digitally de-multiplexed and appropriate DPC is performed to identify the coefficients.

In addition to the link, an additional block of noise loading is included in order to carry our several back-to-back BER vs OSNR measurements. The noise loading setup consists of a noise source consisting of EDFAs, an optical filter and a optical spectrum analyzer (OSA). The BER vs OSNR measurements are executed in the absence of the link for each scheme.

Suitable nyquist pulses with RRC filtering with roll off 0.2 are generated for DP-16QAM 34 GBaud and DP-64QAM 45.25 GBaud and uploaded to the DAC and the corresponding DPC coefficients are calculated.

5.4.3 Assessment methodology

The proposed DPC architecture over an optical fiber link is validated for DP-16QAM 200 Gbit/s and DP-64QAM 400 Gbit/s systems. For this purpose, DPC coefficients are first calculated in a back-to-back configuration and then over several link configurations in single and wavlength division multiplexed (WDM) setting. The capability of the DPC is evaluated for all the scenarios by comparing :

- the BER in back-to-back configuration measured as a function of OSNR

- the accuracy of transmitter I/Q skew estimation measured in terms of its standard deviation

Both the above criteria are very sensitive to the accuracy of the estimation of DPC co-efficients and have a direct impact on system performance.

Following notation is adopted to indicate the different scenarios investigated in back-to-back and over the link for m-QAM transmission :

- DPC-mQAM-B2B : DPC coefficients are calculated in back-to-back configuration

- DPC-mQAM-x km : DPC coefficients are calculated over x km of fiber in a single channel setup

- DPC-mQAM-x km WDM : DPC coefficients are calculated over x km of fiber in a WDM setup with 10 100Gbit/s channels on either side of the m-QAM test channel.

5.4.4 Experimental results

The back-to-back BER vs OSNR for the investigated scenarios are plotted in Figure 5.17. The solid curves show the theoretical curves for DP-16QAM at 34 GBaud (200 Gbit/s) and DP-64QAM at 45.25 GBaud (400 Gbit/s). For each curve, a set of DPC coefficients are obtained using the steps explained in Section 4.6 and then uploaded to the transmitter.

Respective BER vs OSNR curves are then measured using a suitable noise loading setup at the receiver.

From Fig. 5.13, it is clearly seen that both the modulation formats suffer from the the high penalty from bandwidth limitation and transmitter I/Q skew in the absence of DPC. Section 5.4.4 reports the ROSNR for various cases for a DP-16QAM 200Gbit/s signal. There is a gain of 0.4 dB when both the transmitter and receiver I/Q skew are compensated at the zero baseband frequency. Such a value could be obtained either by a brute force search or by using the value obtained from the DPC coefficients.

Another 0.4 dB gain is achieved when DP-16QAM 200Gbit/s samples with DPC are up-loaded. This decrease in ROSNR is attributed to the ability of DPC to further compensate for the 3-dB bandwidth limitation and the mitigation of the frequency dependent trans-mitter I/Q skew.

It is also noted that the back-to-back performance for the two cases of calculation of DPC coefficients, i.e. back-to-back and over 1520 km of SSMF remains the same.
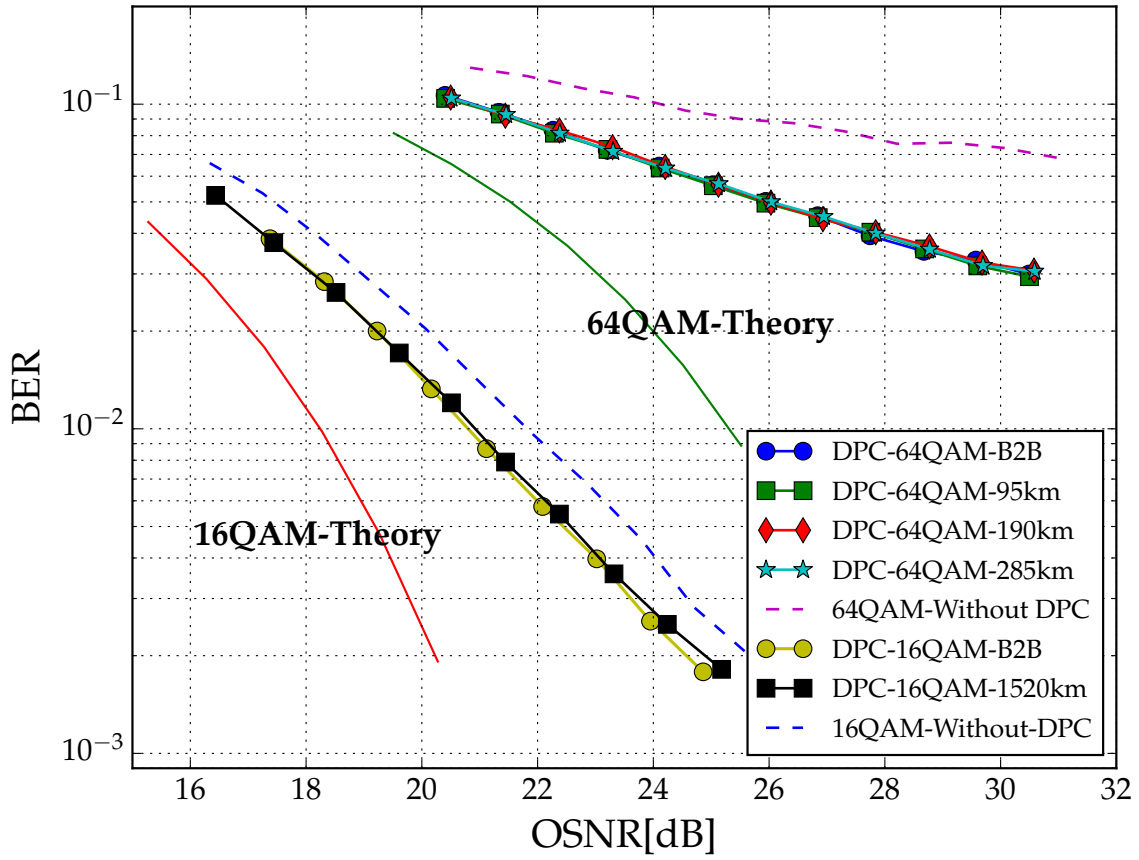
Figure 5.17: BER vs OSNR for DP-16QAM 200Gbit/s and DP-64QAM 400Gbit/s for DPC calculated over back-to-back and several link lengths

Scenario	ROSNR at 2×10^{-2}
Without DPC	20.0
With RX skew correction	19.6
With TX and RX skew correction	19.4
With DPC	19.0

Table 5.1: DP-16QAM ROSNR comparison

For DP-64QAM, four different scenarios of fiber length are examined. The coefficients in this case are calculated in a simple back-to-back setup and over 95 km, 190 km and 285 km of SSMF. These lengths are quite typical for present and next generation metro environments. For all the link scenarios, the performance of BER vs OSNR remains the same, denoting the practical feasibility of calculating DPC coefficients also over fiber lengths.

Figure 5.18: Histogram of estimated transmitter I/Q skew value for DP-64QAM 400Gbit/s over various fiber links

Another important indicator to quantify the performance of the DPC algorithm is the accuracy of estimation of the transmitter I/Q skew values. For this purpose, 50 runs of DPC algorithm are conducted for the presented scenarios. F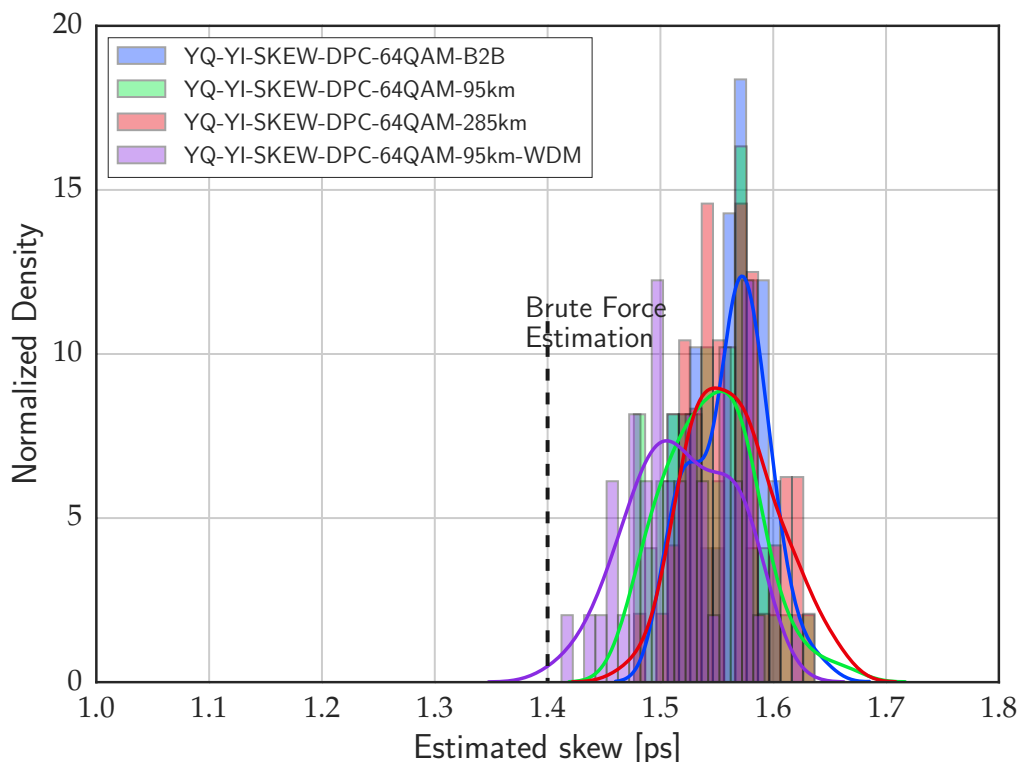or each run, the corresponding transmitter I/Q skew value is calculated from the estimated DPC coefficients as mentioned in Section 4.4.2.

Figure 5.18 and Figure 5.19 show the normalized histogram and the related density plots of the estimated transmitter I/Q skew values for one polarization, with a bin size of 0.01 ps to enable accurate reading of the skew value. In addition, the dashed line shows the measured transmitter I/Q skew value with a brute force scheme, in which the optimum transmitter I/Q skew is found by sweeping the I/Q skew and minimizing the BER. For the undertaken polarization, the brute force estimated I/Q skew value is ~ 1.4 ps. It is essential to know that the brute force measurement scheme is itself affected by measurement errors and the calculated value may not be exact.

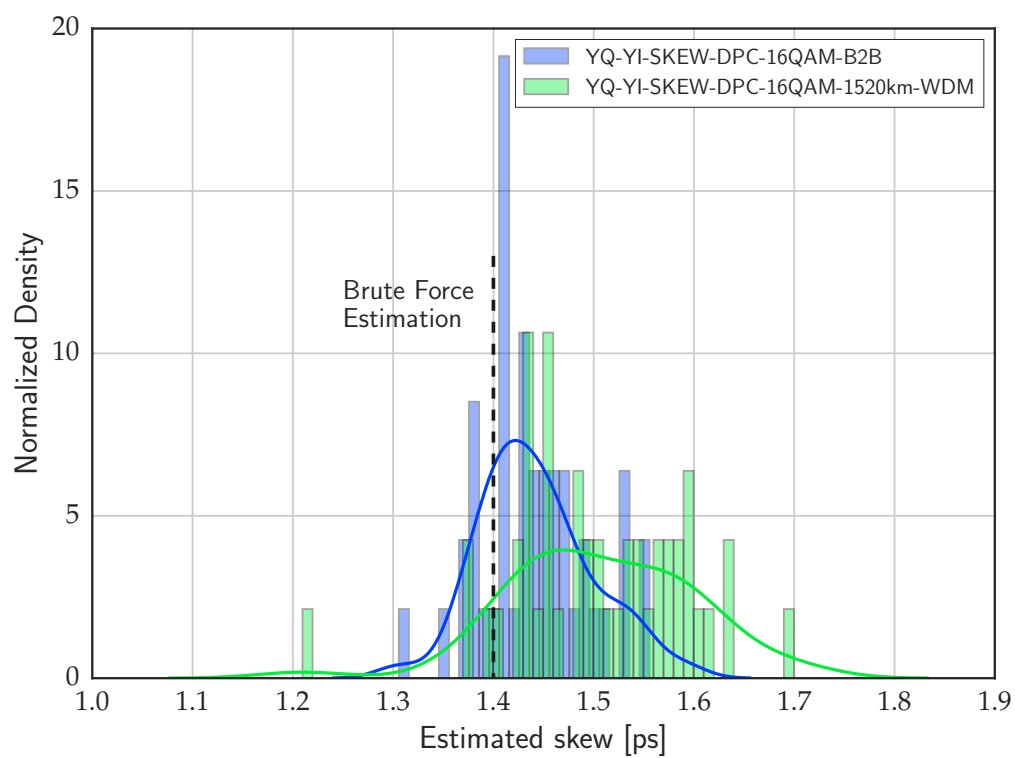In both the histograms, the different curves over various link configurations overlap and

Figure 5.19: Histogram of estimated transmitter I/Q skew value for DP-16QAM 200Gbit/s over various fiber links

the mean value of the estimated I/Q skew lies between 1.4 ps and 1.55 ps. It is also observed that the estimated skew value actually is very close to the value estimated from the brute force search and is within the margin of their respective measurement error.

For the case with DP-16QAM, there is one occurrence of the estimated transmitter I/Q skew value of 1.7 ps for the case when DPC is performed after 1520 km and WDM loading, which is 0.3 ps away from the actual I/Q skew value. Such an error in estimation is tolerable since DP-16QAM at 32 GBaud almost has no OSNR penalty at BER of 1×10^{-3} for a residual skew of 0.3 ps. With DP-64QAM at 45.25 GBaud, this tolerance to residual skew is even less. Nonetheless, the worst case is when the estimated transmitter I/Q skew lies at 1.6 ps which leads to an OSNR penalty < 0.5dB. This estimation can be further improved by using an additional processing block before DPC which will be discussed in the following section.

For both cases with DP-64QAM and DP-16QAM, the standard deviation of the estimates increases with the increase in link length. This can be explained because the feedback signal from the far-end receiver suffers from additional penalties, such as laser decorrelation and uncompensated interaction between receiver laser phase noise and CD. LASER phase noise and linewidth plays an essential role in the accurate estimation of DPC coefficients and the transmitter I/Q skew value. In the above experiment, LASERs with LLW 50 kHz were used. In the next section, an additional processing block to compensate for the LASER phase noise will be discussed.

5.4.5 Summary

This section takes up the case when the feedback signal is received from the far-end receiver instead of from the secondary receiver co-located with the transmitter as discussed in previous scenarios. In contrast to preceding situations, this DPC architecture is capable of continuous monitoring and mitigation of the transmitter imperfections by evaluating a tapped signal from the far-end receiver. While the auxillary receiver is also adept to provide this functionality, collecting feedback from the far-end receiver saves the additional cost and complexity from the auxillary receive which is incurred in the back-to-back case. Moreover, this enables smoother plug and play deployment at the operator site. The working of the scheme is demonstrated by several experiments conducted for a DP-16QAM 200 Gbit/s signal and DP-64QAM 400 Gbit/s signal over several link distances from 95 km to 1520 km.

5.5 Accurate estimation of transmitter I/Q skew with a phase noise canceler

Before we dive into the working of the phase noise canceler which was introduced in Section 4.7, we should talk about the motivation behind implementing this block in practice. With systems migrating from DP-16QAM 200 GBit/s to DP-16QAM 400 Gbit/s and DP-64QAM 600 Gbit/s [74–76]. We know from the earlier section Section 3.5.2 that an uncompensated transmitter I/Q skew can lead to several penalties, which increase rapidly for higher order modulation formats. As the industry moves towards the commercial deployment of single carrier DP-64QAM 600 Gbit/s, the estimation and compensation of the transmitter I/Q skew and the related 3-dB bandwidth effect becomes even more critical [77]. The urgency to come up with an accurate DPC block can be readily seen in Figure 5.20. The plot shows the OSNR penalty incurred by the system at the FEC threshold of $4.2 \cdot 10^{-2}$ for DP-16QAM at 63 GBaud (a net bit rate of 400Gbit/s) and DP-64QAM at 63 GBaud (a net bit rate of 600Gbit/s) transmitter. A mere skew of 0.5 ps for the DP-64QAM compels a 2 dB higher ROSNR in comparison to a system without any actual I/Q skew. The issue only becomes crucial at a skew of 2.5 ps for the DP-16QAM system. Nonetheless, such a deterioration from skew could not be tolerated and should be overcome by a powerful compensation algorithm. The results presented in this section are based on the publication [35].

One cause of the inaccurate estimation is attributed to the phase noise generated by the LASERs used in the transponders. This analysis was covered in Section 4.7. For the sake of a review, the plot comparing the skew estimation performance of two different LASERs is shown here again in Figure 5.21. Note that these measurements were done for a DP-64QAM 63 GBaud signal and data was collected for 70 transmitter I/Q skew estimates obtained from the DPC coefficients. Looking at the figure, it can be concluded that to some extend the quality of estimation is dependent on the LLW. The standard deviation of the estimates is lesser in the case of LASER with 50 kHz linewidth and it increases for the case with 150 kHz LASER.

We also see from the curves that worst case estimate for the red curve (150 kHz linewidth) is further from the mean by ~ 0.3 ps. Even though such an absolute value is quite small, an error of 0.3 ps from the absolute transmitter skew value will lead to an OSNR penalty of ~ 1 dB for DP-64QAM system, as seen in Figure 5.20. In order to reduce the occurrence of such estimates it is imperative to further enhance the accuracy of the estimation
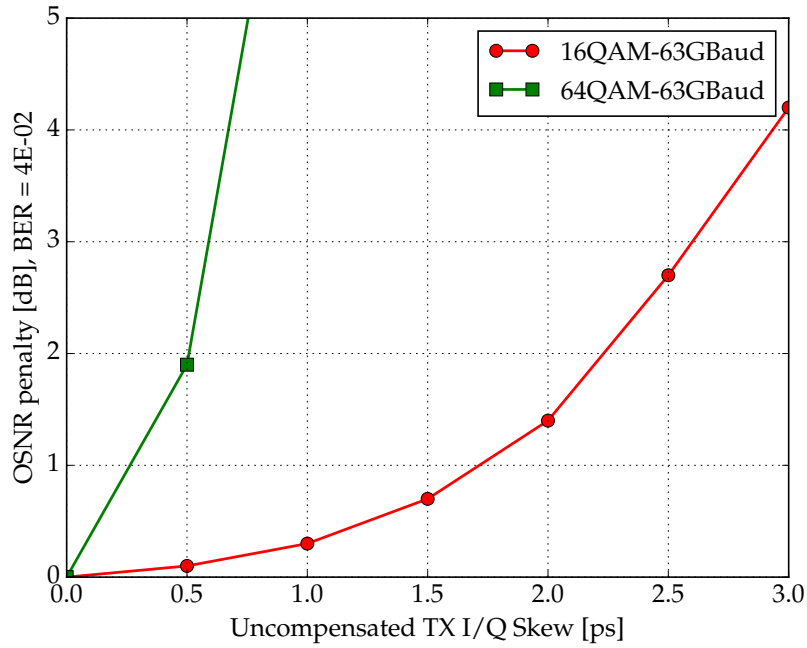
Figure 5.20: ROSNR penalty arising due to uncompensated transmitter I/Q skew
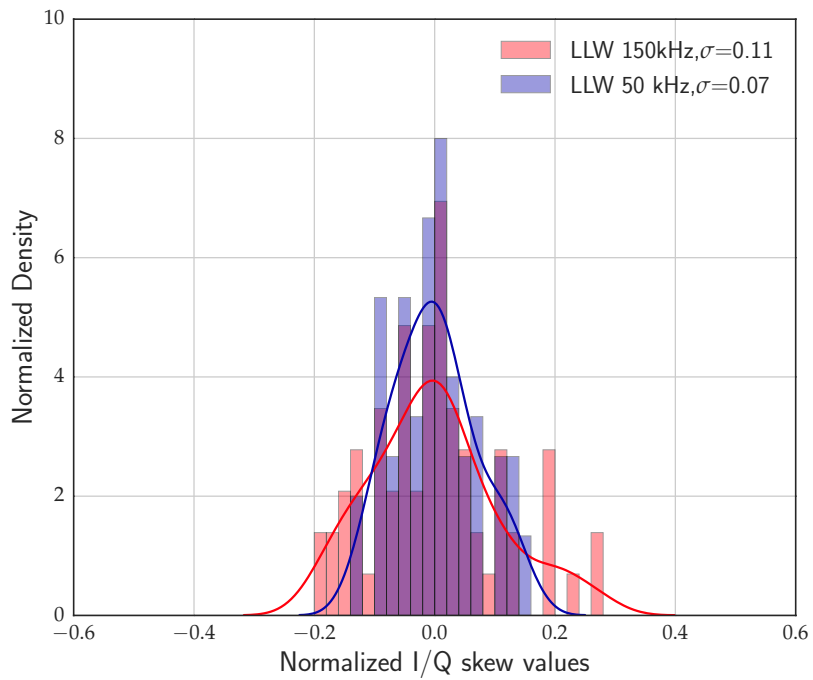

Figure 5.21: Transmitter I/Q skew estimation for two LASERs

of the proposed DPC scheme. This led to the development of a phase noise canceler (PNC) block which estimates and diminishes the effects of LASER phase noise and expedites a finer estimation of the transmitter I/Q skew by leveraging a better estimation of the DPC coefficients.

5.5.1 Experimental Setup

Figure 5.22 illustrates the experimental setup used to propose the working of PNC with DPC. In contrast to previous transmitter and receiver components, a four channel DAC with 3-dB bandwidth 32 GHz and sampling rate 100 Gs/s is used. The DA and DP-MZM are driven in the linear regime and have a respective 3-dB bandwidth of 40 GHz.

At the receiver, the optical signals are coherently demodulated using intradyne detection. A 4-channel oscilloscope with a 3-dB bandwidth of 35 GHz is used to capture shots of 34000 samples of each tributary at 80 Gs/s.

DP-16QAM and DP-64QAM signals at 63 GBaud and Nyquist roll-off 0.2 are uploaded to the DAC and sent over the back-to-back setup and transmitter I/Q skew estimates with and without PNC are evaluated and recorded.

In the case without PNC, the PNC is simply set to identity so that $\hat{y}_i[n] = y_i[n]$ and then DPC is performed. In the case with PNC the initial estimates for the channel matrix, $\hat{C}$ and transmitter I/Q skew, $\hat{\tau}$ are obtained from the digital de-multiplexing block and DPC block respectively. These estimates are then used to estimate and compensate the phase noise in the phase noise canceller according to steps mentioned in Section 4.7. Once the phase noise is compensated, the PNC block can forward the signals $\mathbf{y}$ free from phase noise to the digital de-multiplexing block which then successively provides cleaner signals to the DPC block. In the next iteration with the phase noise compensated signals DPC can then provide a better estimated of the transmitter I/Q skew. We will now go through the experimental results.

5.5.2 Experimental Results

75 independent DPC measurements were carried out for the case with and without PNC for both DP-16QAM and DP-64QAM using two LASERs with LLW 50kHz and 150kHz. Experimental results for the DP-64QAM 600 Gbit/s are discussed here. After calculating the transmitter I/Q skew values from the DPC coefficients, a histogram is plotted and a density estimate is obtained. To assess the gain obtained from PNC, a figure of merit is
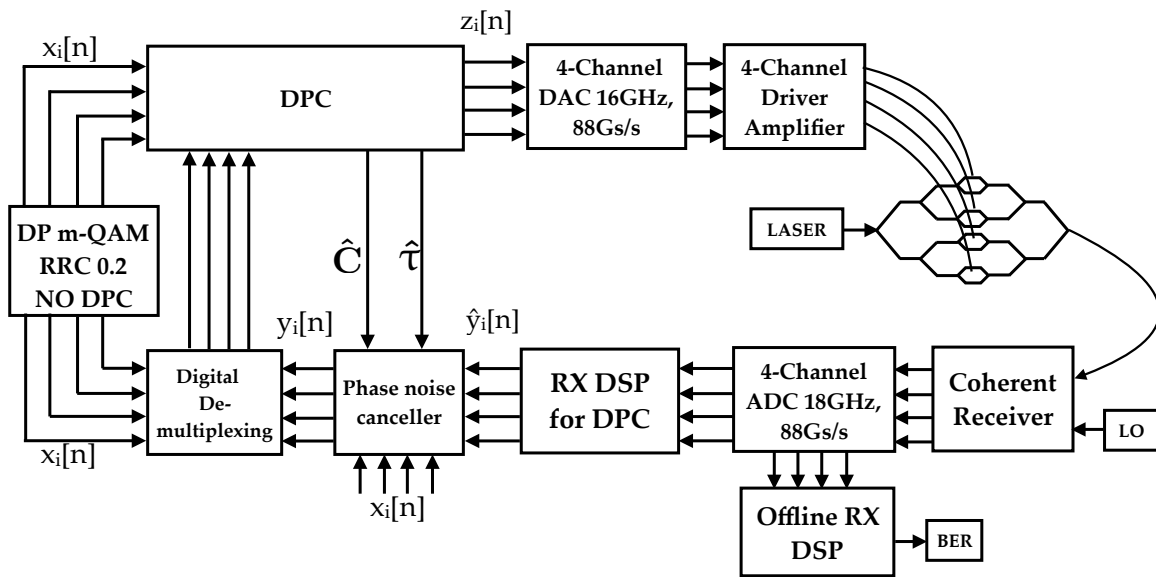
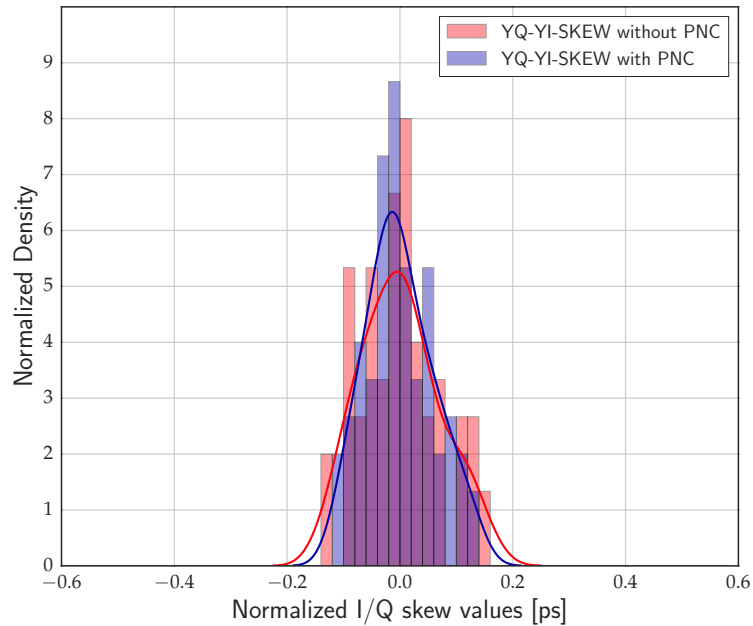Figure 5.22: Experiment setup with phase noise canceler

Figure 5.23: Density of estimated transmitter I/Q skew values for LASER with LLW 50 kHz
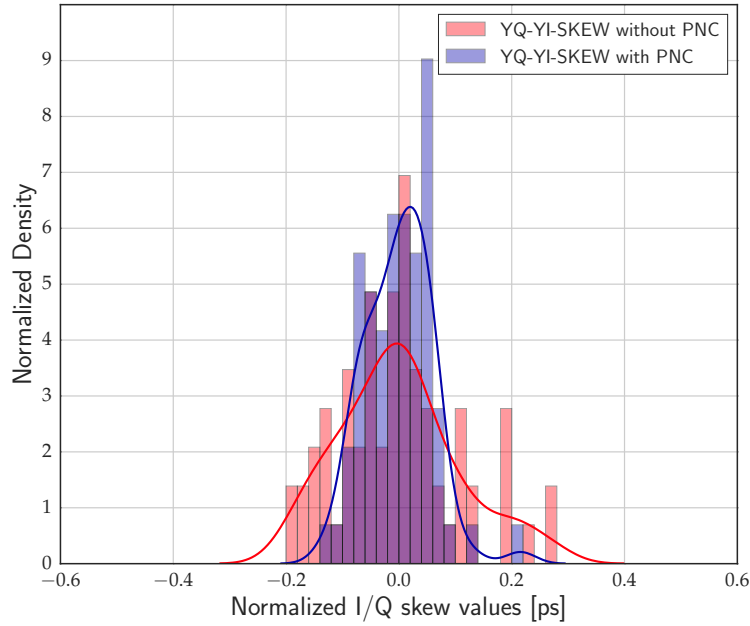
Figure 5.24: Density of estimated transmitter I/Q skew values for LASER with LLW 150 kHz

defined as $P(\tau_{err} > 0.2\text{ ps})$ which is the probability that the estimated skew value is more than 0.2 ps away from the true skew value. Hence, the lower the $P(\tau_{err} > 0.2\text{ ps})$ value, the more reliable is the skew evaluation method.

Figure 5.23 and Figure 5.24 show the histograms (bin size = 0.05 ps) of normalized transmitter I/Q skew estimates for the Y polarization with and without PNC for two different lasers respectively. The normalized values are obtained by subtracting the mean of the 75 estimates from each of the estimated value. Moreover, the corresponding density estimates are shown as solid lines in the figures. In both the cases, PNC brings a gain, by reducing the standard deviation of the estimated values. The gain is however more pronounced when a cost effective LASER with LLW 150 kHz and hence a higher phase noise is used.

$P(\tau_{err} > 0.2\text{ ps})$ can be calculated as the area under the curve from the probability density estimates. From Figure 5.23, $P(\tau_{err} > 0.2\text{ ps})$ is calculated as 0.25% for measurements done without PN and 0.005% when PNC is used. This reduction in $P(\tau_{err} > 0.2\text{ ps})$ is more appreciable in Figure 5.24, where $P(\tau_{err} > 0.2\text{ ps})$ reduces from 9.0% to almost 0.98%.

5.5.3 Summary

Higher order modulation formats such as DP-64QAM at high baud rates of 64 GBaud are extremely sensitive to residual transmitter I/Q skew. It is shown that a skew of 0.5 ps can lead to a 2 dB penalty in ROSNR for a 600 Gbit/s system. In addition to this, LASER phase noise hampers the estimation of transmitter I/Q skew when implemented in the scheme of the proposed DPC algorithm.

In order to improve the accuracy of the transmitter skew estimates, a PNC is introduced before the DPC block. The PNC block 2nd order digital PLL and it's complete illustration is explained in Section 4.7. A significant improvement in the accuracy of the skew values is demonstrated for LASERs with LLW 50 kHz and 150 kHz which is also quantified with a figure of merit. The suggested PNC scheme provides a robust addition to the DPC block leading to an accurate estimation of transmitter I/Q skew 99.995% of the time. It also facilitates the use of cost-effective LASERs for DPC and skew estimation.

6

Transmission Experiments and Field Trials

In the process of development of the DPC algorithm, various transmission experiments and field trials were conducted to showcase the gain obtained in transmission on using the developed algorithm. Following transmission experiments will be discussed in this section:

- 400 Gbit/s single carrier transmission in 50 GHz grid

- WDM transmission of DP-64QAM 300 Gbit/s under highly non-linear transmitter conditions

6.1 400 Gbit/s single carrier transmission in 50 GHz grid

In the past years, there has been an intensive research to realize spectrally efficient and cost-effective 400 G optical communication systems. The combination of higher order modulation formats, transmitter side DPC and sophisticated FEC lay down the foundations for the future 400 G systems. DP-16QAM at 63 GBaud was considered as a rising candidate for next generation 400 G transponder [78]. While DP-16QAM with 400 Gbit/s offers an advantage when it comes to transmission distance, it also requires a larger filter grid of $\sim$ 75 GHz, with a baud rate of 63 GBaud at a 0.2 roll-off .

In comparison to DP-16QAM, DP-64QAM and DP-128QAM were considered as potential candidates in research owing to the higher spectral efficiency provided by these modula-

tion formats. In addition to the spectral efficiency advantage, these formats also require a lower baud rate, hence relaxing the bandwidth requirements on state-of-the-art transmitter technologies with sampling rate 88 Gs/s and 16 GHz 3-dB bandwidth [30, 79].

In relation to DP-64QAM and DP-128QAM transmission experiments, various experiments have been performed [13, 80–82]. In particular, in [82], the authors demonstrate a DP-128QAM signal with a 140 Gbit/s line rate as a more spectrally efficient alternative to DP-QPSK 100G systems In [81], the generation of a 515 Gbit/s DP-128QAM superchannel with 8 sub-bands and its transmission over 155 km SSMF is presented.

In this transmission experiment, the feasibility of implementing DP-64QAM and DP-128QAM at 400Gbit/s net data rate with state-of-the-art transmitter technology is investigated. For this purpose, a DP-64QAM signal with baud rate 45.25 GBaud and a DP-128QAM signal with baud rate 40.69 GBaud are generated. These baud rates are chosen in order to obtain a net data rate of 400 Gbits, with the consideration of a FEC overhead of 25% for DP-64QAM and 30% for DP-128QAM, an optical transport network (OTN) overhead of 4.7% and a DSP overhead of 3.0% for the pilot tones and training sequences. Moreover, these modulation formats enable transmission in 50 GHz grid.

Since the generation of such high baud rates is severely limited by the linear and non-linear effects of the DAC, DA and DP-MZM, the DPC algorithm developed in the thesis is used to compensate for the various transmitter limitations.

6.1.1 Experiment Setup

The experiment setup consists of two steps :

- An optical back-to-back setup is used to generate the samples with DPC

- A transmission setup for comparison of single carrier DP-128QAM and DP-64QAM 400 Gbit/s with different fiber types

Transmitter DSP : DPC for DP-64QAM and DP-128QAM 400 Gbit/s

The same setup as shown in Figure 5.6 is used for generation of DPC samples for DP-128 QAM samples with 40.69 GBaud and for DP-64QAM samples with 45.25 GBaud. The following memory polynomial model is adopted to compensate for the bandwidth limitation, transmitter I/Q skew and other non-linear effects for both the modulation formats:

$$z_i[n] = \sum_{m=-16}^{16} h_{i,m} y_i[n-m] + \sum_{m=-2}^{2} h_{i,m,p} y_i[n-m] + h_{i,0,3} x_i^3[n] + h_{i,0,4} x_i^4[n] \qquad (6.1)$$

Once the respective samples are generated, performance is characterized with back-to-back BER vs OSNR curves and significant gains are reported for the case with and without DPC, emphasizing the need for DPC for generation of the signals.

Transmission over LA-PSCF and SSMF

Transmitter

The experiment setup used for transmission is shown in Figure 6.1. The transmitter consists of a 4-channel DAC with 16 GHz bandwidth, sampling rate of 88 Gs/s and a ENOB of $\sim$ 6 [48]. The analog signals are then amplified with a linear DA and finally data is modulated on to the LASER using a DP-MZM. Root raised cosine pulses with roll-off 0.2 are generated for DP-64QAM and DP-128QAM at 45.25 GBaud and 40.69 GBaud respectively. The details of the transmit samples are mentioned in Table 6.1. After suitable DPC, the samples are uploaded on to the DACs.

Modulation Format	Baud Rate (GBaud)	FEC Overhead	Net Bit Rate (Gb/s)	FEC Threshold	Sp.Efficiency (bits/s/Hz)
DP-64QAM	45.25	25%	403	4.2E-02	8.2
DP-128QAM	40.69	30%	406	5.2E-02	7.1

Table 6.1: 400 Gbit/s single carrier configurations

Link

DP-64QAM and DP-128QAM are transmitted over two different fiber types, large area pure silica core fiber (LA-PSCF) and SSMF with the following link configurations :

- 4 spans of 82 km of Sumitomo LA-PSCF with 0.16 dB/km attenuation and 21 ps/(nm · km) CD [83] with a total reach of 328 km.

- 3 spans of 95 km of SSMF with 0.20 dB/km attenuation and 16 ps/(nm · km) CD amounting to a total link length of 285 km.

EDFAs with noise figure ~ 6 dB are employed to amplify the optical signal after each span. After suitable launch power optimization, digitally pre-compensated DP-64QAM and DP-128QAM signals are launched into both the fiber spans, where N stands for the respective number of fiber spans of SSMF and LA-PSCF (see Figure 6.1). After transmission, optical signal is filtered with an optical filter which additionally suppresses the amplified spontaneous emission (ASE) noise from the EDFAs. The center frequency of the filter is set at 193.4 THz with a bandwidth of 50 GHz. An additional noise loading is utilized to characterize the back-to-back performance of both the modulation formats.

Receiver

The receiver consists of the standard components as also previously explained. It consist of an optical coherent front-end, which demodulates the incoming optical signals with intradyne detection. Electrical signals are then converted to digital domain using a high sampling rate ADC with 18 GHz bandwidth, operating at 80 Gs/s which provides $5 \cdot 10^5$ samples for each tributary. The digital samples are then processed by the suitable functional blocks in the receiver DSP. Receiver DSP includes suitable resampling to two times the symbol rate, CD compensation with a frequency domain equalizer and CFO estimation and compensation [61]. After the data-aided equalization, carrier phase estimation is performed using the distributed pilot symbols, followed by soft demapping and decoding. Finally, BER is estimated by error counting.

6.1.2 Experimental Results

The PSDs of DP-128 QAM signal at 40.96 GBaud are plotted in Figure 6.2. The figure shows the PSD of the input desired signal and spectrum of signals with and without DPC. While samples without DPC suffer from the 3-dB bandwidth limitation of the transmitter components, DPC mitigates this limitation and restores the desired flat top spectrum. Results for DP-64QAM at 45.25 GBaud follow the same pattern. The back-to-back BER vs OSNR performances with and without DPC for DP-128QAM and DP-64QAM are shown in Figure 6.3. The OSNR is measured with a 0.1 nm noise bandwidth. In addition to the experimental curves, the corresponding theoretical curves with the relative FEC thresholds are plotted. Both the modulation formats suffer from extremely large implementation penalties attributable to the various linear and non-linear effects present at the transmitter and receiver. In addition, generation of such higher order modulation formats is also hampered by the low ENOB of 5.5 of the DAC and ADC. This is observed in the higher error
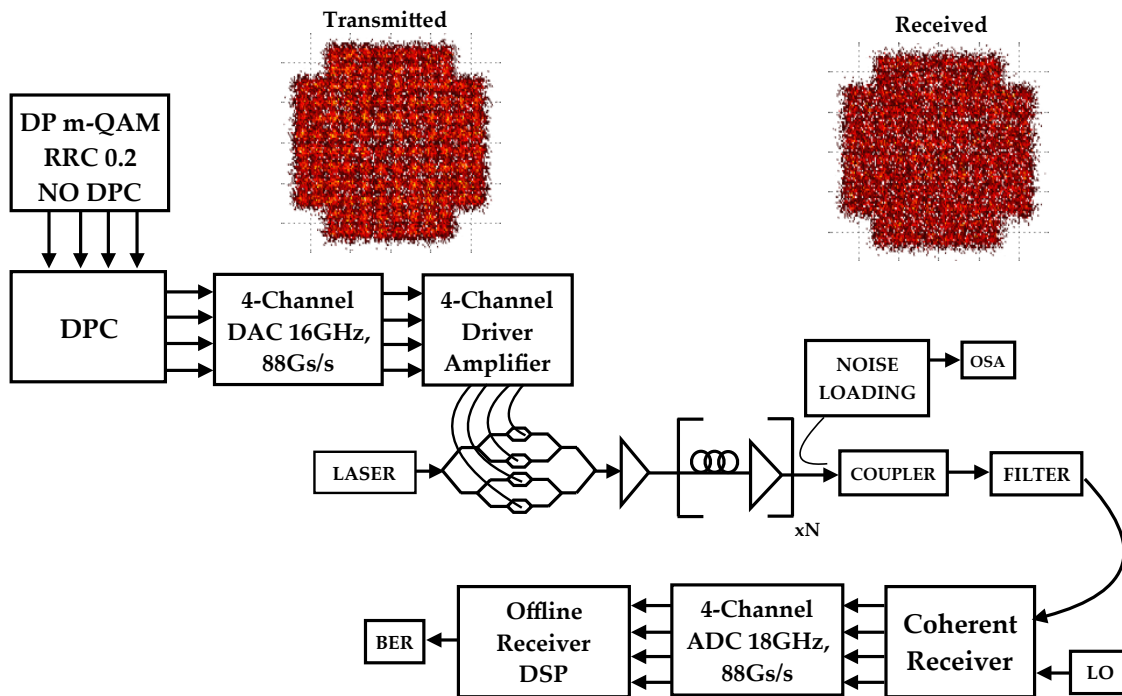
Figure 6.1: Experiment setup for single carrier 400 Gbit/s transmission

floors obtained for both the modulation formats at higher OSNR.

Demodulation and detection of DP-64QAM and DP-128QAM signals require a high OSNR at the receiver. From Figure 6.3, at FEC threshold, error-free detection of DP-64QAM signal is impossible when no DPC is applied, since the BER always lies above the FEC threshold. This, however is made possible by applying DPC to the signals resulting in a gain of more than 10 dB which is obtained at the 25% FEC threshold.

For DP-128QAM signals, a gain of 4.8 dB at 30% FEC is obtained from applying DPC. This gain in turn reduces the implementation penalty and relaxes the ROSNR value necessary for error-free detection at the FEC threshold. It is also noted that the gain obtained from DPC is higher for DP-64QAM. This is because of the benefit from DPC increases with increasing baud rate. In addition, generation DP-128 QAM is additionally hindered by the quantization noise, which can not be tackled by DPC.

For both modulation formats, the optimum launch power is determined by sweeping the launch power against BER. This is performed in order to operate the system in a linear regime and reduce the affect of non-linearities originating from the optical fiber. The launch power for each case is measured over 190 km of SSMF and 328 km of LA-PSCF for DP-128 QAM and over 285 km SSMF and 328 km of LA-PSCF for DP-64QAM. The launch
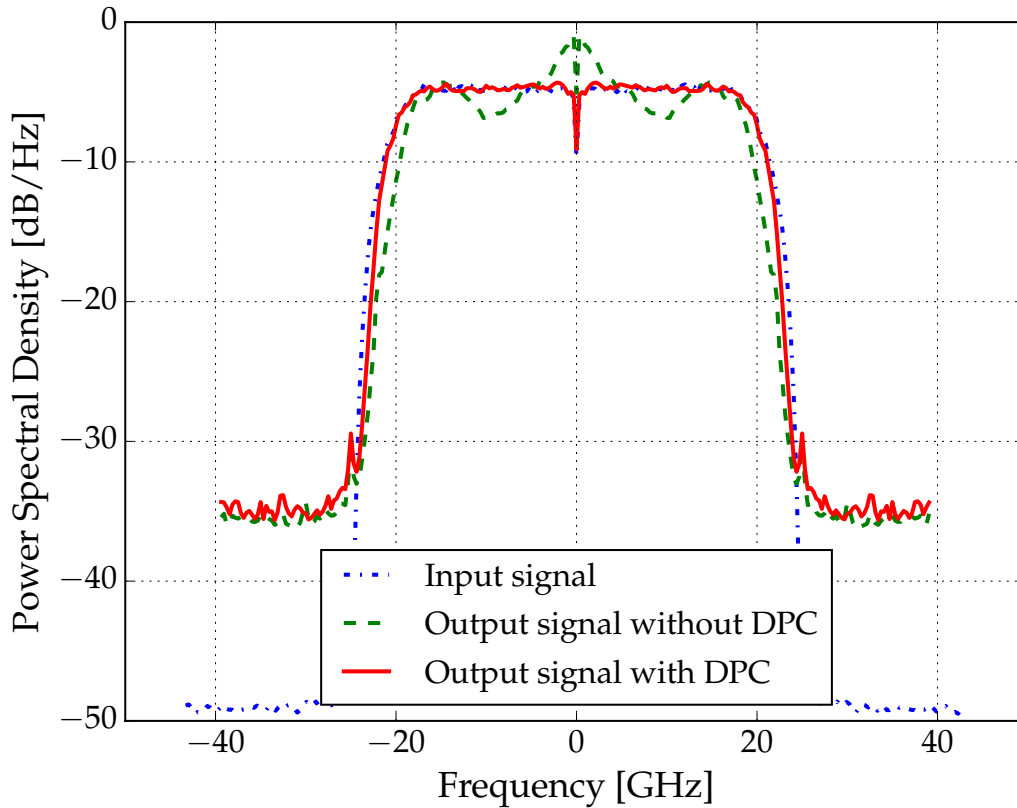
Figure 6.2: PSD for DP-128QAM at 40.69 GBaud

power is established after every EDFA at the input of each span input and the corresponding BER is measured at the end of the link. The corresponding launch power optimization curves are shown in Figure 6.4. The optimal launch power for DP-64QAM is observed to be higher than for DP-128QAM due to the higher baud rate of the signal. Additionally, it is seen that the transmission performance over LA-PSCF is better than over SSMF due to lower non-linearities and lower attenuation of the fiber.

Figure 6.5 shows the comparison of the overall transmission distance for error-free detection for DP-64 QAM and DP-128 QAM. Over SSMF, DP-128 QAM and DP-64 QAM formats can be transmitted over 190 km and 285 km respectively. The transmission distance increases when signals are transmitted over LA-PSCF, which is clear from the slopes of the curves.
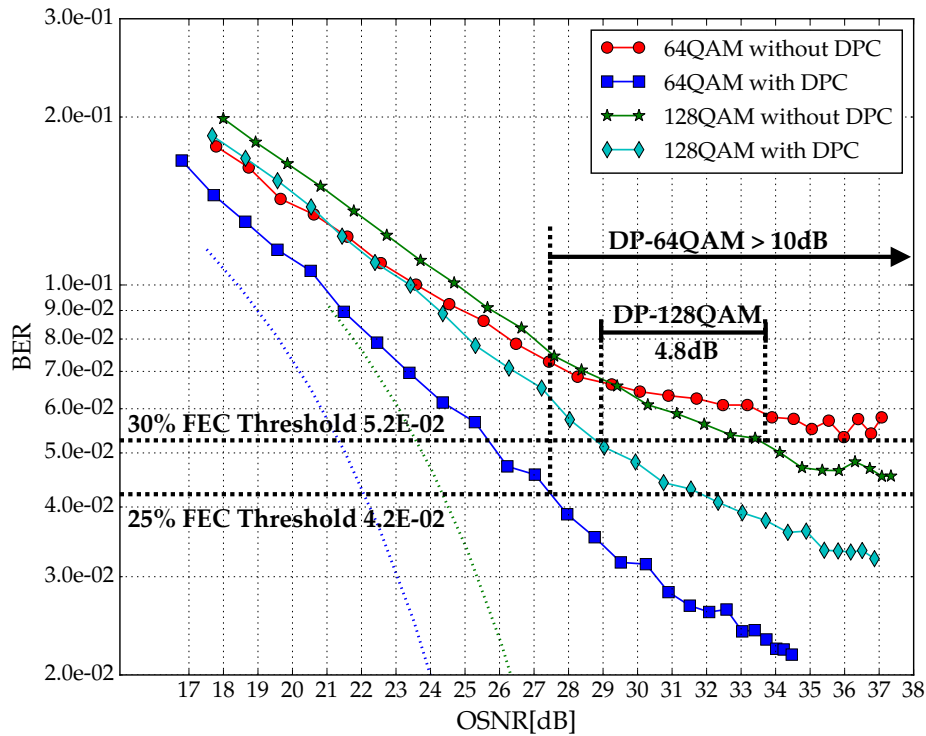
Figure 6.3: BER vs OSNR performance for DP-64QAM and DP-128QAM with and without DPC

6.1.3 Summary

In this subsection, experimental transmission of single carrier 400Gbit/s using commercial state-of-the-art transmitter and receiver components is demonstrated with an effective bandwidth of < 16 GHz.

Given the low bandwidth of state-of-the-art commercial transmitter components, the generation of high baud rate signals such as DP-64QAM at 45.25 GBaud and DP-128QAM at 40.69 GBaud is quite challenging. The proposed adaptive DPC algorithm is used to overcome the bandwidth limitation, transmitter I/Q skew mitigation and non-linear effects through the use of additional non-linear taps in the memory polynomial mode. Substantial gain of more than 4.8 dB is observed for DP-128QAM. In case of DP-64QAM it is ascertained that the transmission is only possible when DPC is executed. Both modulation formats, DP-128QAM and DP-64QAM are able to achieve a distance of 190 km and 285 km with SSMF, which are typical distances for metro and inter data center interconnects (DCI). In terms of spectral efficiency, DP-128QAM with 8.2bit/s/Hz beats DP-64QAM with 7.2bit/s/Hz. An
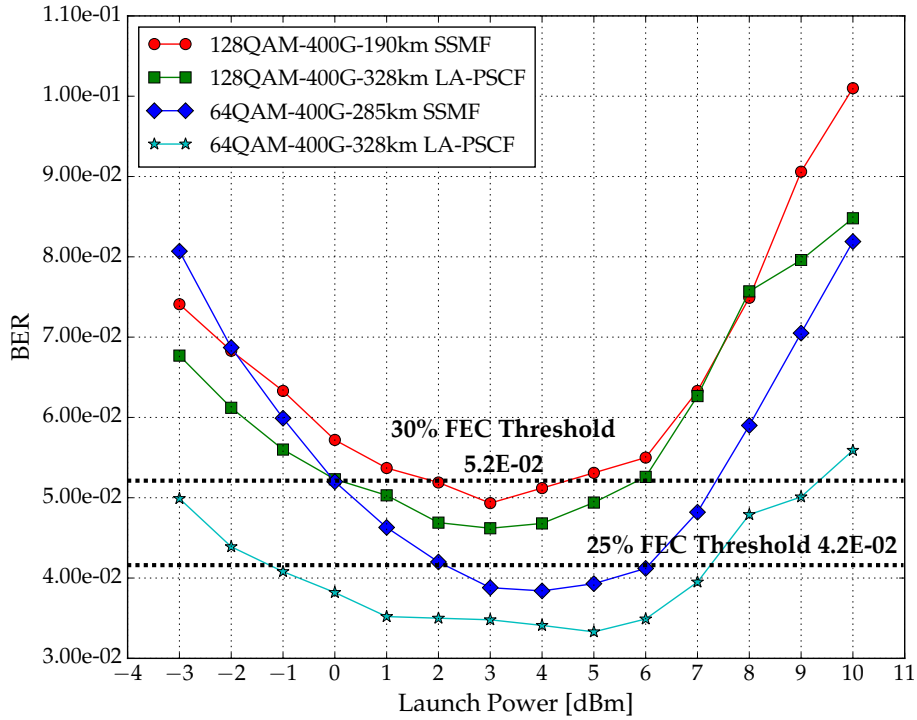
Figure 6.4: Launch power optimization for DP-64QAM and DP-128QAM over various distances and fiber types

extra advantage of DP-128QAM is it's potential to fit in a 50 GHz grid with its narrower spectrum, and an easier upgrade to the high bit-rate legacy systems.

6.2 300 Gbit/s DP-64QAM WDM transmission with highly non-linear transmitter

Conventionally, optical transmitters are operated in their linear regime. Linear operation of the transmitter is obtained by controlling the amplitude of the input digital signal and the gain of the driver amplifier. The digital input signal is optimized by establishing a trade-off between errors introduced due to clipping and utilizing the complete digital to analog range of the DAC. The driver amplifier is as well operated in the linear regime and the gain of the driver amplifier is adjusted to avoid any non-linearities from the DP-MZM. While such a linear operation results in a low BER, it is however, not very efficient and leads to low transmit output power and low OSNR at the transmitter.
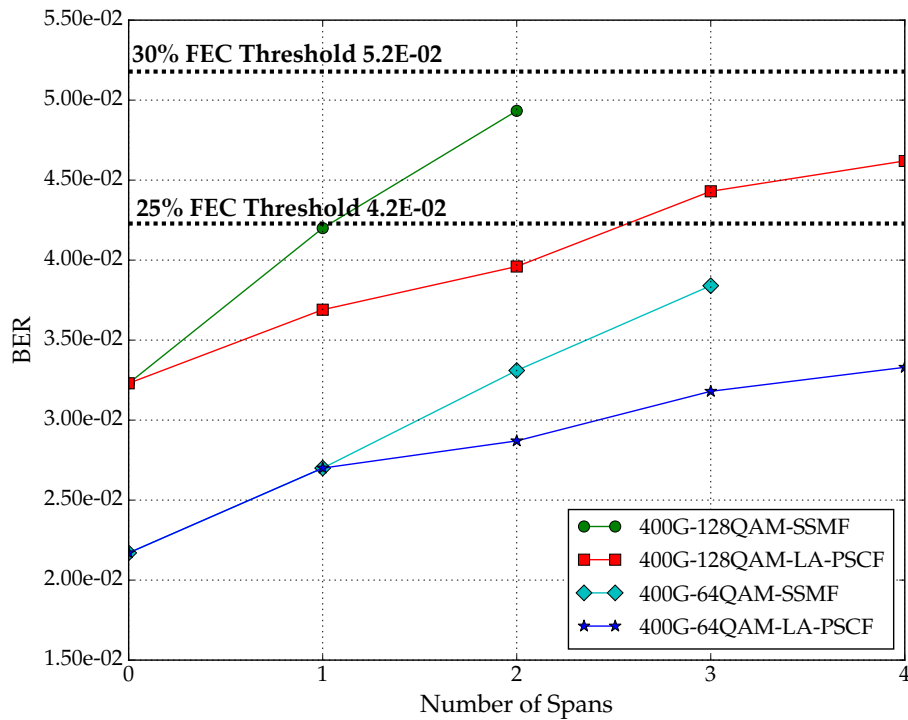
Figure 6.5: Performance vs number of spans for transmission

Particularly in WDM systems which suffer from additional filter losses, the quality of transmit signal and OSNR deteriorate before the signal even reaches the first booster amplifier, hence, necessitating the use of per channel EDFAs. In this work, feasibility of carrying out a DP-64QAM 300 Gbit/s WDM transmission with highly non-linear transmitters is analyzed. The impact of additional non-linear penalties incurred is mitigated using the DPC scheme.

6.2.1 Experimental Setup

The experimental setup consists of the following two parts:

- An optical back-to-back configuration is used to generate the appropriate DPC signal with the DPD part to alleviate the non-linear effects

- A DP-64QAM 34 GBaud WDM transmission setup with 31 neighboring channels

DPC with non-linear compensation for DP-64QAM 34 GBaud

The optical back-to-back setup is the same one as used in the previous section, explained in Figure 5.6. To account for the additional transmitter non-linear effects, the following memory polynomial model with higher order non-linear taps is adopted. The model consists of a 31 taps for compensation of linear effects and extra non-linear taps of order 3 and 5 with memory.

$$z_i[n] = \sum_{m=-15}^{15} h_{i,m,p} y_i[n-m] + \sum_{-5}^{5} h_{i,l,3} x_i^3[n-l] + h_{i,l,5} x_i^5[n-l] \qquad (6.2)$$

After generation of the individual coefficients, DP-64QAM 34 GBaud signals with DPC are obtained and uploaded on to the transmitter for transmission over SSMF.

31 channel DP-64QAM 300 Gbit/s WDM transmission

Transmitter

The WDM transmission experiment setup is shown in Figure 6.6. In real systems, each WDM signal is modulated independently using individual transmitter for each channel. However, for experimental and demonstration purposes, a WDM signal is generated by using two independent transmitter setups and using decorrelation of neighboring channels which are then added to the channel under test (CUT). As shown, the experimental setup consists of two transmitters, one for the CUT and the other for the generation of neighboring channels. Both the transmitters consists of a 4 channel DAC, a DA and a DP-MZM, with the same parameters as mentioned in Section 6.1.1. A LASER box is employed at the neighboring channel setup. The neighboring channel setup produces 30 channels modulated with DP-64QAM at 34 GBaud with Nyquist pulse shaping and roll-off value of 0.2.

In order to de-correlate the channels, a wavelength selective switch (WSS) is employed, in which each signal is delayed by employing fibers of different lengths from 1 m to 8 m. The CUT is independently produced by the other setup and multiplexed with the neighbor channels in the WSS and launched into the SSMF. Before multiplexing, the channels are individually amplified. This was done to ensure enough power entering the fiber, for the sake of doing launch power optimization.
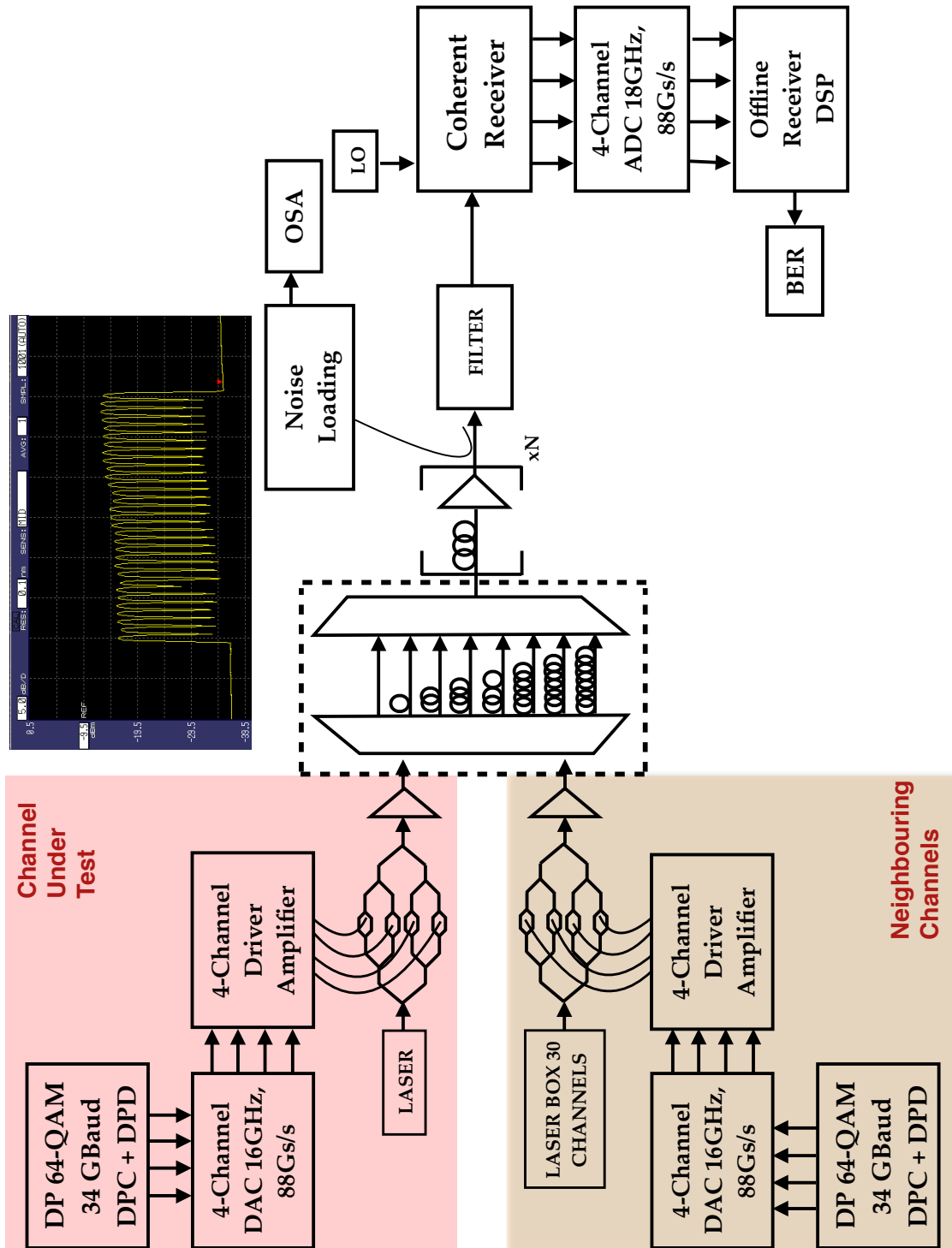
Figure 6.6: Experimental setup for DP-64QAM 300 Gbit/s WDM transmission
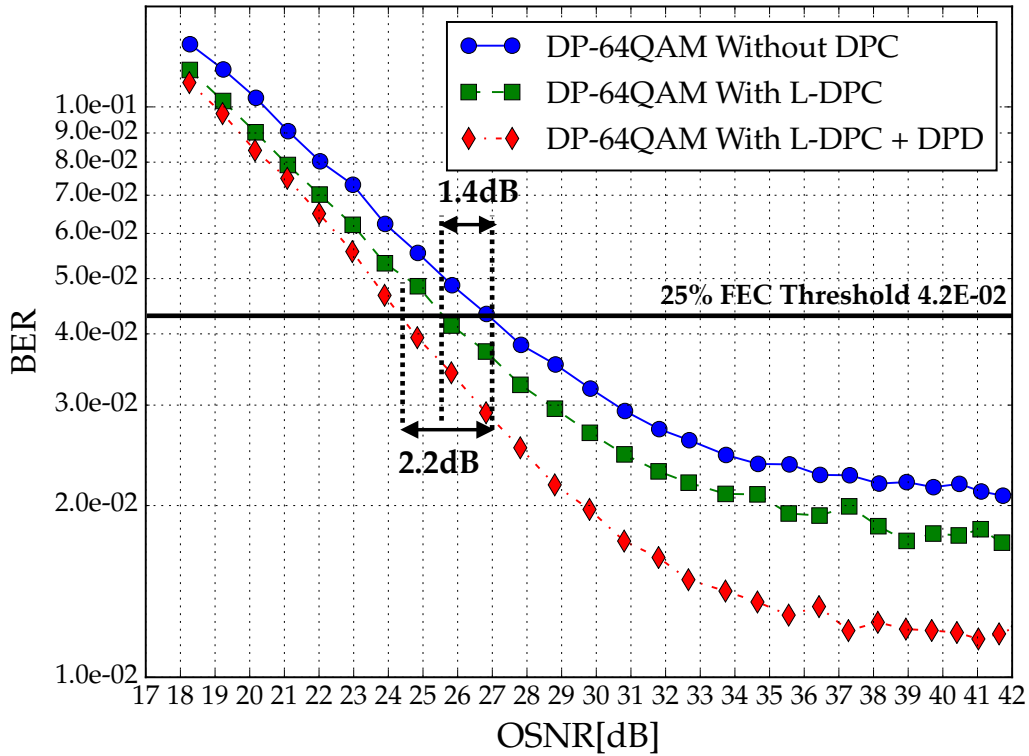
Figure 6.7: BER vs OSNR showing gains obtained from non-linearity mitigation

Link

The link consists of 4 spans of SSMF with 0.2dB/km attenuation and 16.9 ps/nm/km of CD. Similar to the previous experiment, EDFAs with 6 dB noise figure are used to amplify the optical signals after every span and compensate the span loss.

Receiver

In typical WDM systems, each channel is independently filtered, demodulated and decoded using individual receivers. In this case, a filter was employed at the end of the link, to filter out the CUT at 193.4 THz and with a bandwidth of 60 GHz. The filtered CUT is then demodulated using a LO tuned at the carrier frequency.

Demodulation is followed by analog to digital conversion with a high sampling rate ADC, which gives $5 \cdot 10^5$ samples for each tributary at 80 Gs/s. Offline processing of the samples is then performed as mentioned in the receiver of Section 6.1.1.

6.2.2 Experimental Results

The back-to-back BER vs OSNR curves for DP-64QAM 34 GBaud system with net 300 Gbit/s are shown in Figure 6.7. A comparison of the performance sensitivity for three different system configurations :

- DP-64QAM without DPC but with manual transmitter I/Q skew compensation

- DP-64QAM with linear DPC

- DP-64QAM with linear DPC and DPD with additional mitigation of transmitter non-linearities

is shown in the figure. The ROSNR is analysed at a 25% FEC threshold of 4.2×10^{-2} . Driving optical transmitter in their non-linear region with higher order modulation formats such as DP-64QAM leads to a greater penalty, as also explained in Section 5.3. The trend is clear from the higher error floor present in all the cases.

The ROSNR however reduces by 1.4 dB at FEC threshold when linear DPC is executed. There is a further improvement by 0.8 dB when the effects of non-linearities from the driver amplifier and DP-MZM are further lessened after applying non-linear DPD.

The benefit in ROSNR obtained from non-linearity mitigation is translated into transmission reach, which is seen in Figure 6.8. Launch power is optimized with neighbor channels and optimized such that the launch power for each fiber span is -0.5 dBm. After launch power optimization, WDM signals are sent into the fiber spans. At the receiver, the CUT is filtered out, LO is tuned and BER is calculated after offline DSP

It is clear that signals without any linear and non-linear pre-compensation do not attain the transmission distance of 380 km. DP-64QAM with appropriate linear DPC and DPD is successfully transmitted and received error-free after 380 km of SSMF at -0.5dBm launch power.

6.2.3 Summary

When driven at higher gains, driver amplifiers and DP-MZM result into non-linearities which can hamper the transmission performance of higher order modulation formats. In this experiment, utilization of the automatic DPC scheme was presented to alleviate component non-linearites, enabling higher transmit output power, lower optical modulation loss and a potential to save the extra EDFA at the transponder. The proof was demonstrated
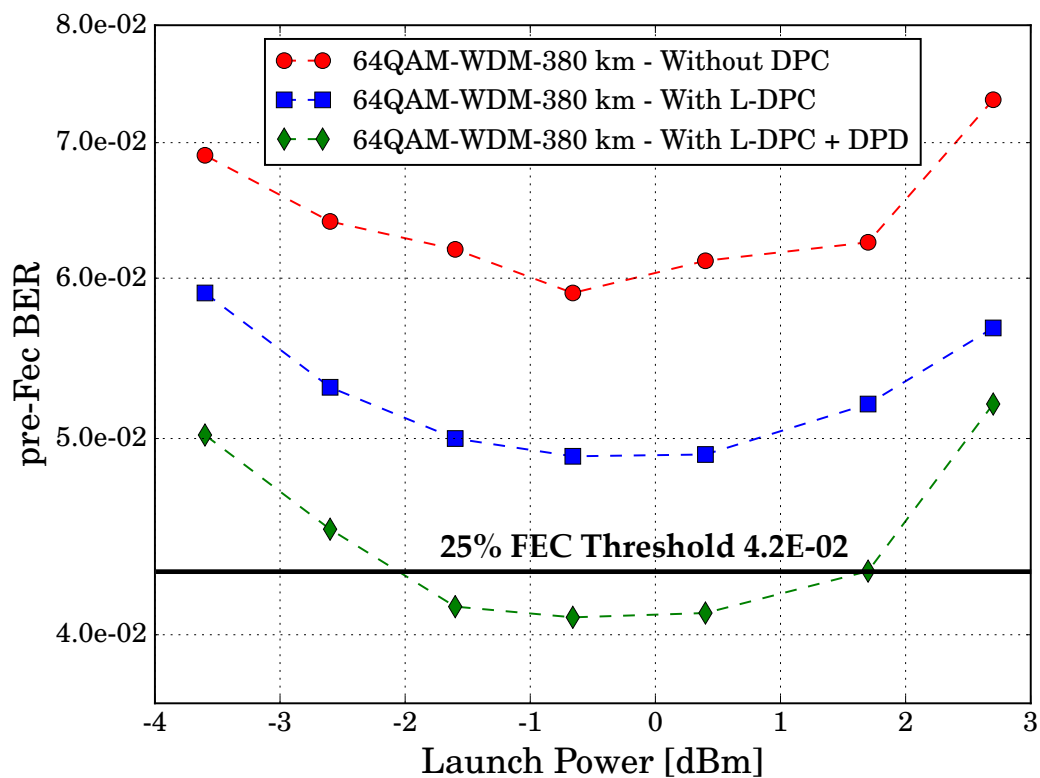
Figure 6.8: Launch power optimization for 300 G transmission

for a DP-64QAM 300 Gbit/s WDM system, where non-linearity compensation achieved a gain of 4 dB in optical modulation loss (seen in Section 5.3) and gain of 2.2 dB in ROSNR after transmission over 380 km of SSMF for a transmitter employed under highly non-linear conditions.

Field Trials

Coherent 100 G technology enjoyed an intense research phase, evaluation during field trials [84] and a successful commercial adoption [85]. This break from legacy on-off keying systems was the result of using modulation formats such as QPSK and cutting edge DSP combined with coherent optics. The commercial-grade success of 100 G is obviously followed by research in next generation 200 G, 400 G and 1 Tb/s technology.

In this regard, field trials become a crucial link in testing and evaluating future technologies on existing optical links. Such trials between vendors and operators enable a smoother transition and upgrade to next generation coherent systems. In the scope of the thesis and developed DPC algorithm, several field trials were conducted [31,33,37,86]. The DP-mQAM modulation formats digital signals were generated after utilizing the DPC coefficients, estimated by the ILA algorithm. An analysis of next generation coherent transponder technology was carried out in collaboration with Telecom Italia, where several higher order DP-mQAMs such as 4QAM, 8QAM, 16QAM, 64QAM and 128QAM at different baud rates were tried over different link configurations.

In this section, the following field trials are discussed :

- Comparison of single carrier 200 Gbit/s WDM transmission of DP-4QAM, 8QAM and 16QAM over 612 km SSMF.

- Single carrier 400 Gbit/s DP-64QAM and DP-128QAM WDM transmission over metro legacy links.

6.3 Field Trial: Comparison of single carrier 200 G WDM transmission of DP-4QAM, 8QAM and 16QAM

The exploration for suitable modulation formats for single carrier 200 G started as soon as coherent 100 G transponders were rolled out to the market. In this respect, field trials have been carried out showcasing the feasibility of single carrier 200 Gbit/s on deployed links in single and superchannel configurations [87, 88]. Single carrier DP-16QAM at 32 GBaud gained popularity due to its electronic bandwidth compatibility with state of the art DACs and ADCs. Other interesting candidates are DP-4QAM at baud rates > 55 GBaud and DP-8QAM at baud rates > 40 GBaud. Single carrier DP-4QAM at 200 G was demonstrated in [89]. Such high baud rates for DP-4QAM and DP-8QAM could only be made possible by applying strong DPC at the transmitter to overcome the hardware limitations and FEC to enable error-free transmission.

In this field trial, we draw exclusive comparisons between the three technological options : DP-4QAM, DP-8QAM and DP-16QAM, for power and cost efficient single carrier 200 G transponders in a WDM environment. Comparisons are drawn in terms of margin, spectral efficiency and reach. Results on the transmission performance for each modulation format are reported in a WDM scenario over 612 km of field deployed SSMF with EDFAs only.

6.3.1 Telecom Italia Link Description

The field trial was conducted on a link deployed with the Telecom Italia metro regional optical fiber network with G.652 standard single mode fiber [87]. The transmission link is shown in Figure 6.9. The transmitter and receiver were placed in Telecom Italia (TI) lab. The link consists of 8 spans of G.652 SSMF between Turin and Chivasso, with 22 dB insertion loss per span. A 2 km SSMF, with a loss of 4 dB, connects the transmitter site at Telecom Italia lab to the Telecom Italia Telephone Exchange (denoted as TI X in the figure). After loop-back from Chivasso for the 8 spans, another SSMF connects the output of the final span from the TI Telephone Exchange to the receiver, placed in TI lab. This makes an overall link length of 612 km. The high insertion losses in the fiber are attributed to the presence of various connector losses and are quite distinctive for deployed links in various metro areas.
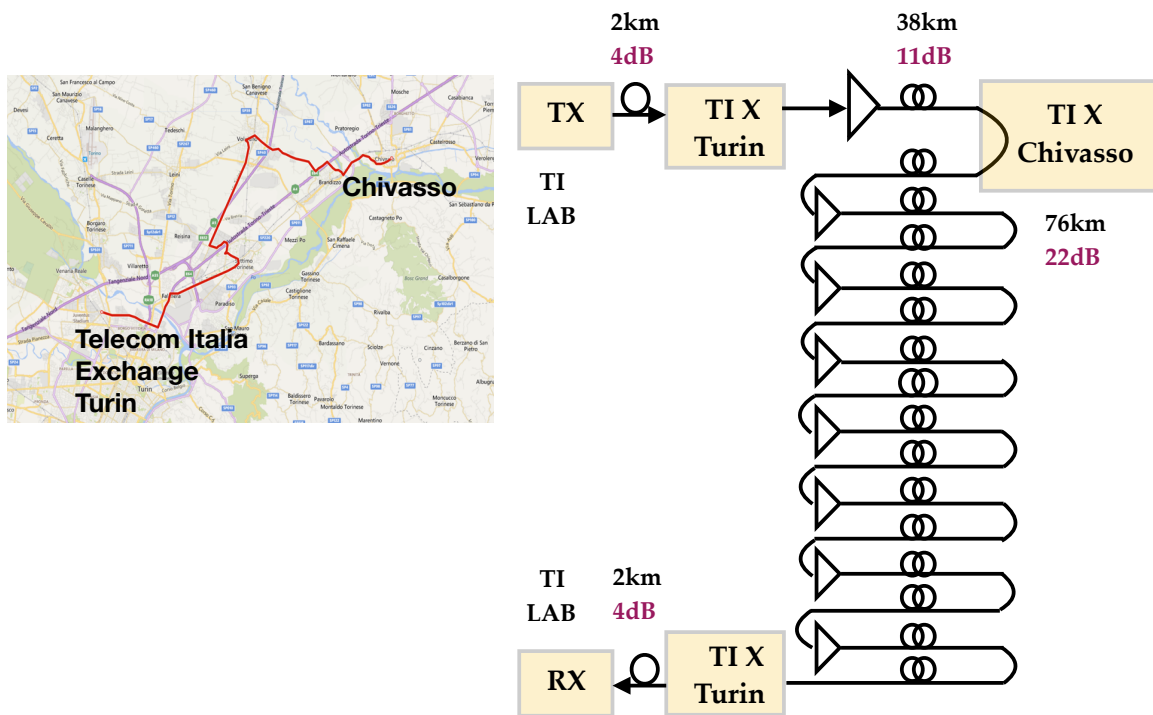
Figure 6.9: Telecom Italia link description

The link is capable of transmitting WDM signals with in-line amplification supported by EDFAs with noise figure of 6.5 dB. Optical per-channel power adjustment was carried out at the input of each span before proceeding with optical amplification with EDFAs. The total power of the WDM signal was supervised with the available remote power monitoring function of the amplifiers. The high span loss in the link itself results in challenging transmission conditions.

6.3.2 Transmitter

The complete configuration for the TI field trial is shown in Figure 6.10. It consists of 3 major parts :

- A 31 channel WDM transmitter

- TI link between Turin and Chivasso

- A coherent receiver

and additional SSMFs and EDFAs.
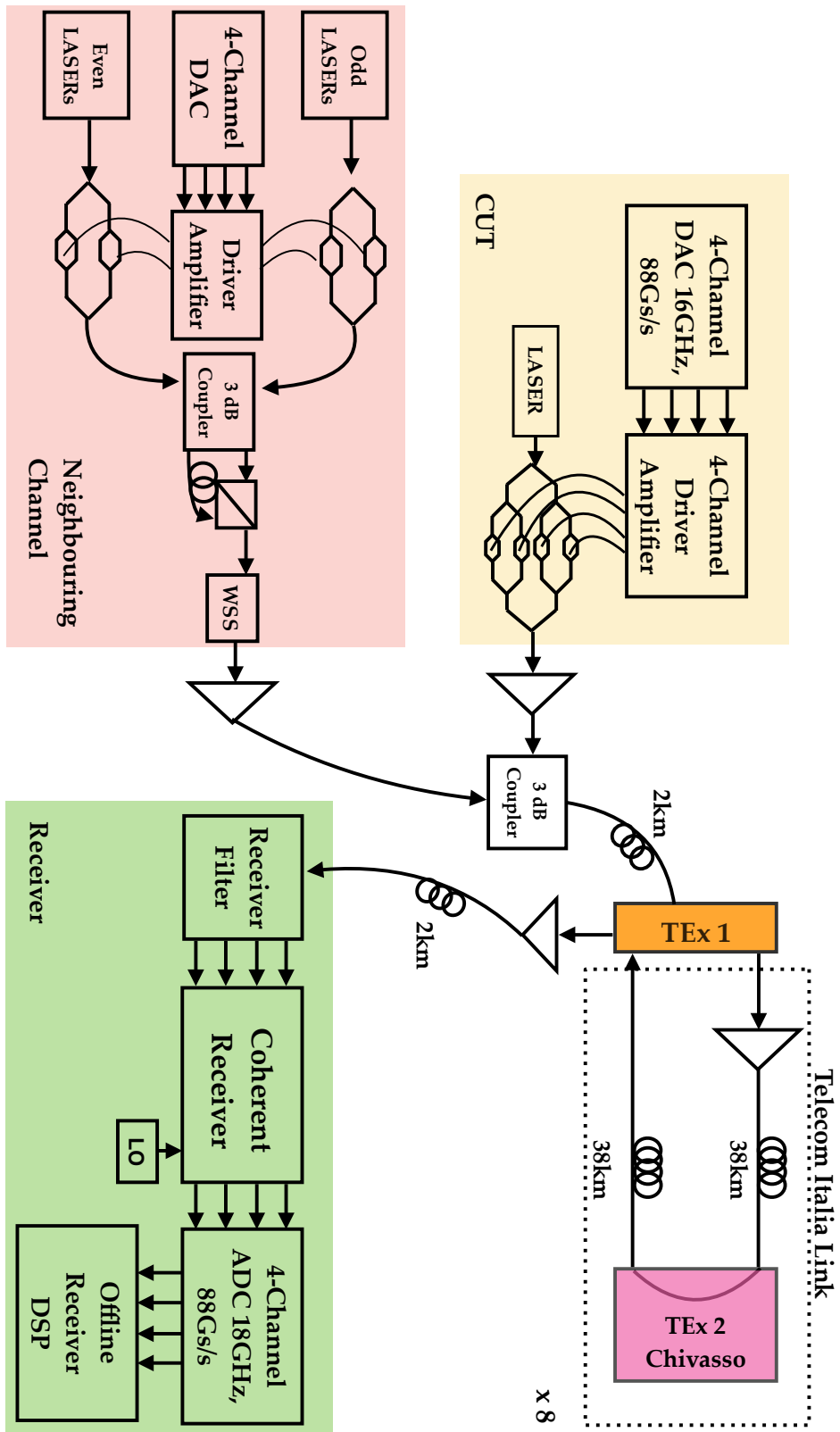
Figure 6.10: Experiment setup for Telecom Italia field trial with single carrier DP-4QAM, DP-8QAM and DP-16QAM.

The transmitter comprises of two independent transmitters, one for producing the CUT and the other for generating the 30 neighbor channels as pointed in Figure 6.10. Both the neighboring channel setup and CUT setup use identical DAC and driver amplifier. The DACs run with 88 Gs/s, and have a 3-dB bandwidth of 16 GHz [48]. Digital signals are amplified using driver amplifiers, which then drive the DP-MZM.

The neighbor channel setup consists of two separate LASER boxes, identified as *even* and *odd* LASERs with LLW of $\sim$ 50 kHz, feeding in to two separate single polarization I/Q MZMs. The separate *even* and *odd* channels are combined together with a 3-dB coupler. The two outputs of the 3-dB coupler are de-correlated by introducing a delay between the two and then combined in a PBC to generate pseudo polarization multiplexed signals. The resulting signals are then combined in a PBC, producing a dual-polarization WDM signal with 30 channels. A WSS is employed in the optical fiber path in order to suppress the CUT wavelength at 1550.116 nm. The resultant 30 channels are compounded with the CUT in a subsequent 3-dB coupler. The 31 channel WDM signal is then launched into the link section.

For the three transmission experiments, three modulation formats DP-4QAM, DP-8QAM and DP-16QAM with their respective system configurations are listed in Table 6.2. PRBS are generated and the FEC bits are added to the bit sequence. For the DP-4QAM case, a FEC overhead of 7%, for DP-8QAM, 15% FEC overhead and for DP-16QAM, 25% FEC overhead is utilized. The implemented soft-decision forward error correction (SD-FEC) codes were in-house developed. In addition, since data-aided DSP is executed, for all transmission experiments, a DSP overhead of 4% is considered and finally, the OTN overhead of 4.7% is employed too. After suitable mapping to the symbols, the digital signal is up-sampled two twice the symbol rate. RRC pulse shaping with the various roll-offs for each case is performed. The electrical generation of such high baud rates puts additional challenges to the transmission experiment. In order to overcome the transmitter's bandwidth limitation, I/Q skew and non-linear effects, suitable DPC is applied. The neighboring channels are produced likewise. After appropriate sampling to the DAC sampling rate, the samples for CUT and neighboring channels are uploaded to the corresponding DACs. After data modulation on to the carriers, the output of both the transmitters are optically coupled and launched into the link.

Modulation Format	Baud Rate (GBaud)	Roll-Off	Net Bit Rate (Gb/s)	FEC Overhead	WDM Spacing Used (GHz)
DP-4QAM	57.24	0.2	200	7%	68.75
DP-8QAM	42.0	0.2	200	15%	50.0
DP-16QAM	33.01	0.1	200	25%	37.5

Table 6.2: 200 Gbit/s single carrier configurations

6.3.3 Link Transmission

In deployed WDM links, each neighboring channel is generated by independent transponders. However, for the emulation of real effects, neighboring channels are produced by a different setup as described before and the CUT is multiplexed with the neighbor channels. Such a setup with 31 channels is used to emulate the non-linear effects of the fiber such as cross-phase modulation and four wave mixing. An analysis of the performance trend of the CUT was recorded by tuning the frequency of the CUT for different wavelengths and appropriately placing the neighboring channels around the CUT with the appropriate WDM channel spacing, as mentioned in Table 6.2.

The 31 WDM channels are optimized for their launch power, the results of which are discussed in this section . For each considered center frequency of the CUT, CD value is calculated and provided in the receiver DSP.

6.3.4 Receiver Processing

At the receiver, CUT is first filtered out by tuning the center frequency of the receiver filter. The filtered optical signal is demodulated using intra-dyne detection with a LO tuned to the transmitter LASER frequency. The electrical signals are converted to digital using an ADC at 80 Gs/s and a bandwidth of 23 GHz. The offline receiver DSP is then carried out as mentioned in Section 6.1.1 [37].

6.3.5 Field Trial Results

sec:fieldtrialresults

Before link transmission, back-to-back characterization for each modulation format was performed. This was followed by a launch power optimization in a WDM scenario. For all the investigated cases 30 neighbor channels around the CUT were undertaken. The following section discusses the back-to-back results and the launch power sweep for the

field trial.

200G DP-4QAM at 57.24 GBaud

The generation of single carrier DP-4QAM at 57.24 GBaud was the most challenging part of the field trial which is seen in the back-to-back BER vs OSNR results in Figure 6.11a. There is an implementation penalty of ~ 4 dB at the FEC threshold of 1.0E-02. To some degree, a high penalty was expected. This penalty is mainly due to the disproportion between the transmitter bandwidth of 16 GHz and the baud rate of 57.24 GBaud. Nonetheless, the strong DPC at the transmitter enabled the generation of a wide-band 57.24 GBaud signal. A high error-floor at 3E-04 is also noticed.

After performing the back-to-back BER vs OSNR characterization, the 31 channels with DP-4QAM 57.24 GBaud were multiplexed together and a launch power sweep was carried out for the WDM signal. The signals were arranged on the frequency grid with the center channel at 193.4 THz and the neighboring channels spaced 68.75 GHz apart which is sufficient filter bandwidth for the DP-4QAM signal with a total bandwidth of 68.68 GHz, accounting for the Nyquist roll-off of 0.2 For this purpose, launch power was regulated at the input of each span by adjusting the output power of the EDFAs. As seen in Figure 6.11b, for every 1 dB increase in launch power, the BER reduces and the corresponding OSNR increases. The points are the measured results, and the dotted line signifies an interpolation. The trend signifies the operation in the linear region of the system, where the system is still dominated by noise and not the non-linear effects. Due to the inability of the amplifiers to provide more power per channel, measurements beyond 5 dBm/channel could not be carried out. The launch power was then set at 5 dbm/channel. Successful transmission was obtained over a link length of 612 km with a large margin of 4.1 dB. This margin was determined by calculating the additional OSNR degradation which can be tolerated by the system before the BER reaches the FEC threshold.

200 G DP-8QAM at 42 GBaud

The next eligible candidate for single carrier 200 G transmission was DP-8QAM at 42 GBaud. For back-to-back characterization, only the CUT was considered. The BER vs OSNR results are shown in Figure 6.12a. The theory curve is also plotted. The DP-8QAM 200 G system has an implementation penalty of 2.3 dB. Note that, this penalty is even higher for signals without any DPC. As anticipated, signal deterioration due to the low bandwidth of the transmitter components is relatively lower than the DP-4QAM case. No error-floor is ob-

(a) BER vs OSNR

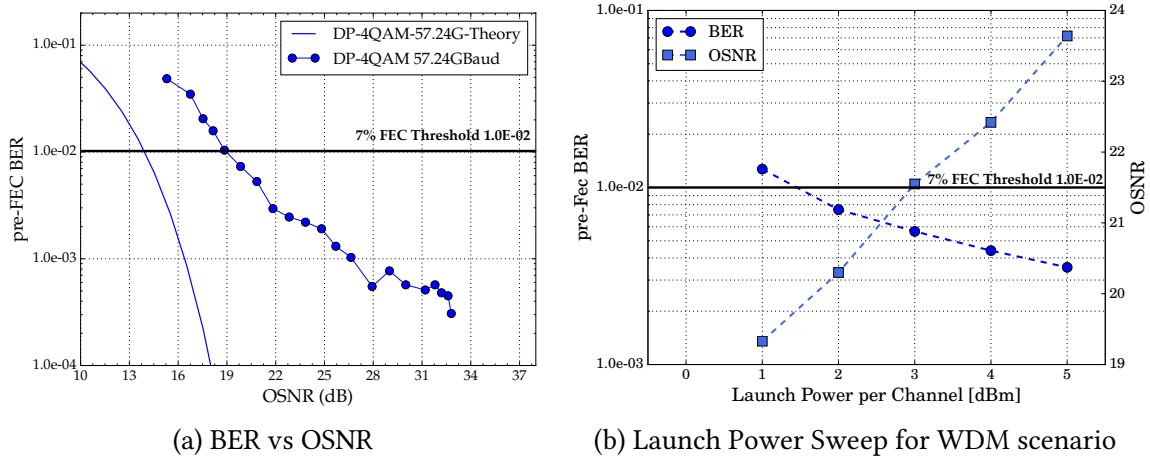(b) Launch Power Sweep for WDM scenario

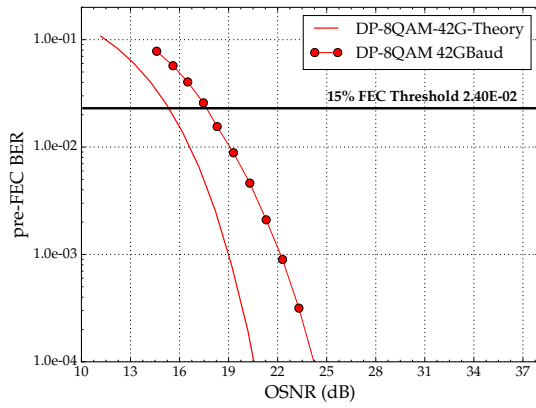Figure 6.11: Performance assessment of DP-4QAM 200 G

served within the measurement boundaries. For launch power sweep, 31 WDM channels were coupled together. With the CUT at 193.4 THz, channels were spaced at 50 GHz apart, ensuring sufficient filter bandwidth for a 42 GBaud signal with 0.2 Nyquist roll-off. The launch power was swept by controlling the output power of the EDFAs in the link. Results are plotted in Figure 6.12b. Up to a launch power of 3 dB/channel, the BER decreases, pointing to the noise dominated region of the system. For a launch power of 4 dBm/channel, a slight increase in BER is noticed, signifying the presence of light non-linearities due to higher launch power in the fiber. In order to limit the non-linear effects, the launch power was set at 3 dBm/channel. The DP-8QAM 200 G WDM signal was also successfully transported over the 612 km field trial link with a residual OSNR margin of 4.3 dB, marginally higher than the DP-4QAM counterpart.

200 G DP-16QAM at 33.01 GBaud

The third potential and the most preferred candidate for 200 G single carrier is DP-16QAM. Commercially, 200 G systems with DP-16QAM with 32 GBaud are available. In this field trial, another variant of DP-16 QAM was inquired. The baud-rate was set at 33.01 GBaud with a 0.1 Nyquist roll-off. Owing to its relatively lower channel spacing requirements, DP-16QAM 33.01 GBaud signal offers improvement in spectral efficiency and enables transmission of more WDM channels in the C-Band, thereby achieving a higher capacity.

For the DP-16QAM system, the back-to-back BER vs OSNR results are shown in Figure 6.13a, where an acceptable implementation penalty of 2.3 dB is noted. It is indeed interesting to observe the same penalty for both DP-8QAM and DP-16QAM. This is at-
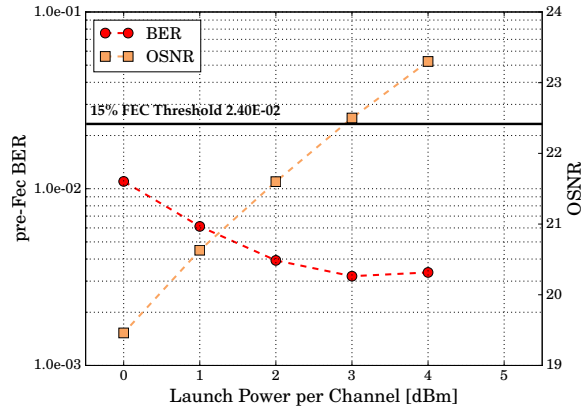
(a) BER vs OSNR

(b) Launch Power Sweep for WDM scenario

Figure 6.12: Performance assessment of DP-8QAM 200 G
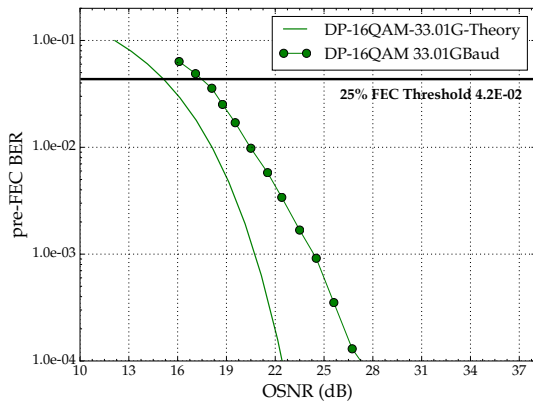
(a) BER vs OSNR
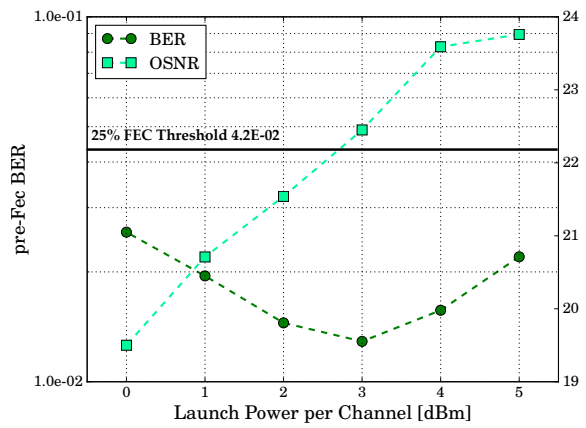
(b) Launch Power Sweep for WDM scenario

Figure 6.13: Performance assessment of DP-16QAM 200 G

tributed to the higher bandwidth of the DP-8QAM signal. An error-floor is observed at a BER of 1E-04. For the launch power sweep, the 31 DP-16QAM channels were multiplexed, with the CUT at 193.4 THz and the neighboring channels spaced at 37.5 GHz. Launch power was changed according to the method explained above. The launch power sweep results are plotted in Figure 6.13b. The complete trend of the noise and non-linearity trade-off is observable in the graph. Up-to a launch power of 3-dBm, the BER reduces, with a corresponding linear increase in the OSNR. For launch power/channel of 4 and 5 dBm, a degradation in BER is recorded. This is coupled with a non-linear saturation in the OSNR. The saturation in the OSNR is due to the increase in non-linearities originating from the optical fiber. Self-phase modulation (SPM), cross-phase modulation (XPM) and four wave mixing (FWM) interactions deteriorate the optical signal [90], inhibit the OSNR and lead to a worsening of the BER.

WDM C-Band Tranmission of DP-4QAM and DP-16QAM 200G

After the back-to-back characterization and launch power optimization, WDM transmission was carried out over selective C-band frequencies for DP-4QAM and DP-16QAM. The CUT was tuned to a specific frequency, and the neighboring channels were set accordingly. Launch power for each case of center channel frequency was adjusted according to the value found previously. For DP-4QAM, a launch power of 5 dBm/channel is set and for DP-16QAM, 3 dBm/channel is maintained. It is logical that the DP-4QAM signal has a higher launch power due to the higher bandwidth of the signal in comparison to the narrower spectrum of DP-16QAM signal.

The achieved BER results for the 31-channel transmission over 612 km over the C-band for both the modulation formats are plotted in Figure 6.14. The markers are the measured BER values and joining lines represent the interpolation between the measured values. The OSNR change over the frequencies is also plotted and a variation of 22 dB - 25 dB is seen for both the modulation formats. This trend of a different BER for lower frequencies is due to the varying noise spectrum of the EDFAs [91]. In Figure 6.14, we see that error-free transmission is obtained for all the frequencies with substantial margin to the FEC thresholds for both the cases. Error-free transmission was further confirmed by evaluating the post-FEC BER by applying an in-house SD-FEC code.

(a) BER and OSNR for DP-4QAM 200G C-Band transmission

(b) BER and OSNR for DP-16QAM 200G C-Band transmission
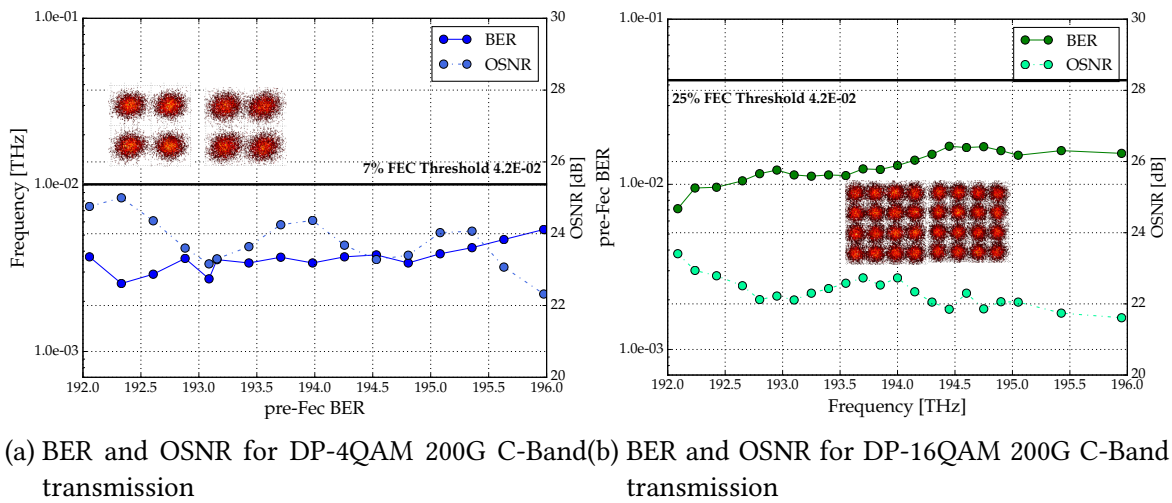
Figure 6.14: C-Band transmission for DP-4QAM and DP-16QAM over 612 km

6.3.6 Conclusion

In this section, three alternatives for single carrier 200 G systems were investigated. After the success of coherent 100 G technology in long haul, efforts were re-directed towards finding the most profitable technology for long haul 200 G. In this respect, DP-16QAM 200 G systems were already commercially available. This field trial was an effort to explore the other two alternatives : DP-4QAM and DP-8QAM for a likely addition to the 200 G technology portfolio. In terms of reach, all the three modulation formats achieved error-free transmission after 612 km of field deployed G.652 SSMF with in-line EDFAs amplification.

Table 6.3 is an extension of Table 6.2 with additional columns of spectral efficiency and residual OSNR margin. This makes it easier for a head-to-head comparison of the various technologies. DP-4QAM at 57.24 GBaud presents itself as a workable option. It has a capability of going even further on long haul links, possibly more than 1500 kms. The final spectral efficiency, however is just 2.9 bits/s/Hz. Further, the generation of such high baud rate signals with mere 32 GBaud components is a challenging task. With the availability of strong DPC and pulse shaping at the transmitter, the electronic bandwidth limitation could be overcome. Nonetheless, the option still suffers from a disadvantages w.r.t spectral efficiency.

DP-16QAM had been quite a preferred choice for the second generation of 200 G transponders. In this scenario, a second variant of DP-16QAM with 33.01 GBaud at 0.1 roll-off was tested. An underlying fundamental advantage of DP-16QAM to DP-4QAM and DP-8QAM

Modulation Format	Baud Rate (GBaud)	Roll-Off	Net Bit Rate (Gb/s)	FEC Overhead	WDM Spacing Used (GHz)	Spectral Efficiency (bits/s/Hz)	OSNR Margin (dB)
DP-4QAM	57.24	0.2	200	7%	68.75	2.9	4.1
DP-8QAM	42.0	0.2	200	15%	50.0	3.9	4.3
DP-16QAM	33.01	0.1	200	25%	37.5	5.5	2.6

Table 6.3: 200 Gbit/s single carrier configurations

is the higher spectral efficiency, owing to the higher (4) number of bits encoded in a symbol. For the undertaken link, DP-16QAM achieves error-free transmission and clearly beats both the lower-modulation formats in spectral efficiency. Hence, DP-16QAM appears as a highly feasible choice when transmission distances of < 1000 km are to be achieved. With its higher spectral efficiency and higher bandwidth compatibility to the electronics, DP-16QAM clearly appears as the best choice.

There is however a middle ground as well. Where DP-4QAM loses in spectral efficiency, DP-16QAM gains. On the other hand, when reach is an issue, DP-4QAM clearly beats DP-16QAM, due to its higher tolerance to non-linearities and the inherent capability of 4QAM symbols which require lesser energy/bit compared to DP-16QAM. It seems that DP-8QAM can fill in this gap. As seen in the results, DP-8QAM had the highest OSNR margin. Due to time limitations, a complete C-Band transmission was not possible. The DP-8QAM back-to-back results and the launch power results propel DP-8QAM towards a potential candidate for 200 G transmission for distances between 1000 km and 2000 km.

Instead of finding the most suitable candidate for 200 G transmission, all the above three technologies could be brought together in one transponder, giving the freedom to switch between each other depending on the application. The optimum choice can be made by optimizing the trade off between reach and spectral efficiency and resolving to a solution which offers the best performance for the lowest power consumption, resulting in lowest cost/bit.

6.4 Field Trial: Single carrier 400 G DP-64QAM and DP-128QAM WDM Transmission

With the advancement in optical technology, a gradual adoption of coherent transponders was first seen in long haul market, where the 100 G transponders proved to be the superior alternatives to the traditional on-off keying direct detection systems. As data rates and demands increased, coherent became the preferred option also in the metro market, due to

its easier transmission structure and higher efficiency for the same channel. Following the success in long haul and metro, the next market is the data center interconnect market. As global Internet traffic increases, a significant amount of data is being transmitted between various data centers [92].

Data center interconnects are defined as market segments which connect two or more data centers belonging to one corporation. In such cases, one data center is located quite close to the user location and the other is often situated in another location for redundancy. The typical distances between such data centers is set to be 80 km [92, 93]. Such connections need dense WDM technology and make a decent case for future coherent technology. Coherent transponders are capable of transporting terabits of data. However, since distances are small, cost/bit and power consumption become critical aspects when choosing between conventional direct detection systems or coherent systems. While direct detection systems have an advantage that they require low OSNR compared to their coherent higher order m-QAM counterparts, coherent technology has an underlying advantage of delivering higher spectral efficiency enabling a better usage of the fiber infrastructure.

Coherent single carrier solutions delivering 400 G net data rate over 80-100 km make an excellent successor to the 100 G long-haul solution in the DCI market for 50 GHz grid [94]. Higher order modulation formats, such as DP-64QAM and DP-128QAM are viable candidates for generation of single carrier 400 G signals. Due to their higher order cardinality, they relax the electrical bandwidth requirements on DACs and ADCs. Moreover, such short links are not OSNR limited, which indirectly helps the detection of higher modulation format signals. In this respect, several single carrier 400 G experiments have been carried out to establish the feasibility of 400 G signals for link distances of 80-100 km [30, 95–97]. The performance of 400 G systems employed with DP-64QAM or DP-128QAM is then hindered by the quantization noise at the DACs and ADCs. DP-64QAM and DP-128QAM are also severely affected by the non-linear effects at the transmitter side.

In this section, a field trial demonstration of single carrier 400 G signal with DP-64QAM at 45.25 GBaud and DP-128QAM at 42.0 GBaud in a WDM scenario is discussed. The 400 G signal are transmitted on Telecom Italia legacy links of length 80 km and 156 km for DP-128QAM and DP-64QAM respectively. Comparisons are drawn in terms of margin, spectral efficiency and reach.

Modulation Format	Baud Rate (GBaud)	Roll-Off	Net Bit Rate (Gb/s)	FEC Overhead	WDM Spacing Used (GHz)
DP-64QAM	45.25	0.2	400	25%	56.25
DP-128QAM	42.0	0.2	400	35%	56.25

Table 6.4: 400 Gbit/s single carrier configurations

6.4.1 Telecom Italia Link Description

The link is the same as described in Section 6.3.1, however, the link length is different. Figure 6.15 shows the combined field trial setup. The loop back from Chivasso to Turin remains unchanged from the previous 200 G field trial. The link, however, now consists of 2 spans of 76 km G.652 fiber. An extra switch was utilized to conveniently alternate between the two different link lengths. As a result, depending on the scenario a total link length of either 156 km or 80 km can be engaged. The link conditions w.r.t attenuation and CD remain the same as described previously. It is crucial to notice that the link conditions present quite a real and a challenging scenario for the transmission of DP-64QAM and DP-128QAM 400 G single wavelength signals.

6.4.2 Transmitter

The transmitter setup remains the same as already explained in Section 6.3. For the two transmission experiments, DP-64QAM at 45.25 GBaud and DP-128QAM at 42.0 GBaud were chosen. Table 6.4 summarizes the transmission configurations used in the field trial experiment. The signal baud rate and FEC are decided by considering the additional overhead of 4% from DSP and 4.7% from OTN. Both the modulation formats are extremely sensitive to various linear and non-linear impairments arising from the transponder and the link. To enable error-free transmission, higher threshold SD-FEC codes with 25% for DP-64QAM and 35% for DP-128QAM are utilized. The payload consisted of PRBS of order 32. After the suitable insertion of data-aided DSP overhead of 4%, OTN overhead of 4.7% and respective SD-FECs, bits are mapped on to DP-64QAM and DP-128QAM symbols. Nyquist RRC pulse shaping with roll 0.2 is applied. This is followed by a convolution with the DPC coefficients which were measured on-the-fly at the time of the experiment. Subsequently, the digital samples are up sampled to DAC sampling rate and uploaded on to the DACs.

The neighboring channels are generated as explained previously. For both the cases, the modulation format and baud rate of neighboring channels are the same as the CUT. Use of the same neighboring channels as WDM neighbors brings the emulation of the field trial
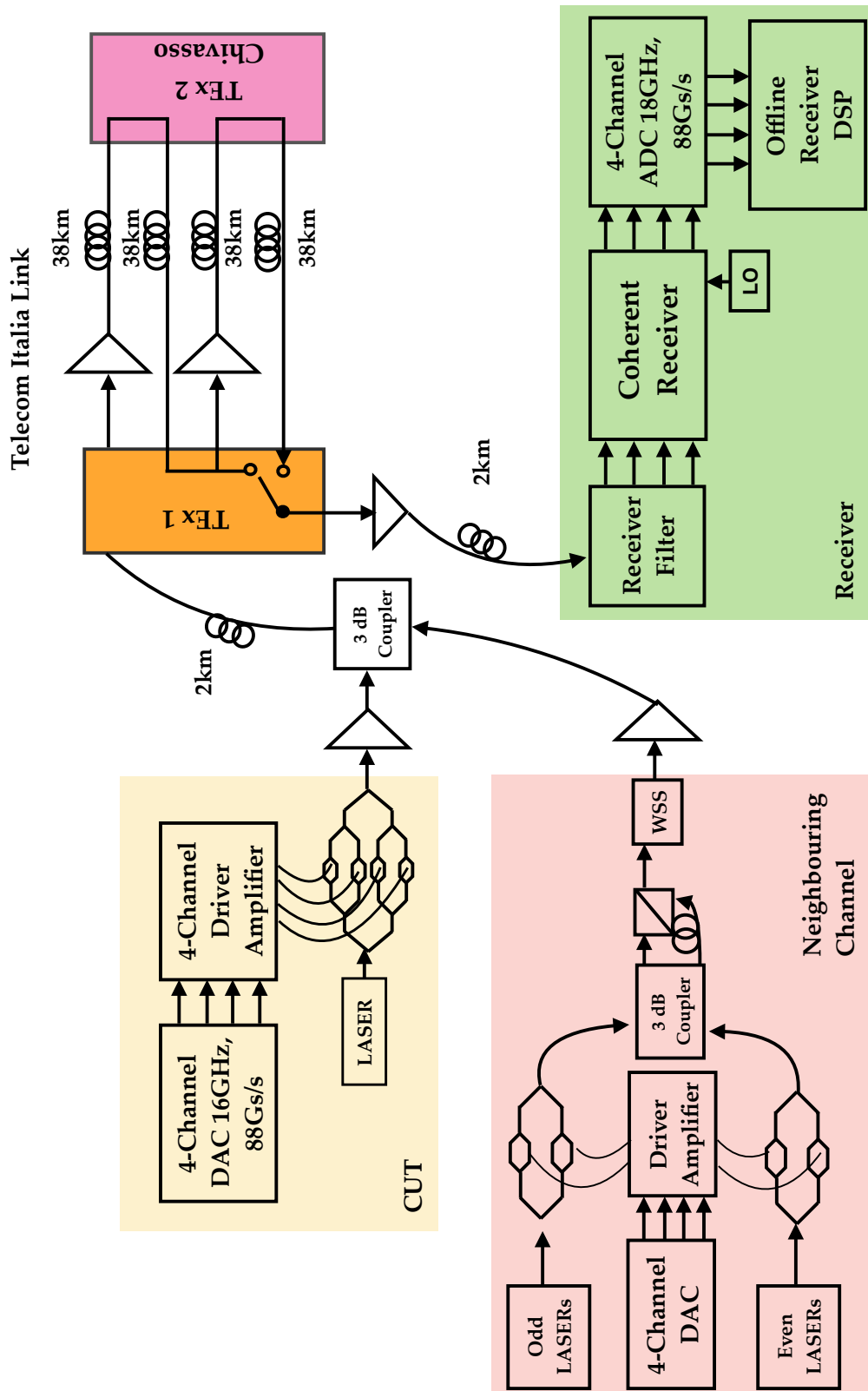
Figure 6.15: Experiment setup for Telecom Italia field trial with single carrier 400 G DP-64QAM and DP-128QAM.

setup even closer to reality, when in the future the operator decides to send WDM 400 G channels together over the link. The transmit spectrum always consists of 15 channels on the left and 14 channels on the right, resulting in 30 WDM channels.

6.4.3 Receiver Processing

The LO is tuned within 200 kHz of the transmitter LASER and signal is demodulated using intra-dyne detection. The receiver DSP remains the same as explained previously. The difference however comes in the value of CD. Approximate value of CD, considering 16.9 ps/nm/km over 80 km and 156 km is calculated and provided to the receiver DSP. The performance is assessed in terms of both pre-FEC BER and post-FEC BER.

6.4.4 Field Trial Results

We will first discuss the back-to-back BER vs OSNR characterization of both the modulation formats. The launch power optimization was done in order to find the optimal launch power to achieve best performance over the field deployed link.

400 G DP-64QAM at 45.25 GBaud

We know from Section 6.1 that DPC is an inevitable step in the process of generation of DP-64QAM 45.25 GBaud signals. The BER vs OSNR (at 0.1 nm bandwidth) result with the respective theory curve are shown in Figure 6.16. The gain obtained from DPC is evident, where it is clear that the generation of 45.25 GBaud signal with 32 GBaud components is rather challenging. An overall gain of more than 10 dB is obtained at the FEC threshold.

Following the BER vs OSNR measurements, a single DP-64QAM 45.25 GBaud channel at 193.4 THz center frequency was considered and optimal launch power was measured. The launch power results for single and WDM channel are plotted in Figure 6.17a and Figure 6.17b respectively. The transmission of single 400 G channel without any neighbors is pretty successful at a launch power of 5 dBm. Additionally, the clear trend of the curve is also seen, for lower launch powers, the BER is high due to noise and for higher launch powers, even though the OSNR increases, BER worsens due to the presence of non-linearities in the fiber. For the case with WDM, shown in Figure 6.17b, transmission over 80 km was very ambitious. It is also observed that the optimal launch power for the WDM case is 1 dB
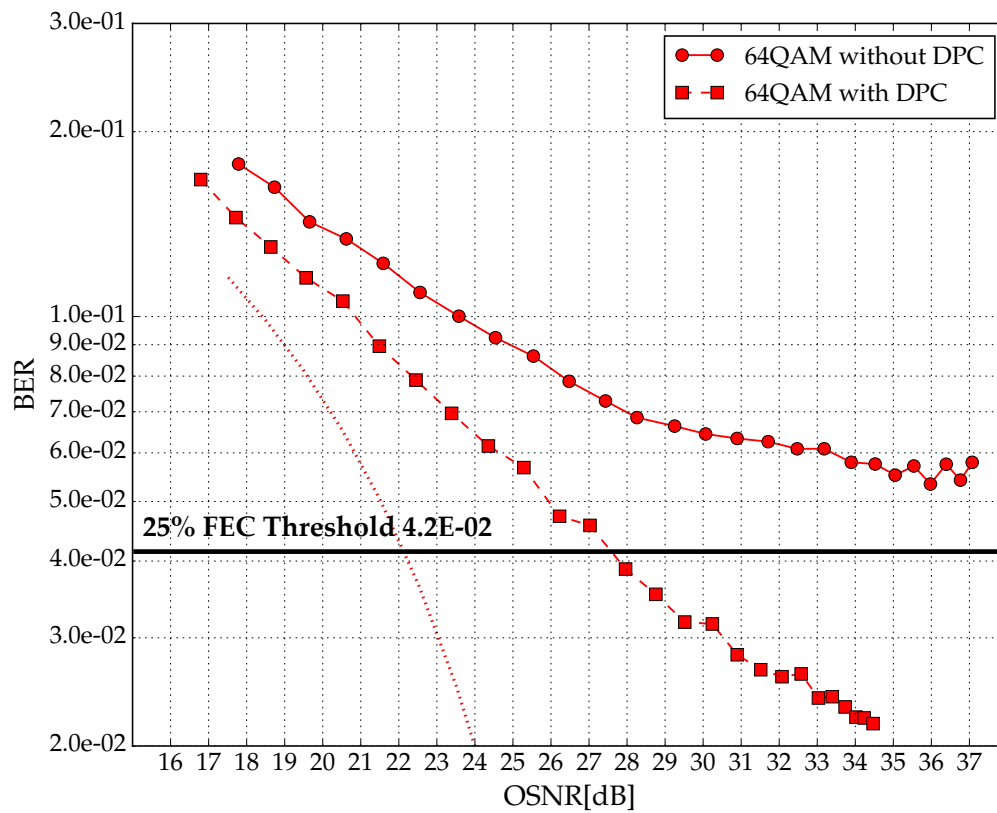
Figure 6.16: BER vs OSNR

(a) Launch power sweep for single channel   (b) Launch power sweep for WDM scenario
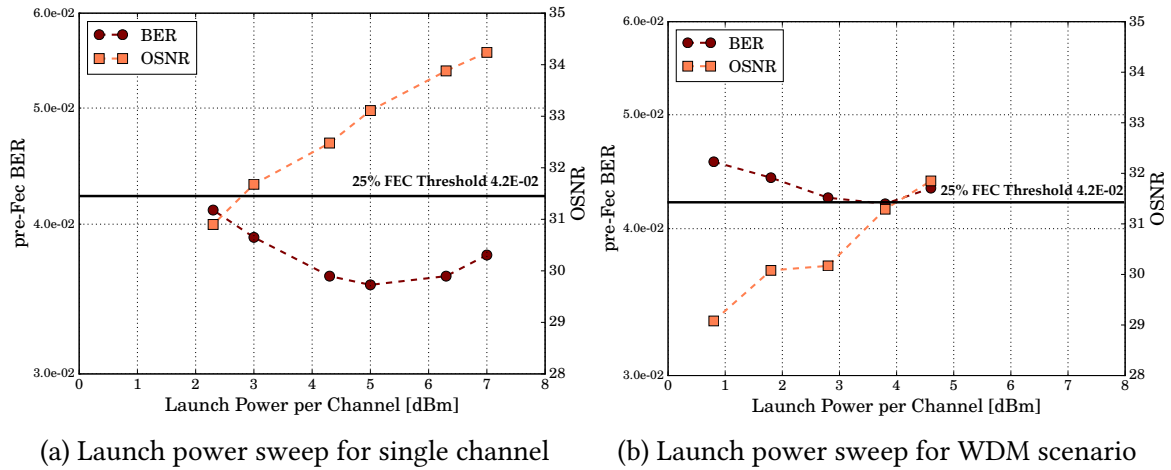
Figure 6.17: Characterization results for DP-64QAM 400 G after 80 km

less than the single channel case. A lower launch power is expected in order to alleviate the effects from non-linearities in the fiber when several WDM channels are sent together.

WDM C-Band Transmission of DP-64QAM 400 G

After the launch power sweep for the WDM scenario, the 30 channels were transmitted in to the link at a transmit power of 4 dBm/channel. The channels were spaced 56.25 GHz apart and the frequency of the CUT was always tuned at selective frequencies of the C-band. Figure 6.18b shows the spectrum of the received WDM spectrum after 80 km of transmission. Due to one defective LASER at the transmitter, one of the channels has a lower power than the rest. However, since the channel is far away from the CUT, it can be safely assumed that it has minimal impact of the overall non-linear system performance. The WDM C-band transmission results are plotted in Figure 6.18a.

Due to time limitation, only selective C-Band frequencies were chosen. It is seen from Figure 6.18a, that error-free transmission for all the frequencies was not possible. For lower frequencies, the pre-FEC BER is below the SD-FEC threshold of 4.2 E-02. For higher frequencies, due to the lower OSNR and the varying gain characteristics of the EDFAs and suboptimal launch power , successful error-free transmission could not be achieved.

The WDM results clearly indicate that WDM transmission of 400 G channels in the field trial was quite challenging. However, it is also necessary to point out that the link conditions were rather extreme with an exceptionally high net attenuation of 0.3 dB/km and several connector and splice losses. Nonetheless, certain channels were still received error-free, signifying the potential of deploying DP-64QAM with 400 G in DCI links.
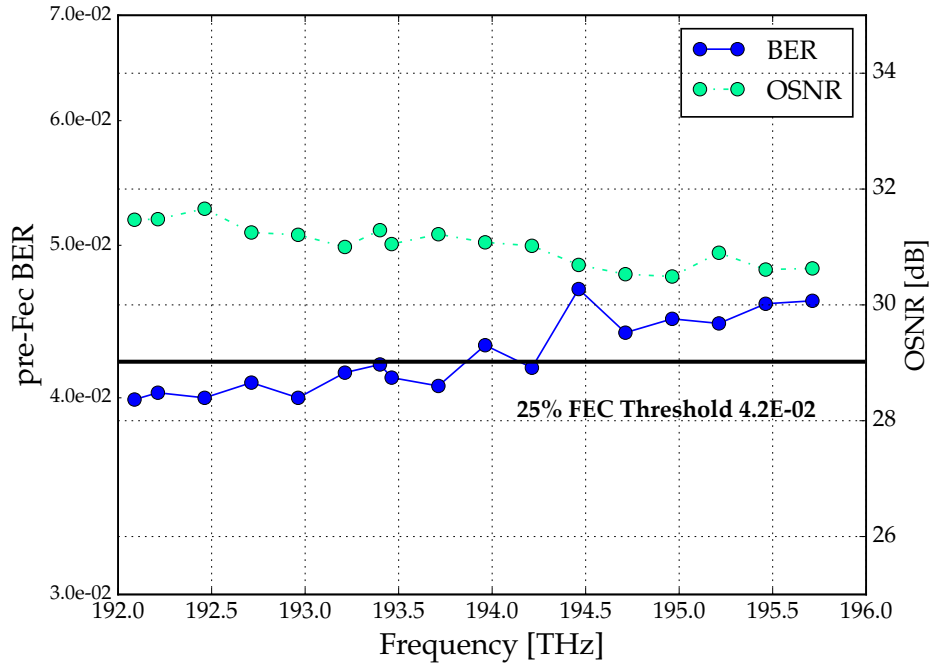
(a) C-Band transmission results for DP-64QAM
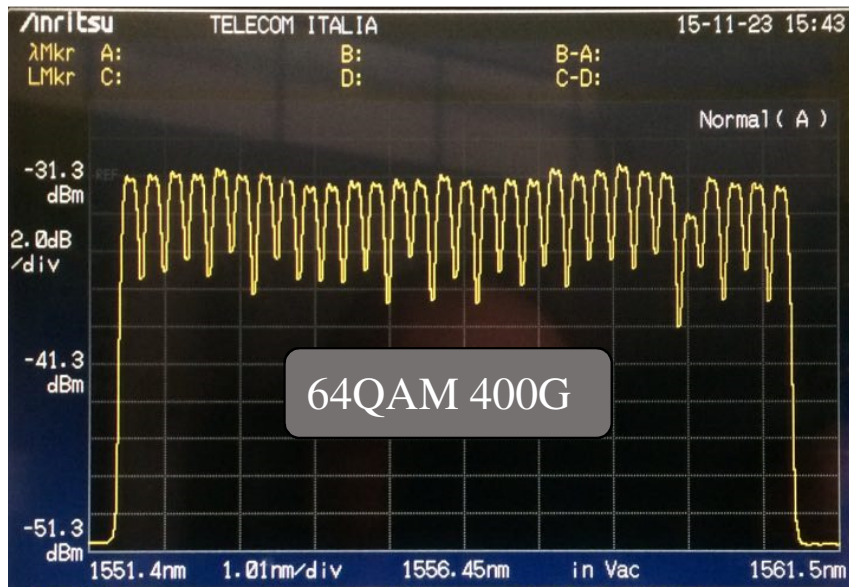
(b) WDM spectrum for 30 DP-64QAM 400 G channels
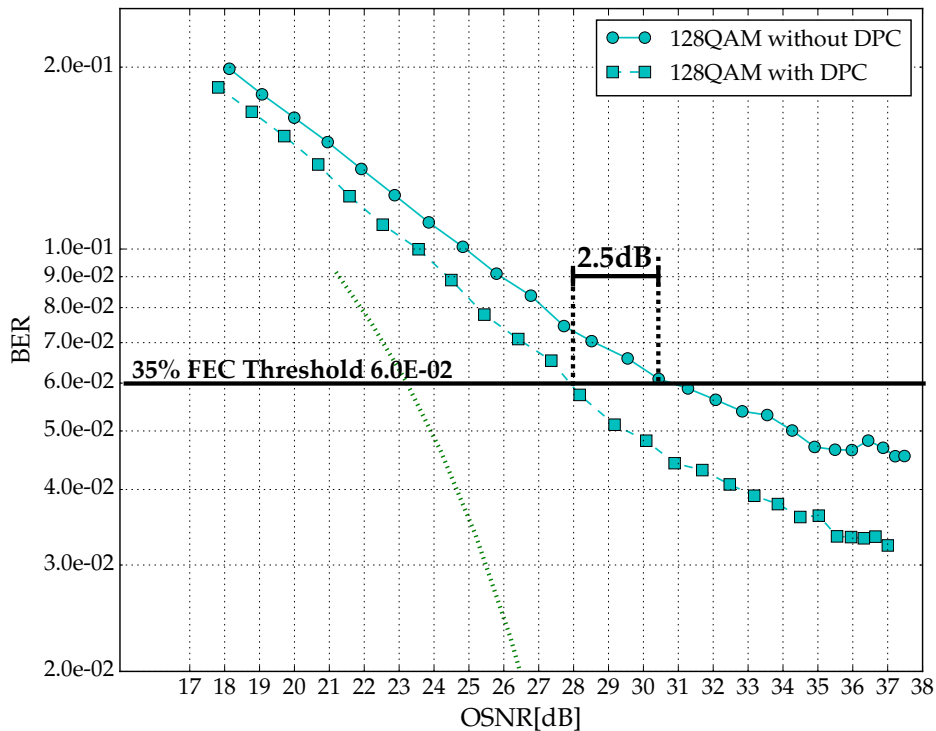
Figure 6.19: BER vs OSNR

400 G DP-128QAM at 42.0 GBaud

Another means of generating a single carrier 400 G signal is by decreasing the baud rate and thereby increasing the modulation order. The second alternative investigated in the field trial was a DP-128QAM signal with a signaling rate of 42.0 GBaud. The back-to-back BER vs OSNR results with the theory curve are presented in Figure 6.19. Given the limited ENOB of the state-of-the-art DACs, DP-128QAM modulation format is tough to produce. The generated signal from the transmitter suffers to a great extent from the bandwidth limitation, transmitter I/Q skew and non-linear effects of the driver amplifier and DP-MZM. The implementation of DPC proved to be successful. A gain of 2.5 dB at FEC threshold is obtained in comparison to the case when no DPC is employed. Nonetheless, a huge implementation penalty is also obtained.

After the BER vs OSNR characterization, launch power optimization was carried out for the case when only single channel is present and for the WDM case where 30 DP-128QAM 400 G channels are sent together in the fiber span of 80 km. The launch power results with corresponding BER and OSNR are shown in Figure 6.20. From Figure 6.20a, optimal launch

(a) Launch power sweep for single channel

(b) Launch power sweep for WDM scenario
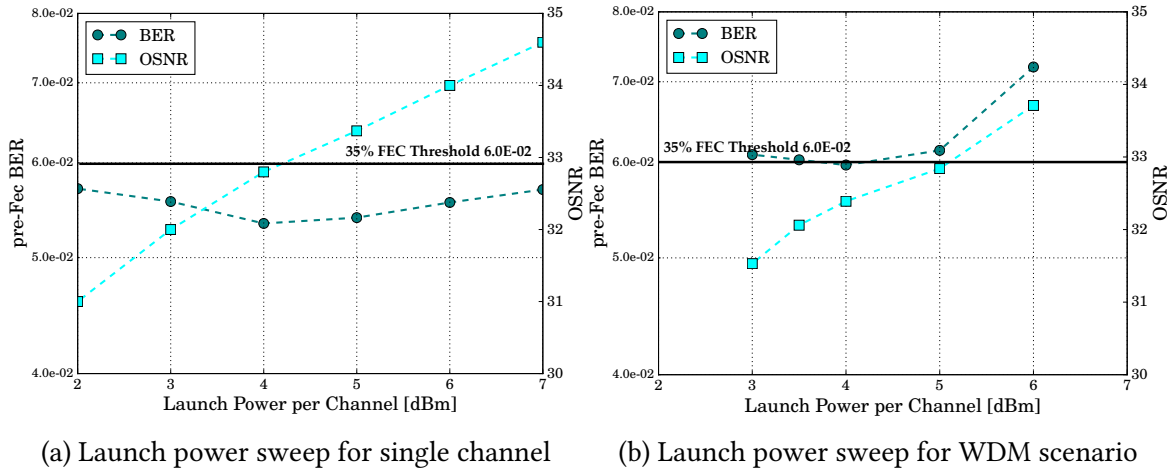
Figure 6.20: Characterization results for DP-128QAM 400 G

power is obtained at 4 dBm for CUT at 193.4 THz. This value is lower than in comparison to the DP-64QAM alternative, where the launch power for single channel was 5 dBm. This can be attributed to the lower baud rate of the DP-128QAM signal and the lower tolerance of DP-128QAM to fiber non-linearities. Moreover, error-free transmission is achieved for the single channel case, where after 80 km transmission, a BER of 5.3 E-02 is obtained.

Things look a bit different when 30 WDM channels with DP-128QAM are sent in to the 80 km fiber. An optimal launch power is obtained at 4 dBm. However, the deviation in BER for 3 dBm and 4 dBm is negligible. The BER, however, is just shy under the FEC threshold, denoting the tough link and transponder conditions to support DP-128QAM signal transmission.

6.4.5 Conclusion

In this section, field trial results of two 400 G options : DP-64QAM at 45.25 GBaud and DP-128QAM at 42.0 GBaud were discussed. Current state-of-the-art systems support 400 G systems by employing 2x200 G carriers. 400 G single carrier solutions provide an advantage by re-using the same transponder components utilized for 200 G. This enables the transport of double the capacity but with cheaper electronic and optical components, hence reducing cost, transponder footprint and power consumption. Nonetheless, the use of low bandwidth components to transport double the data-rate inhibits the signal quality. The transponder limitations could be overcome by using strong DPC at the transmitter. Coupled with strong FEC codes, transmission of single carrier DP-64QAM and DP-128QAM at

400 Gbit/s is achievable. The feasibility of the solution was tested in a field trial scenario with Telecom Italia fiber link.

30x400 G 128QAM and 30x400 G 64QAM were successfully transmitted over 80 km of field trial link between Turin and Chivasso. The link presented tough conditions with an average of 0.3 dB/km of attenuation. Amplification was carried out using legacy EDFA solutions. Efforts were made to measure the performance of DP-64QAM over the C-Band. While some channels were obtained error-free after 80 kms, the performance of other channels in the high frequency region could be further optimized with accurate amplifier and launch power configurations. With the channel spacing of 56.25 GHz, both the formats achieve a spectral efficiency of 7.11 bits/s/Hz.

The presented field trial was the first ever field trial where transmission of DP-128QAM 400 G was shown. The use of a robust DPC coupled with Nyquist pulse shaping at the transmitter enabled the generation of DP-128QAM and DP-64QAM signals at baud rates of 42.0 GBaud and 45.25 GBaud respectively. At the receiver, the strong DSP with the firm FEC threshold complemented the transmitter DSP to achieve error-free transmission after 80 km. The demonstrated results signify the potential of using DP-64QAM for future 400 G solutions, as an effective alternative to the DP-16QAM 2x200 G solution. With a further optimization in baud-rate and FEC, a spectral efficiency of 8 bit/s/Hz in 50 GHz grid is achievable. While the novelty of the field trial was in the transmission of DP-128QAM 400 G signals, it can be safely said that in the race of 400 G solutions, DP-64QAM presents itself as a better prospect, owing to the less complex FEC utilized.

6.5 Summary

As previously stated, the race is not in finding the best option for a particular technology, but to able to address the demands of 100 G, 200 G and 400 G all from the same transponder. Future transponders are being built to be able to offer flexible services, bandwidth on demand, dynamic channel provisioning. For the evolution of next generation of transponders, in order to provide further value to the operators, transponders need to be able to dynamically switch between modulation formats and baud rates depending on the link conditions.

7

Conclusions

When work was started on this thesis in February 2014 single carrier 100 G coherent optical transponders were already commercially available and first attempts were being conducted on bringing dual-carrier 200 Gbit/s systems in the market. As bandwidth demands increased, optical vendors started to find ways to transmit 400 Gbit/s, 600 Gbit/s and even 800 Gbit/s on a single wavelength. Now you might ask why the urge for single wavelength systems, when a pair of the wavelengths can also solve the problem. The incentive to push for even higher data-rates with single wavelength is the lower cost/bit of these systems. In comparison to multi-wavelength transponders, surely a single transponder transmitting the same data rate requires lesser components and hence is cheaper. To add to the lower cost/bit, these transponders demand less power. Nonetheless, the design of these transponders is not elementary.

To produce bit rates of 400 G and 600 G, signals with higher baud-rates (>32 GBaud) and higher order modulation formats (>4QAM) need to be leveraged. For the vendors which were up to now dealing with only baud rates of 32 GBaud and 4QAM modulation format, the practical implementation of these systems became challenging. We analyzed in Chapter 3 the various limitations posed by the electrical and electro-optic components for high baud rate and higher order modulation format signals. One of the biggest hurdles faced by the optical system vendors is the poor availability of high bandwidth DACs. We evaluated the effect of the 3-dB bandwidth limitation on transmission quality of various signals. The second critical aspect was the transmitter I/Q skew. With legacy systems supporing 10 Gbit/s and 40 Gbit/s the I/Q skew never materialized as a critical impairment. But, we

saw how uncompensated transmitter I/Q can affect the performance of the system by several dBs. While the 3-dB bandwidth limitation and transmitter I/Q skew were categorized as linear effects, we also looked further in to the non-linear effects which became even more apparent and crucial for transmission of higher order modulation formats (>4QAM). Since these effects start to surface already at the transmitter, the signal quality deteriorates considerably even before it reaches the optical fiber. The question comes then if something can be done to alleviate these distortions.

It turns out there are several approaches which can be used to mitigate the impairment effects of the transmitter. One of the most favored approaches is digital pre-compensation and various flavours of this were discussed in Section 2.3. Enough of the previous works approached the problem by performing lengthy time consuming individual measurements of each of the components in the transmitter namely, the digital to analog converter, electrical driver amplifier and dual polarization Mach-Zehnder Modulators. This isn't a rudimentary job, but involves sub-picosecond accurate measurement of the I/Q skew and careful probing of each of the 4 channels of a dual-polarization signal to generate the transfer functions and then repeating the process for different transmit output powers to also capture the non-linear effects from the electrical driver amplifier and DP-MZM. Now add to that the time, work and money needed to carry out these measurements for hundreds of such transponders in production. This will just lead up to several delay for the optical vendors to roll out the latest technologies.

Main contributions

A practical problem was looking for a potential solution and this was developed in the form of **Automatic Adaptive Digital Pre-Compensation** in the thesis. The DPC block is placed in the transmitter DSP chain before the transmitter. The proposed DPC block caters to the problem of 3-dB bandwidth limitation, transmitter I/Q skew and transmitter non-linear effects. The solution is based on the memory polynomial model and indirect learning architecture ILA, discussed extensively in Section 4.1 and Section 4.2. Subject to the effects to be compensated, the memory polynomial model can be adapted either in its simple linear form or the more complex non-linear form. The ILA necessitates a feedback signal to calculate the required coefficients of the DPC block. We discussed the implementation of the DPC block in the two modes : training and working. Once the DPC block is trained, normal operation of the system can then resume. The working of the DPC block was

explained for the several feedback scenarios: electrical back-to-back, optical back-to-back and optical feedback from far-end receiver. Accurate estimation of transmitter I/Q skew additionally plays a pivotal rule in the characterization of future 64 GBaud 64 QAM signals. To address this issue, further analysis was carried out on the estimation capabilities of the DPC block and a supplementary phase noise canceler block was included. This block enables a sub-picosecond estimation routine for the transmitter I/Q skew, which after all is a critical requirement for next generation 800 Gbit/s systems.

After developing the theory and design for the application of the DPC method with practical transponder systems, the theory was put into practice. The algorithm was evaluated on distinct setups and significant gains were observed across all these setups. In the optical back-to-back case considerable gain in required OSNR was obtained and it was shown that signals up to 56 GBaud can be transmitted with transmitter components which merely have a 16 GHz bandwidth, which were conventionally designed to transmit 32 GBaud signals. The same transmitter components were then shown to be employed for transmission of 400 Gbit/s signals with DP-128QAM and DP-64QAM. Had there been no DPC, transmission of such signals would not have been possible due to the penalties from the various component limitations. The algorithm was further put to test in a field trial, where in-field characterization and impairment mitigation of transmitter components was carried out. This led to the successful transmission of DP-64QAM and DP-128QAM 400 Gbit/s signals in a WDM environment. Mitigation of the non-linear effects was also made possible by testing the efficiency of the DPC algorithm in highly non-linear transmitters with DP-64QAM signals. As an effort to make the accuracy even finer the phase noise canceler in combination with the DPC block was put into practice, which led to the possibility of using cheaper LASERs for DPC estimation. In addition to the basic solution of obtaining feedback from back-to-back receiver, the DPC architecture was reconstructed to make the coefficient estimation possible when the feedback signal is obtained from a far-end receiver. In my personal opinion, this could be a more elegant solution for the next generation systems, allowing even adpative DPC to compensate for ageing and drift effects.

The DPC algorithm developed in the thesis has proven to be a robust candidate for the characterization and mitigation of transmitter components. Whether it's a 100 Gbit/s signal or 800 Gbit/s signals, the components utilized will always suffer from the aforementioned effects. For the design and development of transponders supporting flexible bits rates, the proposed DPC scheme can be a promising candidate to facilitate a faster, accurate, time and money saving automatic pre-compensation routine.

Future Work Directions

This work mainly concentrated on the characterization of transmitter impairments. This can be further developed in the following directions :

- Explore the possibility to improve the memory polynomial model to be able to compensate also the effects of the fiber channel.

- The transmitter I/Q skew estimation routine can be supplemented by a receiver I/Q skew estimation routine.

- The individual memory polynomial models for each tributary can be further adopted to enable compensation of various I/Q crosstalk and offset effects.

A

Abbreviations

Bibliography

[1] G. P. Agrawal, *Optical Communication: Its History and Recent Progress.* Springer International Publishing, 2016.

[2] G. Rademacher, R. S. Luís, B. J. Puttnam, T. A. Eriksson, E. Agrell, R. Maruyama, K. Aikawa, H. Furukawa, Y. Awaji, and N. Wada, "159 Tbit/s C+L band transmission over 1045 km 3-mode graded-index few-mode fiber," in *Optical Fiber Communication Conference Postdeadline Papers.* Optical Society of America, 2018, p. Th4C.4.

[3] N. Hanik, *Lecture Notes in Optical Communication Systems*, 2015.

[4] R. Essiambre, G. Kramer, P. J. Winzer, G. J. Foschini, and B. Goebel, "Capacity limits of optical fiber networks," *Journal of Lightwave Technology*, vol. 28, no. 4, pp. 662–701, Feb 2010.

[5] C. Laperle and M. Osullivan, "Advances in high-speed DACs, ADCs, and DSP for optical coherent transceivers," *Journal of Lightwave Technology*, vol. 32, no. 4, pp. 629–643, 2014.

[6] R. I. Killey, P. M. Watts, V. Mikhailov, M. Glick, and P. Bayvel, "Electronic dispersion compensation by signal predistortion using digital processing and a dual-drive mach-zehnder modulator," *IEEE Photonics Technology Letters*, vol. 17, no. 3, pp. 714–716, March 2005.

[7] T. Sugihara, T. Kobayashi, T. Fujimori, and T. Mizuochi, "Electronic pre-equalization technologies using high-speed dac," in *2011 37th European Conference and Exhibition on Optical Communication*, Sep. 2011, pp. 1–3.

[8] P. J. Winzer and R. Essiambre, "Advanced modulation formats for high-capacity optical transport networks," *Journal of Lightwave Technology*, vol. 24, no. 12, pp. 4711–4728, Dec 2006.

[9] D. Rafique, A. Napoli, S. Calabro, and B. Spinnler, "Digital preemphasis in optical communication systems: On the dac requirements for terabit transmission applications," *J. Lightwave Technol.*, vol. 32, no. 19, pp. 3247–3256, Oct 2014.

[10] A. Napoli, M. M. Mezghanni, D. Rafique, V. A. J. M. Sleiffer, T. Rahman, B. Spinnler, S. Calabrò, and M. Bohn, "Novel dac digital pre-emphasis algorithm for next-generation flexible optical transponders," in *2015 Optical Fiber Communications Conference and Exhibition (OFC)*, March 2015, pp. 1–3.

[11] T. Rahman, D. Rafique, A. Napoli, E. de Man, M. Kuschnerov, B. Spinnler, M. Bohn, C. M. Okonkwo, and H. de Waardt, "Long-haul terabit transmission (2272km) employing digitally pre-distorted quad-carrier pm-16qam super-channel," in *2014 The European Conference on Optical Communication (ECOC)*, Sept 2014, pp. 1–3.

[12] J. Qi, B. Mao, N. Gonzalez, L. N. Binh, and N. Stojanovic, "Generation of 28gbaud and 32gbaud pdm-nyquist-qpsk by a dac with 11.3ghz analog bandwidth," in *2013 Optical Fiber Communication Conference and Exposition and the National Fiber Optic Engineers Conference (OFC/NFOEC)*, March 2013, pp. 1–3.

[13] F. Buchali, A. Klekamp, L. Schmalen, and T. Drenski, "Implementation of 64qam at 42.66 gbaud using 1.5 samples per symbol dac and demonstration of up to 300 km fiber transmission," in *OFC 2014*, March 2014, pp. 1–3.

[14] J. Zhang, H. Chien, Y. Xia, Y. Chen, and J. Xiao, "A novel adaptive digital pre-equalization scheme for bandwidth limited optical coherent system with dac for signal generation," in *OFC 2014*, March 2014, pp. 1–3.

[15] G. Khanna, S. Calabrò, B. Spinnler, E. D. Man, and N. Hanik, "Joint adaptive pre-compensation of transmitter i/q skew and frequency response for high order modulation formats and high baud rates," in *2015 Optical Fiber Communications Conference and Exhibition (OFC)*, March 2015, pp. 1–3.

[16] C. R. S. Fludger and T. Kupfer, "Transmitter impairment mitigation and monitoring for high baud-rate, high order modulation systems," in *ECOC 2016; 42nd European Conference on Optical Communication*, Sept 2016, pp. 1–3.

[17] P. W. Berenguer, M. Nölle, L. Molle, T. Raman, A. Napoli, C. Schubert, and J. K. Fischer, "Nonlinear digital pre-distortion of transmitter components," *Journal of Lightwave Technology*, vol. 34, no. 8, pp. 1739–1745, April 2016.

[18] C. Eun and E. J. Powers, "A new volterra predistorter based on the indirect learning architecture," *IEEE Transactions on Signal Processing*, vol. 45, no. 1, pp. 223–227, Jan 1997.

[19] J. Kim and K. Konstantinou, "Digital predistortion of wideband signals based on power amplifier model with memory," *Electronics Letters*, vol. 37, no. 23, pp. 1417–1418, Nov 2001.

[20] L. Ding, G. T. Zhou, D. R. Morgan, Z. Ma, J. S. Kenney, J. Kim, and C. R. Giardina, "A robust digital baseband predistorter constructed using memory polynomials," *IEEE Transactions on Communications*, vol. 52, no. 1, pp. 159–165, Jan 2004.

[21] Y. Bao, Z. Li, J. Li, X. Feng, B. ou Guan, and G. Li, "Nonlinearity mitigation for high-speed optical ofdm transmitters using digital pre-distortion," *Opt. Express*, vol. 21, no. 6, pp. 7354–7361, Mar 2013.

[22] G. Khanna, B. Spinnler, S. Calabro, E. D. Man, U. Feiste, T. Drenski, and N. Hanik, "A memory polynomial based digital pre-distorter for high power transmitter components," in *2017 Optical Fiber Communications Conference and Exhibition (OFC)*, March 2017, pp. 1–3.

[23] G. Lazzarin, S. Pupolin, and A. Sarti, "Nonlinearity compensation in digital radio systems," *IEEE Transactions on Communications*, vol. 42, no. 234, pp. 988–999, February 1994.

[24] X. Zhou, J. Yu, M. Huang, Y. Shao, T. Wang, L. Nelson, P. Magill, M. Birk, P. I. Borel, D. W. Peckham, R. Lingle, and B. Zhu, "64-tb/s, 8 b/s/hz, pdm-36qam transmission over 320 km using both pre- and post-transmission digital signal processing," *Journal of Lightwave Technology*, vol. 29, no. 4, pp. 571–577, Feb 2011.

[25] R. Cigliutti, A. Nespola, D. Zeolla, G. Bosco, A. Carena, V. Curri, F. Forghieri, Y. Yamamoto, T. Sasaki, and P. Poggiolini, "Ultra-long-haul transmission of 16×112 gb/s spectrally-engineered dac-generated nyquist-wdm pm-16qam channels with 1.05x(symbol-rate) frequency spacing," in *OFC/NFOEC*, March 2012, pp. 1–3.

[26] Z. Dong, X. Li, J. Yu, and N. Chi, "6×144-gb/s nyquist-wdm pdm-64qam generation and transmission on a 12-ghz wdm grid equipped with nyquist-band pre-equalization," *Journal of Lightwave Technology*, vol. 30, no. 23, pp. 3687–3692, Dec 2012.

[27] T. Duthel, P. Hermann, J. Schiessl, C. R. S. Fludger, A. Bisplinghoff, and T. Kupfer, "Characterization and pre-distortion of linear and non-linear transmitter impairments for pm-64qam applications," in *ECOC 2016; 42nd European Conference on Optical Communication*, Sept 2016, pp. 1–3.

[28] C. R. S. Fludger, T. Duthel, P. Hermann, and T. Kupfer, "Low cost transmitter self-calibration of time delay and frequency response for high baud-rate qam transceivers," in *2017 Optical Fiber Communications Conference and Exhibition (OFC)*, March 2017, pp. 1–3.

[29] G. Khanna, B. Spinnler, S. Calabrò, E. D. Man, and N. Hanik, "A robust adaptive pre-distortion method for optical communication transmitters," *IEEE Photonics Technology Letters*, vol. 28, no. 7, pp. 752–755, April 2016.

[30] G. Khanna, B. Spinnler, S. Calabro, E. D. Man, U. Feiste, T. Drenski, and N. Hanik, "400g single carrier transmission in 50 ghz grid enabled by adaptive digital pre-distortion," in *2016 Optical Fiber Communications Conference and Exhibition (OFC)*, March 2016, pp. 1–3.

[31] G. Khanna, T. Rahman, E. D. Man, E. Riccardi, A. Pagano, A. C. Piat, S. Calabrò, B. Spinnler, D. Rafique, U. Feiste, H. D. Waardt, B. Sommerkorn-Krombholz, N. Hanik, T. Drenski, M. Bohn, and A. Napoli, "Single-carrier 400g 64qam and 128qam dwdm field trial transmission over metro legacy links," *IEEE Photonics Technology Letters*, vol. 29, no. 2, pp. 189–192, Jan 2017.

[32] G. Khanna, B. Spinnler, S. Calabrò, E. D. Man, U. Feiste, T. Drenski, and N. Hanik, "A memory polynomial based adaptive digital pre-distorter for optical communication transmitters," in *2017 19th International Conference on Transparent Optical Networks (ICTON)*, July 2017, pp. 1–4.

[33] G. Khanna, T. Rahman, E. d. Man, E. Riccardi, A. Pagano, A. C. Piat, B. Spinnler, S. Calabro, D. Rafique, U. Feiste, H. d. Waardt, B. Sommerkorn-Krombholz, T. Drenksi, M. Bohn, A. Napoli, and N. Hanik, "Comparison of single carrier 200g 4qam, 8qam and 16qam in a wdm field trial demonstration over 612 km ssmf," in *ECOC 2016; 42nd European Conference on Optical Communication*, Sept 2016, pp. 1–3.

[34] G. Khanna, B. Spinnler, S. Calabrò, E. de Man, Y. Chen, and N. Hanik, "Adaptive trans-

mitter pre-distortion using feedback from the far-end receiver," *IEEE Photonics Technology Letters*, vol. 30, no. 3, pp. 223–226, Feb 2018.

[35] ——, "Accurate estimation of transmitter i/q skew for high-rate spectrally efficient optical transponders," in *2018 European Conference on Optical Communication (ECOC)*, Sept 2018, pp. 1–3.

[36] G. Khanna, Y. Yoffe, E. D. Man, E. Wohlgemuth, B. Spinnler, S. Calabrò, A. Napoli, N. Hanik, and D. Sadot, "Experimental verification of 400g 64qam using 4 bits dacs enabled by digital resolution enhancer," in *2018 European Conference on Optical Communication (ECOC)*, Sept 2018, pp. 1–3.

[37] T. Rahman, D. Rafique, B. Spinnler, S. Calabrò, E. de Man, U. Feiste, A. Napoli, M. Bohn, G. Khanna, N. Hanik, E. Pincemin, C. L. Bouëtté, J. Jauffrit, S. Bordais, C. André, C. Dourthe, B. Raguénès, C. M. Okonkwo, A. M. J. Koonen, and H. de Waardt, "Long-haul transmission of pm-16qam-, pm-32qam-, and pm-64qam-based terabit super-channels over a field deployed legacy fiber," *Journal of Lightwave Technology*, vol. 34, no. 13, pp. 3071–3079, July 2016.

[38] B. Spinnler, G. Khanna, S. Calabrò, E. D. Man, U. Feiste, T. Bex, and H. von Kirchbauer, "Joint linear and non-linear adaptive pre-distortion of high baud rate transmitters for high-order modulation formats," in *2016 21st OptoElectronics and Communications Conference (OECC) held jointly with 2016 International Conference on Photonics in Switching (PS)*, July 2016, pp. 1–3.

[39] G. Colavolpe, T. Foggi, E. Forestieri, and M. Secondini, "Impact of phase noise and compensation techniques in coherent optical systems," *Journal of Lightwave Technology*, vol. 29, no. 18, pp. 2790–2800, Sept 2011.

[40] C. Shannon, "Communication in the presence of noise," *Proceedings of the IRE*, vol. 37, no. 1, pp. 10–21, jan 1949. [Online]. Available: https://doi.org/10.1109/jrproc.1949.232969

[41] Micram., "Micram dac10001 and dac10002," March 2017. [Online]. Available: http://globaltek.us.com/wp-content/uploads/2017/03/dac.pdf

[42] Fujitsu., "Dp-qpsk 100g ln modulter," November 2014. [Online]. Available: https://www.fujitsu.com/jp/group/foc/en/products/optical-devices/100gln/

[43] G. McBrien, D. Bossi, P. Hallemeier, D. Maack, D. Lafaw, D. Fritz, K. Kissa, E. Wooten, E. Murphy, A. Yi-Yan, and D. Attanasio, "A review of lithium niobate modulators for fiber-optic communications systems," *IEEE Journal of Selected Topics in Quantum Electronics*, vol. 6, no. 1, pp. 69–82, 2002. [Online]. Available: http://ieeexplore.ieee.org/document/826874/

[44] M. Seimetz, *High-Order Modulation for Optical Fiber Transmission.* Springer-Verlag Berlin Heidelberg, 2009.

[45] Hoon Kim and A. H. Gnauck, "Chirp characteristics of dual-drive. mach-zehnder modulator with a finite dc extinction ratio," *IEEE Photonics Technology Letters*, vol. 14, no. 3, pp. 298–300, March 2002.

[46] K. . Velthaus, M. Hamacher, M. Gruner, T. Brast, R. Kaiser, K. Prosyk, I. Woods, D. Hoffmann, and M. Schell, "High performance inp-based mach-zehnder modulators for 10 to 100 gb/s optical fiber transmission systems," *IPRM 2011 - 23rd International Conference on Indium Phosphide and Related Materials*, pp. 1–4, May 2011.

[47] lightwaveonline., "Optical iq modulators for coherent 100g and beyond," March 2015. [Online]. Available: https://www.lightwaveonline.com/optical-tech/electronics/article/16648483/optical-iq-modulators-for-coherent-100g-and-beyond

[48] Fujitsu., "Digital to analog converter," March 2012. [Online]. Available: http://www.fujitsu.com/downloads/MICRO/fme/documentation/c60.pdf

[49] Cheng-Po Liang, Je-Hong Jong, W. E. Stark, and J. R. East, "Nonlinear amplifier effects in communications systems," *IEEE Transactions on Microwave Theory and Techniques*, vol. 47, no. 8, pp. 1461–1466, Aug 1999.

[50] R. Raich and G. T. Zhou, "On the modeling of memory nonlinear effects of power amplifiers for communication applications," *Proceedings of 2002 IEEE 10th Digital Signal Processing Workshop, 2002 and the 2nd Signal Processing Education Workshop.*, pp. 7–10, Oct 2002.

[51] A. Napoli, M. M. Mezghanni, D. Rafique, V. A. J. M. Sleiffer, B. Spinnler, and M. Bohn, "Novel digital pre-distortion techniques for low-extinction ratio Mach-Zehnder modulators," *2015 Optical Fiber Communications Conference and Exhibition (OFC)*, no. 2, p. Th3G.1, 2015.

[52] K. Kikuchi, "Fundamentals of coherent optical fiber communications," *Journal of Lightwave Technology*, vol. 34, no. 1, pp. 157–179, 2016.

[53] L. Kazovsky, "Decision-driven phase-locked loop for optical homodyne receivers: Performance analysis and laser linewidth requirements," *Journal of Lightwave Technology*, vol. 3, no. 6, pp. 1238–1247, December 1985.

[54] M. Selmi, Y. Jaouen, and P. Ciblat, "Accurate digital frequency offset estimator for coherent polmux qam transmission systems," in *2009 35th European Conference on Optical Communication*, Sep. 2009, pp. 1–2.

[55] B. Widrow and I. Kollár, *Quantization Noise: Roundoff Error in Digital Computation, Signal Processing, Control, and Communications.* Cambridge University Press, 2008.

[56] B. Widrow, I. Kollar, and Ming-Chang Liu, "Statistical theory of quantization," *IEEE Transactions on Instrumentation and Measurement*, vol. 45, no. 2, pp. 353–361, April 1996.

[57] R. H. Walden, "Performance trends for analog to digital converters," *IEEE Communications Magazine*, vol. 37, no. 2, pp. 96–101, Feb 1999.

[58] Y. Yoffe and D. Sadot, "Novel low resolution adc-dsp optimization based on non-uniform quantization and mlse for data centers interconnects," *Opt. Express*, vol. 24, no. 5, pp. 5346–5354, Mar 2016. [Online]. Available: http://www.opticsexpress.org/abstract.cfm?URI=oe-24-5-5346

[59] M. Kuschnerov, F. N. Hauske, K. Piyawanno, B. Spinnler, M. S. Alfiad, A. Napoli, and B. Lankl, "Dsp for coherent single-carrier receivers," *Journal of Lightwave Technology*, vol. 27, no. 16, pp. 3614–3622, Aug 2009.

[60] S. J. Savory, "Digital coherent optical receivers: Algorithms and subsystems," *IEEE Journal of Selected Topics in Quantum Electronics*, vol. 16, no. 5, pp. 1164–1179, Sep. 2010.

[61] B. Spinnler, "Equalizer design and complexity for digital coherent receivers," *IEEE Journal of Selected Topics in Quantum Electronics*, vol. 16, no. 5, pp. 1180–1192, Sep. 2010.

[62] R. Schmogrow, S. Ben-Ezra, P. C. Schindler, B. Nebendahl, C. Koos, W. Freude, and J. Leuthold, "Pulse-shaping with digital, electrical, and optical filters - A comparison," *Journal of Lightwave Technology*, vol. 31, no. 15, pp. 2570–2577, 2013.

[63] G. Bosco, "Advanced Modulation Techniques for Flexible Optical Transceivers: The Rate/Reach Tradeoff," *Journal of Lightwave Technology*, vol. 37, no. 1, pp. 36–49, 2019.

[64] M. Mazurczyk, "Spectral shaping in long haul optical coherent systems with high spectral efficiency," *Journal of Lightwave Technology*, vol. 32, no. 16, pp. 2915–2924, 2014.

[65] X. Zhou, "Efficient clock and carrier recovery algorithms for single-carrier coherent optical systems: A systematic review on challenges and recent progress," *IEEE Signal Processing Magazine*, vol. 31, no. 2, pp. 35–45, March 2014.

[66] F. Gardner, "A bpsk/qpsk timing-error detector for sampled receivers," *IEEE Transactions on Communications*, vol. 34, no. 5, pp. 423–429, May 1986.

[67] M. Oerder and H. Meyr, "Digital filter and square timing recovery," *IEEE Transactions on Communications*, vol. 36, no. 5, pp. 605–612, May 1988.

[68] K. Mueller and M. Muller, "Timing recovery in digital synchronous data receivers," *IEEE Transactions on Communications*, vol. 24, no. 5, pp. 516–531, May 1976.

[69] A. M. Viterbi, "Nonlinear Estimation of PSK-Modulated Carrier Phase with Application to Burst Digital Transmission," *IEEE Transactions on Information Theory*, vol. 29, no. 4, pp. 543–551, 1983.

[70] M. Schetzen, *The Volterra and Wiener Theories of Nonlinear Systems.* reprint ed. R. E. Krieger Publishing, 1989.

[71] G. Strang, *Introduction to Linear Algebra.* Wellesley-Cambridge Press, 2016. [Online]. Available: https://books.google.de/books?id=efbxjwEACAAJ

[72] L. Kazovsky, "Decision-driven phase-locked loop for optical homodyne receivers: Performance analysis and laser linewidth requirements," *Journal of Lightwave Technology*, vol. 3, no. 6, pp. 1238–1247, December 1985.

[73] M. Gardner, *Phaselock Techniques, Third Edition.* John Wiley and Sons Inc, 1980.

[74] ADVA., "Adva optical networking unveils industry first with 600gbit/s per wavelength dci technology," March 2017. [Online]. Available: https://www.advaoptical.com/en/newsroom/press-releases/20170320-adva-optical-networking-unveils-industry-first-with-600gbit-s-per-wavelength-dci-technology

[75] NTT., "World's fastest 600-gbit/s per lambda optical transmission with 587-gbit/s data transfer—prospect for realizing 600-gbit/s optical network and data transfer protocol," Dec 2018. [Online]. Available: https://www.ntt-review.jp/archive/ntttechnical.php?contents=ntr201906sr1.html

[76] H. Journalist., "Tencent transmits single-wavelength 600gbit/s signals over its opc-4 open line system," Nov 2018. [Online]. Available: https://hostingjournalist.com/data-center/tencent-transmits-single-wavelength-600gbit-s-signals-over-its-opc-4-open-line-system/

[77] H. Chaouch, M. Filer, and A. Bechtolsheim, "Lessons learned from cfp2-aco system integrations, interoperability testing and deployments," in *2017 Optical Fiber Communications Conference and Exhibition (OFC)*, March 2017, pp. 1–3.

[78] R. Rios-Müller, J. Renaudier, P. Brindel, C. Simonneau, P. Tran, A. Ghazisaeidi, I. Fernandez, L. Schmalen, and G. Charlet, "Optimized spectrally efficient transceiver for 400-gb/s single carrier transport," in *2014 The European Conference on Optical Communication (ECOC)*, Sep. 2014, pp. 1–3.

[79] W. Idler, F. Buchali, and K. Schuh, "Experimental study of symbol-rates and mqam formats for single carrier 400 gb/s and few carrier 1 tb/s options," in *2016 Optical Fiber Communications Conference and Exhibition (OFC)*, March 2016, pp. 1–3.

[80] D. Qian, M.-F. Huang, E. Ip, Y.-K. Huang, Y. Shao, J. Hu, and T. Wang, "101.7-tb/s (370×294-gb/s) pdm-128qam-ofdm transmission over 3×55-km ssmf using pilot-based phase noise mitigation," in *Optical Fiber Communication Conference/National Fiber Optic Engineers Conference 2011*, 2011, p. PDPB5.

[81] D. Wang, X. Lv, R. Wang, F. Zhang, and Z. Chen, "515 gb/s, 10.31 b/s/hz, optical pdm-128-qam nyquist signal transmission over 155-km ssmf," in *2014 OptoElectronics and Communication Conference and Australian Conference on Optical Fibre Technology*, July 2014, pp. 784–785.

[82] S. Okamoto, T. Omiya, K. Kasai, M. Yoshida, and M. Nakazawa, "140 gbit/s coherent optical transmission over 150 km with a 10 gsymbol/s polarization-multiplexed 128 qam signal," in *2010 Conference on Optical Fiber Communication (OFC/NFOEC), collocated National Fiber Optic Engineers Conference*, March 2010, pp. 1–3.

[83] M. Hirano, Y. Yamamoto, Y. Tamura, T. Haruna, and T. Sasaki, "Aeff-enlarged pure-silica-core fiber having ring-core profile," in *OFC/NFOEC*, March 2012, pp. 1–3.

[84] Y. R. Zhou, K. Smith, M. Wilkinson, R. Payne, A. Lord, T. Bennett, and M. Frankel, "Coherent 100G Field Trial Over Installed Fiber Links: Investigating Key Network Scenarios and Applications [Invited]," *Journal of Optical Communications and Networking*, vol. 4, no. 11, p. B35, 2012.

[85] S. Perrin, "Deployment & Service Activation at 100G & Beyond Prepared by 100G Market Overview," March 2015.

[86] D. Rafique, T. Rahman, B. Spinnler, E. Pincemin, S. Calabro, E. de Man, U. Feiste, J. Slovak, A. Napoli, C. Le Bouette, J. Jauffrit, S. Bordais, G. Khanna, N. Hanik, C. Okonkwo, M. Kuschnerov, A. M. J. Koonen, C. Dourthe, B. Raguenes, T. Drenski, B. Sommerkorn-Krombholz, H. de Waardt, and M. Bohn, "Multi-flex field trial over 762km of g.652 ssmf using programmable modulation formats up to 64qam," *2016 Optical Fiber Communications Conference and Exhibition (OFC)*, pp. 1–3, March 2016.

[87] A. Pagano, E. Riccardi, M. Bertolini, V. Farelli, and T. V. D. Velde, "400 Gb / s Real-Time Trial Using Rate-Adaptive Transponders for Networks [Invited]," *J. Optic. Comm. Netw.*, vol. 7, no. 1, pp. 52–58, 2015.

[88] Y. R. Zhou, K. Smith, R. Payne, A. Lord, J. Hopewell, J. Weatherhead, J. Chen, J. Yao, W. Liu, C. Zhao, Y. Xiong, Z. Xiao, and P. Du, "Field Demonstration of up to 3 Tb/s Real-Time Superchannel Transport over 359 km Using a Fully Managed Flexible Grid Infrastructure with Net Spectral Efficiency of 5.97 b/s/Hz," *Journal of Lightwave Technology*, vol. 34, no. 2, pp. 805–811, 2016.

[89] Y. R. Zhou, K. Smith, S. West, M. Johnston, J. Weatherhead, P. Weir, J. Hammond, A. Lord, J. Chen, W. Pan, C. Cao, R. Yang, N. Zhou, and S. Wu, "Field trial demonstration of real-time optical superchannel transport up to 5.6 Tb/s over 359 km and 2 Tb/s over a live 727 km flexible grid optical link using 64 GBaud software configurable transponders," *Journal of Lightwave Technology*, vol. 35, no. 3, pp. 499–505, 2017.

[90] G. P. Agrawal, "Nonlinear fiber optics," in *Nonlinear Science at the Dawn of the 21st Century*, P. L. Christiansen, M. P. Sørensen, and A. C. Scott, Eds. Berlin, Heidelberg: Springer Berlin Heidelberg, 2000, pp. 195–211.

[91] H. Bissessur, C. Bastide, S. Etienne, and S. Dupont, "24 tb/s unrepeatered c-band transmission of real-time processed 200 gb/s pdm-16-qam over 349 km," in *2017 Optical Fiber Communications Conference and Exhibition (OFC)*, March 2017, pp. 1–3.

[92] "Understanding data center interconnect: Inter-data center," https://www.neophotonics.com/what-is-inter-data-center-interconnect-dci/, accessed: 2018-01-05.

[93] A. Dochhan, H. Griesser, N. Eiselt, M. H. Eiselt, and J. P. Elbers, "Solutions for 80 km DWDM Systems," *Journal of Lightwave Technology*, vol. 34, no. 2, pp. 491–499, 2016.

[94] X. Zhou and L. E. Nelson, "400G WDM transmission on the 50 GHz grid for future optical networks," *Journal of Lightwave Technology*, vol. 30, no. 24, pp. 3779–3792, 2012.

[95] K. Kasai, Y. Wang, D. Otuya, M. Yoshida, and N. M., "448 Gbit/s, 32 Gbaud 128 QAM coherent transmission over 150 km with a potential spectral efficiency of 10.7 bit/s/Hz." *Optics Express*, vol. 23, no. 22, pp. 28 423—-28 429, 2015.

[96] O. Bertran-Pardo, J. Renaudier, H. Mardoyan, P. Tran, R. Rios-Muller, A. Konczykowska, J.-Y. Dupuy, F. Jorge, M. Riet, B. Duval, J. Godin, S. Randel, G. Charlet, and S. Bigo, "Transmission of 50-GHz-Spaced Single-Carrier Channels at 516Gb/s over 600km," *2013 Optical Fiber Communication Conference and Exposition and the National Fiber Optic Engineers Conference (OFC/NFOEC)*, no. 1, p. OTh4E.2, 2013.

[97] D. Wang, X. Lv, R. Wang, F. Zhang, and Z. Chen, "515 Gb/s , 10.31 b/s/Hz , optical PDM-128-QAM Nyquist signal transmission over 155-km SSMF," *Optoelectronics and Communications Conference (OECC)*, pp. 784–785, July 2014.